Federal University of Minas Gerais

Graduate Program in Mechanical Engineering, UFMG, Belo Horizonte, Brazil

Ph.D. Thesis

Thesis Title

Prediction of Solar/Wind Energy in a Hybrid Renewable Energy System Using Artificial Intelligence

Ph.D. Candidate

Ali Khosravi

Advisor

Prof. Luiz Machado

June 2018

FEDERAL UNIVERSITY OF MINAS GERAIS (UFMG)

SCHOOL OF ENGINEERING

GRADUATE PROGRAM IN MECHANICAL ENGINEERING

"Prediction of Solar/Wind Energy in a Hybrid Renewable Energy System Using Artificial Intelligence"

Ali Khosravi

Thesis submitted to the Graduate Program in Mechanical Engineering of Federal University of Minas Gerais (UFMG), as a requirement for obtaining the title "Doctor of Philosophy in Mechanical Engineering".

PhD committee:

Prof. Dr. Luiz Machado
Department of Mechanical Engineering-UFMG (Advisor)

Prof. Dr. Raphael Nunes De Oliveira
Department of Mechanical Engineering-UFMG (Internal Examiner)

Prof. Dr. Tatiana Paula Alves
Centro Universitário UNA (External Examiner)

Prof. Dr. Ralney Nogueira De Faria
Centro Federal de Educação Tecnológica de Minas Gerais (External Examiner)

Prof. Dr. Rudolf Huebner
Department of Mechanical Engineering-UFMG (Internal Examiner)

Prof. Dr. Antonio Maia
Department of Mechanical Engineering-UFMG (Alternate Member)

Belo Horizonte, June 21st, 2018

Contents

List of Figures

List of Tables

Nomenclature

A: area (m^2)
AR: area ratio
BRS: basic refrigeration system
BD: book depreciation
BL: book life
B: baffle spacing (m)
CI: The cost of expenses or cost of investment
COP: coefficient performance
CRS: cascade refrigeration system
cp: specific thermal capacity (kJ/kg °C)
C_t: tube clearance
CC: Capital cost
Cp: power efficiency
cp_a: air specific heat (kJ/kg K)
cp_v: vapor specific heat (kJ/kg K)
d_o: outer diameter (m)
D_s: shell diameter (m)
$\dot{E}x$: exergy flow rate (kW)
FF: fill factor
G_T: incident solar radiation (kWh/m²)
$\overline{H}$: monthly average solar radiation (MJ/m²)
$\overline{H}_o$: monthly average daily extraterrestrial radiation (MJ/m²)
$\overline{H}_d$: monthly average daily defuse radiation (MJ/m²)
h: specific enthalpy (kJ/kg)
h_{cp}: heat transfer coefficient of convection boiling (W/m^2K)
h_{np}: heat transfer coefficient of nuclear boiling (W/m^2K)
$\dot{I}$: rate of exergy destruction (kW)
i_r: interest rate
I_{sc}: short-circuit current (A)
I_{mp}: current at maximum power point (A)
K: conduction coefficient (W/mK)
ke: kinetic energy
$\overline{K}_T$: monthly average clearness index
L_t: tube length (m)
LCC: life cycle cost
m: mass
$\dot{m}$: mass flow rate (kg/s)
n_p: life span
NOCT: normal operating cell temperature
N_p: number of passes
N_t: number of tube
N_b: number of baffles
Nu: Nusselt number
P: pressure (kPa)
P: power (kW)
P_r: tube pitch ratio
Pr: Prandtl number
PV: photovoltaic
$\dot{Q}$: heat transfer rate (kW)
s: specific entropy (kJ/kg K)
STC: standard test condition
T: temperature (°C)
T_0: surrounding temperature (°C)

Subscripts/Superscripts
1, 2,..., 10: thermodynamic states of fluid in the refrigeration
comp: compressor
cond: condenser
c.v: control volume
d: diffuser
eje: ejector
eva: evaporator
ex.v: expansion valve
f: working fluid (refrigerant)
v: vapor
HX: heat exchanger
i: inlet
is: isentropic process
l: liquid
mn: motive nozzle
ms: mixing suction
o: outlet
OM: the operating and maintenance costs
PEC: purchased equipment cost
sn: suction nozzle
st: standard refrigeration cycle

w: water
z= height (m)
T: total
b: beam radiation
d: diffuse radiation
c: array
dest: destruction
p: potential
ch: chemical
chi: chill
a: air

Greek Symbols
ω: ejector suction mass flow rate to motive mass flow
ρ: density (kg/m^3)
η: energy efficiency
τ: time of cycle working per year
ΔT: temperature difference (°C)
ΔP: pressure drop in suction nozzle (kPa)
χ: Martinelli factor
σ: surface tension (N/m)
μ: dynamic viscosity
η_m: transmission efficiency
ω: humidity ratio
η_g: generator efficiency
α: constant coefficient
Ψ: exergy efficiency
β: slope angle (deg)
η_{mp}: maximum power point efficiency
η_e: efficiency of any power-conditioning equipment
δ: declination angle
γ: azimuth angle (deg)

TRR: total revenue requirement
TNI: total net investment
TCR: total capital recovery
T_m: module temperature (K)
T_s: surface temperature of the sun (K)
T_{sky}: sky temperature (K)
U_L: loss coefficient
v: velocity (m/s)
VCC: volumetric cooling capacity (kJ/m^3)
v_m: wind speed (m/s)
V_{oc}: open-circuit voltage (V)
V_{mp}: voltage at maximum power point (V)
$\dot{w}$: work rate (kW)
x: quality

μ_{mp}: maximum power point temperature coefficient
ϕ: latitude (deg)
$\tau\alpha$: effective transmittance-absorptance product
τ: time of cycle working per year
χ: Martinelli factor

Preface

This dissertation is submitted for the degree of Doctor of Philosophy at the Federal University of Minas Gerais (UFMG). The research described herein was conducted under the supervision of Professor Luiz Machado in Department of Mechanical Engineering, Federal University of Minas Gerais, Between March 2016 and June 2018.

This Work is to the best of my knowledge original, except where acknowledgments and references are made to previous work. Neither this nor any substantially similar dissertation has been or is being submitted for any other degree, diploma or other qualification at any other university. This dissertation contains less than 40,000 words.

The following publications were presented based on the knowledge of this dissertation:

1. **A. Khosravi***, R. N. N. Koury, and L. Machado, "Thermo-Economic Analysis and Sizing of the Components of an Ejector Expansion Refrigeration System," *International Journal of Refrigeration*, vol. 86, pp. 463–479, Feb. 2018.

2. **A. Khosravi***, R. N. N. Koury, L. Machado, and J. J. G. Pabon, "Prediction of Hourly Solar Radiation in Abu Musa Island Using Machine Learning Algorithms," *Journal of Cleaner Production*, vol. 176, no. C, pp. 63–75, 2018.

3. **A. Khosravi***, R. N. N. Koury, L. Machado, and J. J. G. Pabon, "Energy, Exergy and Economic analysis of a Hybrid Renewable Energy with Hydrogen Storage System," *Energy*, vol. 148, no. C, pp. 1087-1102, 2018.

4. **A. Khosravi***, J. J. G. Pabon, R. N. N. Koury, and L. Machado, "Using Machine Learning Algorithms to Predict the Pressure Drop During Evaporation of R407C," *Applied Thermal Engineering*, vol. 133, no. C, pp. 361–370, 2018.

5. **A. Khosravi***, R. N. N. Koury, L. Machado, and J. J. G. Pabon, "Prediction of Wind Speed and Wind Direction Using Artificial Neural Network, Support Vector Regression and Adaptive Neuro-Fuzzy Inference System," *Sustainable Energy Technologies and Assessments*, vol. 25, pp. 146–160, Feb. 2018.

6. J.J. Garcia, T. Ali, W.M. Duarte, **A. Khosravi**, and L.Machado, "Comparison of Transient Response of an Evaporator Model Working with R1234yf as a Drop-in Replacement for R134a," *International Journal of Refrigeration*, 2018.

7. **A. Khosravi***, R. N. N. Koury, and L. Machado, "Time-Series Prediction of Wind Speed Using Machine Learning Algorithms: A Case Study Osorio Wind Farm, Brazil," *Applied Energy*, "In Revision".

8. **A. Khosravi*** and L. Machado, "Estimation of Density and Compressibility Factor of Natural Gas Using Adaptive Neuro-Fuzzy Inference System Optimized with Genetic Algorithm," *Journal of Petroleum Science and Engineering*, "In Revision".

9. **A. Khosravi*** and L. Machado, "Comparison of Artificial Intelligence Methods in Estimation of Daily Global Solar Radiation," *Journal of Cleaner Production*, "In Revision".

Under Review:

10. **A. Khosravi*** and L. Machado, "Energy, Exergy and Economic Analyses of Hybrid Ocean Thermal Energy Conversion/Photovoltaic System with Hydrogen Storage System," *Applied Energy*, "In Revision".

11. J. J. G. Pabon, **A. Khosravi***, Ricardo Poley, and L. Machado, "Multi-Objective Optimization of Air Conditioning System with The Low GWP Refrigerant R1234yf Using Genetic Algorithm," *Energy*, "Submitted".

12. **A. Khosravi***, L. Machado, "Energy and Exergy Analyses of an Ejector Expansion Refrigeration System with The Low GWP Refrigerants," Applied Thermal Engineering, "Submitted".

Ali Khosravi

June 2018

b

Acknowledgement

Thanks to the never-ending support of my supervisor Professor Luiz Machado for his hospitality, provision of facilities and assistance in this dissertation. Undoubtedly, Boiling and Condensation was the best course that I have taken, which was taught by Prof. L. Machado.

Furthermore, I would like to express thanks to Professor R.N.N. Koury (was my supervisor in this Ph.D. thesis and unfortunately we missed him), who provided insight and expertise that greatly assisted this dissertation.

Special thanks go to my wife to endure the problems in a new life. She also has been like a consultant for me in these years.

I would like to thank my colleagues at Federal University of Minas Gerais (UFMG), Prof. R.O. Nunes and Dr. J.J. Garcia, for their useful insight and assistance.

Ali Khosravi

June 2018

c

Abstract

The case study is Unit 132 of the second refinery of the South Pars, Bushehr in the south of Iran. This unit has a refrigeration system that is responsible to deliver 39 kg/s cold water for cooling the equipment of the refinery. In the first part, two refrigeration systems are designed for this target, which are heat exchanger refrigeration system (HXRS) and ejector expansion refrigeration system (EERS). R134a, R407C and R410A refrigerants are evaluated to identify the most suitable one for the proposed systems. Energy, exergy, economic and environmental analyses are investigated for each system. Sizing of the evaporator, condenser and ejector device are determined. In the second part, artificial intelligence methods are developed to predict solar and wind energy. These predicted data are employed to calculate the produced power by wind turbines and photovoltaic panels. In the third part, a hybrid renewable energy with hydrogen energy storage system is designed to provide the electrical energy for this refrigeration unit. The target of this part is to define and assess an off-grid hybrid renewable energy with hydrogen storage system. The system combines solar energy, wind energy, hydrogen production unit and fuel cell. Energy, exergy, and economic analyses are carried out for the proposed system. The results demonstrated that from energy, exergy, environmental and economic point of views R134a EERS is more efficient than HXRS with different working fluids. For prediction of solar radiation data, multilayer feed-forward neural network (MLFFNN) and support vector regression (SVR) performed better than the other developed models. For wind speed prediction, SVR outperformed the other developed models for all time intervals. Also, for hybrid renewable energy system, the amount of energy and exergy efficiencies for photovoltaic system (in the case study region) were obtained as 12% and 16%, respectively. In addition, for wind turbine system, the values of energy and exergy efficiencies were achieved 32% and 26%, respectively. The payback period of the proposed renewable energy system was obtained around 11 years.

Keywords: Refrigeration system; Photovoltaic system; Wind energy; Hydrogen storage system; Artificial intelligence

1

Chapter 1
Introduction

Most of sun's ultraviolet (UV) radiation is absorbed by ozone layer of the earth. This layer contains a high concentration of ozone. The ozone layer is vitally important to life because it absorbs biologically harmful ultraviolet (UV) radiation coming from the sun [1]. Today most of the industrial units use the electrical energy that it is produced by power stations which are fueled by fossil fuels. A lot of pollution is released by these power stations and it causes the destruction of the ozone layer [2]. The increase in energy demand, depletion of fossil resources and environmental pollution problem have led to growth of interest in more efficient systems [3]. Therefore, efforts to reduce high-grade energy consumption are necessary and it is useful to develop innovative alternatives in technologies that involve large amounts of power consumption, such as vapor compression refrigeration. As an example, one can consider alternative ejector refrigeration system (ERS).

There is a growing global demand for energy, but also for reducing strain on the environment. Considerable investments were made in alternative energy research worldwide recently. Growing demand for environment-friendly energy makes renewable energy development and production a sound investment for the future. Solar energy can be defined as the energy produced by the Sun's radiation. This energy comes in two forms, heat and light. Since solar energy comes from the sun it is considered a renewable source of energy because nothing is consumed to use this energy. Solar energy is also a clean source of energy that does not damage the environment with harmful emissions or waste like other source such as nuclear and conventional energy. Solar energy sources can be located anywhere that there is sunlight, thus solar energy sites can be constructed close to where consumers are located; this could potentially reduce transmission and distribution costs [4]. An important feature to design required photovoltaic systems is prediction of solar energy, that machine learning algorithms are currently, the most popular for this target [5]. Several studies were proposed machine learning algorithms to predict solar irradiance in different worldwide regions [6]–[9].

Between the renewable energies, the wind energy is more accessible and fairly cheaper [10]. Wind energy is a clean resource and does not pollute the air like fossil fuel power stations. In addition, it does not produce atmospheric emissions which increase health problems. Power produced by WTs depends on wind speed. Due to the importance of short-term prediction of the wind speed for connecting and disconnecting the power to the grid and management of the power, many investigations have implemented artificial intelligence methods in order to predict wind speed data [11]–[13]. Artificial neural network (ANN) is a kind of the artificial intelligence that is proposed to predict wind speed data [13]–[20]. Meteorological data, e.g., pressure, temperature, relative humidity, etc., of the region are proposed to construct the intelligent models [21], [22].

The aims of this thesis are to design and asses a refrigeration system for supplying the cold water for Unit 132 of the second refinery of the South Pars, Bushehr in the south of Iran. Also, designing and evaluating a hybrid photovoltaic/wind energy system with hydrogen energy storage system to provide the electrical energy for the refrigeration system and to discuss the feasibility of applying this system for the remote area (or islands) in the south of Iran. In addition, using artificial intelligence methods to predict solar and wind energies, which are used to calculate the energy input to photovoltaic panels and generating power by wind turbines. The targets of this Ph.D. thesis are as follows:

1.1. Refrigeration unit

Maybe a system will be an ideal system from a thermodynamic point of view, but it might not be able to pass the economic and environmental criteria. Also, analysis the systems only by considering the economic criterion, can obtain the cheapest one, but may not be a well-designed one from the thermodynamic and environmental points of view. Thus none of these systems are acceptable from a comprehensive engineering point of view and it needs that a simultaneous consideration of all or some of these criteria might provide a better option for engineers. The goal of this section of Ph.D. thesis are:

1. Energy analysis based on the first law of thermodynamics in order to find the maximum coefficient of performance of the proposed systems.
2. Exergy analysis of the systems in order to determine the exergy destruction of the systems and also for each component of the systems.
3. Environmental analysis for the proposed systems.
4. Thermo-economic analysis based on the second law of thermodynamics for the proposed systems.
5. To determine the sizing of the components such as evaporator, condenser, and ejector device.

Contribution:

Regarding the literature review, the extensive research carried out on the performance of the EERS with the constant area for ejector device based on the energy analysis. In this study, the performance of the EERS and ejector design under different operating conditions and for the first time by considering the economic and thermodynamic parameters simultaneously carried out. Thus far, the ejector device was applied in transcritical CO_2 cycle, domestic refrigerators and freezers, this Ph.D. thesis concentrates on the EERS in real conditions for large-scale refrigeration system for supplying the cold water (high temperature in condenser and evaporator). Also, there is no detailed thermo-economic assessment on the EERS in order to design the components. Based on the literature, more the proposed thermo-economic analysis methods have considered only the initial capital cost and costs of the input exergy of the system. Due to the large capacity of the unit, in this study TRR method is considered as thermo-economic analysis method in which all the costs, including return on investment, equipment, and fuel purchase prices and the total revenue requirement are calculated annually.

The main goal of this section is to find the more efficient refrigeration system with the optimum working fluid for supplying the cold water for the refinery.

1.2. Artificial intelligence methods

1.2.1. Solar radiation prediction

Between renewable energy resources, solar energy has a high potential in Iran. This country with 300 clear sunny days for a year and average 2200 kWh/m^2/year solar radiation is especially important to use solar systems [23]. In the south of Iran there are several Islands that because of remarkable potential of the solar energy in these regions, it is proposed to use solar energy systems for providing the electrical energy. Prediction of the solar radiation is useful for grid operators in order to make decisions of grid operation, as well as, for electric market operators. In addition energy producers and to negotiate contracts with financial entities or utilities that distribute the produced energy also use of this solar prediction. The goals of this study are:

1. To develop a multilayer feed-forward neural network (MLFFNN) in order to predict the solar radiation in the study zone.
2. Using radial basis function neural network (RBFNN) to forecast the hourly solar radiation.
3. To develop a support vector regression (SVR) model to estimate the hourly solar radiation.
4. Prediction of solar radiation using fuzzy inference system (FIS).
5. To develop adaptive neuro-fuzzy system (ANFIS) for predicting the solar radiation.

1.3.2. Wind speed prediction

The fossil fuel energy resource is gradually being replaced by renewable energy in the world. The sources of fossil fuel energy are limited and use of this resources causes the environmental pollutions and depletion of ozone layer [24]. Iran has primarily relied on a fossil fuel-based energy sector to make its country powerful. With looking at the meteorological data in Iran, it can be understood that there is a powerful potential for using the wind energy in this country. With considering these subjects, this Ph.D. thesis has been encouraged to evaluate the wind energy in the south of Iran. The goals of this study are:

1. To design an MLFFNN to predict the wind speed and its direction with several data training algorithms to identify the better one.
2. The implementing of SVR model for forecasting the wind speed with different time series data.
3. Using ANFIS model to predict the wind speed data in the study region.

Contribution:

Machine learning algorithms were applied to predict the solar and wind energy in the case study zone. This Ph.D. thesis evaluated some machine learning algorithms like multilayer feed-forward neural network, radial basis function neural network, support vector regression model, fuzzy inference system, and adaptive neuro-fuzzy inference system in order to predict the solar radiation and wind speed datasets in the study region. The more efficient method will be introduced for predicting the targets. A comparison between the developed models is done in order to find the best performance. Also, forecasting models are developed for the first time in the south of Iran to predict wind speed and solar energy.

The main goal of this section is to propose the optimum intelligent model for prediction of solar radiation and wind speed.

1.3. Hybrid renewable energy system

The hydrogen energy storage system is especially attractive for remote communities which are not connected to a utility grid. For remote areas, the value of solar/wind energy is extremely high and because of the difficulty and expense of bringing in fuel or building a power line, the renewable hydrogen system can supply energy with locally available renewable sources. In this study, a hybrid renewable energy with hydrogen storage system for supplying the electrical energy for Unit 132 of the second refinery of South Pars in Bushehr (Iran) is proposed. PV panel, wind turbine, electrolyzer, fuel cell, hydrogen tank, and converter are considered for this system. The goals of this section of the Ph.D. thesis are:

1. To find the pattern of produced power for photovoltaic and wind turbine systems in the study zone with dynamical modeling of solar radiation and wind energy.
2. Energy analysis for the photovoltaic system in order to find the produced pattern of photovoltaic systems in the case study region.
3. Finding the optimum slope and azimuth angles for solar collectors for the study zone.
4. Energy analysis for the wind turbine system in the case study region.
5. Exergy analysis for the wind turbine system in the study zone.
6. To determine the pattern of produced power for the photovoltaic and wind energy systems.
7. Energy, exergy, and economic analysis for the hybrid renewable energy with hydrogen energy storage system.

Contribution:

Although some studies investigated hybrid renewable energy systems with hydrogen energy storage, based on a comprehensive literature review that has been done for hybrid renewable energy with hydrogen energy storage systems most of the studies are in small applications and this study focus on a large hydrogen energy storage system with the constant demand load. Also, this analysis for the first time is carried out for the south of Iran and the energy storage pattern was found for this area. In the south of Iran, there are a lot of remote area and several islands, which the proposed system can be applied for this regions.

The main target of this section is to investigate a dynamic model of the renewable energy system for supplying the electrical energy in the case study region.

1.4. Scope

This thesis in the first section concentrates on ejector expansion refrigeration system and evaluates the technical and economic status and prospects of the system components. The proposed system can be used in food processing, preservation and distribution; chemical and process industries; special applications such as cold treatment of metals, medical, construction, ice skating; comfort air-conditioning; and supplying the cold water in large-scale industrial applications. The second section machine learning algorithms are applied to predict the solar and wind energy for the

study zone. These proposed models can be used to predict the solar and wind energy in the other regions in the world. The predicted data are used to calculate the produced power by wind turbines and photovoltaic panels. The third section defines and assesses a hybrid renewable energy with hydrogen energy storage system that is suitable for the remote area applications. The proposed system concentrates on solar and wind energy in the south of Iran, which in this region there are a lot of remote areas and islands that proposed system can be used for this regions. Also, the potential of solar and wind energy for the study zone will be evaluated.

1.5. Methods and Outline

This Ph.D. thesis is developed based on a literature review and experiences from relevant projects all over the world. For designing the refrigeration systems:

1. EES software is used to obtain the operating condition of the proposed systems.
2. Energy, exergy, economic, and environmental analyses of the proposed systems were implemented by developing some algorithms in the Matlab software.
3. Solar and wind analysis of the hybrid renewable energy system is based on the data that provided by NASA[25].
4. The first and second law of thermodynamics are used to evaluate the hybrid renewable energy system.
5. For implementing the machine learning algorithms Matlab software is used. A three layer feed-forward neural network, a radial basis function neural network, fuzzy inference system, support vector regression model, and adaptive neuro-fuzzy inference system are applied to predict the solar radiation. Also, a three layer feed-forward neural network, support vector regression and adaptive neuro-fuzzy inference system models are used to estimate the wind speed data in the study zone.

Chapter 2
Literature Review

2.1. Refrigeration system

World energy consumption is increasing continually and this event is worrisome for all researchers and scientists [3]. The increase in energy demand, depletion of fossil resources and environmental pollution problem have led to a growth of interest in more efficient systems. Therefore, efforts to reduce high-grade energy consumption are necessary and it is useful to develop innovative alternatives in technologies that involve large amounts of power consumption, such as vapor compression refrigeration system [26]. This type of cooling systems are more popular in Iran and optimization of these systems will be helpful for energy saving. As an example, one can consider alternative ejector refrigeration system (ERS). The role of energy and exergy analysis for defining the cost and benefits in refrigeration systems was shown with the thermo-economic analysis that is based on the second law of thermodynamics. The optimum conditions for thermodynamic and economic performance of the system are achieved by considering the economic and thermodynamic parameters simultaneously [27]. Maybe a system will be an ideal system from a thermodynamic point of view, but it might not be able to pass the economic and environmental criteria. Also, analysis the systems only by considering the economic criterion can obtain the cheapest one, but may not be a well-designed one from the thermodynamic and environmental points of view. Thus none of these systems are acceptable from a comprehensive engineering point of view and it needs that a simultaneous consideration of all or some of these criteria might provide a better option for engineers.

With the introduction of EERS for the first time by Kornhauser [28] in 1990, studies in this area have seen a growing trend. Some of the investigations have proposed ejector instead of the expansion device in refrigeration systems [29]–[32]. Two-phase flow ejector device was proposed instead of the expansion device in refrigeration cycle (RC) by Hassanian et al. [33]. It is found that ejector device is an efficient way to enhance the performance of the system. The coefficient of performance (COP) increased approximately 88% as evaporation temperatures changed from -10℃ to 10℃. Wongwises et al. [34] conducted an experimental investigation on EERS in a transcritical CO_2 refrigeration system. It was found a higher cooling capacity and COP, as a result of using ejector as a new expansion device. Zheng et al. [35] developed a dynamic model for a CO_2 transcritical EERS. Evaporator, gas cooler and separator were formulated by using the mass and energy conservation laws. They illustrated that the area ratio of the ejector has greater effect on gas cooler pressure. Also, the mass flow rates decrease if the area ratio of ejector increases. Li et al. [36] evaluated EERS with R1234yf as working fluid. The constant evaporation temperature (5℃) and the constant condensing temperature (40℃), COP, and volumetric cooling capacity (VCC) were analyzed in their study. It was observed that COP and VCC in EERS were improved in comparison to a standard refrigeration system. Thongtip et al. [37] evaluated the performance of an ejector that was applied in R141b jet-pump refrigeration system. They provided the optimum range of primary mass flow rate and critical evaporator temperature for the proposed ejector system.

7

On the other hand, some studies evaluated thermo-economic analysis in refrigeration systems. Farsi et al. [38] evaluated thermo-economic analysis on ejector supercritical refrigeration system. For economic analysis, it is considered the operating and maintenance costs and the capital investment cost of the component. Thermo-economic optimization results illustrated that COP and exergy efficiency improve about 12% and 8%, respectively. Exergoeconomic analysis and multi-objective optimization for an ejector refrigeration cycle (ERC) powered by an internal combustion engine have been investigated by Sadeghi et al. [39]. Thermodynamic analysis, exergoeconomic and multiobjective optimization were implemented for the ERC in order to obtain the optimum design variables. Several design parameters such as the condenser, evaporator and generator temperatures are examined on the thermodynamic and exergoeconomic performances. Their results showed the best performance obtained when the ejector refrigeration system works at a generator, a condenser and evaporator temperatures of 94.54, 33.44 and 0.03℃, respectively. Exergoeconomic analysis of CO_2 transcritical refrigeration system (TRS) was done by Fazelpour et al. [40]. They used an economizer as an auxiliary component for one-stage CO_2 TRS that this machine helps them to decrease the total cost by about 14%. Rezayan et al. [41] evaluated thermo-economic analysis of CO_2/NH_3 cascade refrigeration system. By the input exergy cost and capital cost for the systems, the optimum evaporation and condensing temperatures were found in their study. It should be noted that finding the size of the components is important for thermo-economic analysis which is done in this study. Shell and tube evaporator and compact air-cooled condenser were considered for the proposed systems in this study. Comprehensive methods in order to design the heat exchangers are introduced by Thulukkanam [42] and Lee [43]. An ejector expansion device is divided into three sections known as diffuser, mixing section and motive nozzle. To determine the size of the ejector device some methods were proposed by [33], [44], [45]. Based on the literature review for the ejector in refrigeration systems, it can be said that many studies proposed an ejector in transcritical CO_2 refrigeration systems [30], [46]–[50], domestic refrigerators [36], [44], [51]–[58], and domestic refrigerator-freezers [31], [59]–[61].

2.2. Artificial intelligence methods

2.2.1. Wind speed prediction

Wind energy is one of the most common of clean energies that has been developed significantly in the world [62]. This type of energy is more accessible, inexhaustible, fairly cheaper, renewable and sustainable, and environmentally friendly. Wind energy is a free source of energy that has served the mankind for many countries for driving wind turbines, pumping water, ships, etc. Developing wind energy systems can improve the idea of electricity generation without pollution in the future [63]. However, the integration of wind farms into the power networks has become an important problem for commitment and control of power plants, connecting and disconnecting the power to the grid and management of the power [64]. The produced power by wind turbine is related to the wind speed. Wind is considered one of the weather variables which more difficult to be estimated [65]. Wind is intermittent in nature, so it is not possible to predict exact wind speed because of the continuously changing climate conditions.

Therefore, the advent of alternative energy sources, particularly wind power, and the need to manage energy resources necessitate the use of advanced tools for prediction of short-term wind speed (or other types of renewable energies) [66]. The contribution of wind speed prediction for a safe and economic operation of the network will organize by

independent power producer, system operator distribution and electrical companies. In recent years many investigations have proposed machine learning algorithms (MLAs) (or Artificial Intelligence methods) to predict the variation of meteorological data such as wind speed, solar irradiance, relative humidity, air temperature and etc. [11], [13], [67]–[72]. Artificial Intelligence methods are defined as an extensive scientific discipline which enable computer programs to solve the complex nonlinear problems. In this study, four types of MLAs are implemented to predict the wind speed data. It is exposed the procedure to achieve the possible models which better explain the wind speed behavior. These methods are described as follows:

The first method is multilayer feed forward neural network (MLFFNN) that is defined as a new method of programming computers. This method is employed to analyze the problems that are very difficult to solve using conventional techniques [73]. The second method is support vector regression (SVR) that optimize its structure based on the input data. This method has been introduced by Vapnik [74], which works based on the classification and regression technique. In recent years, SVR was successfully employed on classification tasks in very different areas of application [75]–[78]. The third method is adaptive neuro-fuzzy inference system (ANFIS). An ANFIS model is defined as a combination of an ANN (generally, radial basis function neural network) into a fuzzy inference system. This combination is carried out to obtain the knowledge of the human expert to adjust the fuzzy parameters. The fourth method is the combination of particle swarm optimization (PSO) algorithm with ANFIS model (ANFIS-PSO). The PSO algorithm is employed to increase the performance of the ANFIS model, tuning the membership functions required to achieve a lower error. This optimization algorithm that was proposed by Kennedy and Eberhart in 1995 is a heuristic approach [79].

Chang et al. [80] developed a radial basis function neural network (RBFNN) for short-term wind speed and power forecast. The proposed network was trained with 24 h of observation period with historical data. Also, their method was compared with other methods of neural networks. They obtained the mean absolute percentage error (MAPE) for backpropagation neural network (BPNN), RBFNN and ANFIS as 27%, 24% and 3.87%, respectively. Ramasamy et al. [15] proposed an artificial neural network (ANN) to estimate wind speed in the mountains region of India. Temperature, solar radiation, air pressure and altitude were selected as inputs of the model and mean daily wind speed was selected as the target. It was reported a MAPE and correlation coefficient around 4.55% and 0.98, respectively. Doucoure et al. [21] implemented wavelet neural network and multi-resolution analysis to forecast wind speed.

Liu et al. [81] developed a modified Taylor Kriging method in order to estimate wind speed time-series data. One-year wind speed data were divided into 10 samples and the proposed model was applied to each sample. The proposed method was compared with an autoregressive integrated moving average method (ARIMA) and the results illustrated that the proposed method outperformed the ARIMA method by 18.6% and 15.2% in term of mean absolute error (MAE) and root mean square error (RMSE), respectively. Noorollahi et al. [82] used ANNs for estimating temporal and spatial wind speed in Iran. They implemented BPNN, RBFNN and ANFIS models to predict the targets. The BPNN and ANFIS models yielded similar results. The RBFNN method illustrated larger errors in all cases. Schicker et al. [83] developed an interval-artificial neural network for short-term wind speed prediction.

9

Kumar et al. [84] proposed generalized regression neural network (GRNN) and multilayer perceptron neural network (MLPNN) in order to predict wind speed in Western Region of India. It was found that the GRNN model has given the better result than MLPNN in term of mean square error (MSE). Sheela et al. [85] proposed neural network based on hybrid computing model for wind speed prediction. The proposed model was compared with an MLPNN and the results demonstrated the hybrid computing model performed better in terms of minimization of errors. Petkovic [86] implemented an ANFIS method for estimation of wind speed distribution. It was achieved an improvement in predictive accuracy and capability of generalization with the ANFIS approach.

Bonfil et al. [87] developed a model based on SVR to predict wind speed for wind farms. Wavelet, extreme learning machine and outlier correction algorithm were developed in order to predict wind speed by Mi et al. [88]. Also, Liu et al. [71] applied secondary decomposition algorithm and Elman neural networks for forecasting wind speed data. It was achieved a satisfactory performance for the proposed method in multi-step wind speed prediction. Li et al. [89] developed a study based on three models of ANN to predict wind speed data. These methods were adaptive linear element, backpropagation and radial basis function neural network. It was observed that the three developed models were capable at wind speed prediction. Koo et al. [90] employed ANN to predict wind speed data based on geological and distance variables (a case study in South Korea).

Lodge and Yu [91] implemented an ANN to predict the short-term wind speed data. This model was constructed based on the current weather condition and historical wind speed data. The values of RMSE for training and testing datasets were determined as 0.5781 (m/s) and 0.8895 (m/s), respectively. Mohandes et al. [92] developed a support vector machine (SVM) for forecasting the wind speed data and compared to an MLP neural network. For testing datasets, the value of MSE for SVM and MLP models were obtained 0.0078 and 0.0090, respectively. Bilgili et al. [93] used MLP neural network in order to forecast wind speed data. To train the network, resilient propagation (RP) learning algorithm was employed. Also, *logsig* and *purelin* transfer functions were selected for the hidden and output layers, respectively. The MAPE for the developed model was obtained 14.13%.

Salcedo-Sanz et al. [94] developed evolutionary support vector regression algorithms to estimate short-term wind speed prediction. An Evolutionary Programming algorithm (EP) and particle swarm optimization algorithm (PSO) were applied to tackle the hyper-parameters estimation problem in regression SVM. Their results have shown that the new model based on SVM with EP algorithm outperformed the MLP neural network. Liu et al. [95] proposed two models of ANN to predict the wind speed data. The first model was SVM optimized with genetic algorithm (SVM-GA) and the second one was a combination of wavelet transform with SVM-GA model (W-SVM-GA). It was obtained that the W-SVM-GA performed better than the SVM-GA in terms of MAPE and RMSE.

2.2.2. Solar radiation prediction

Renewable energy resources, particularly, solar energy is being replaced with the fossil fuel resources [96], [97]. Accurate prediction of solar irradiance data is an important issue towards the successful planning of renewable energy projects [98]. Vast applications in the field of agriculture, heating and cooling systems, ventilation and electrical energy production use solar energy. Generally, solar radiation data are measured by pyrheliometer, pyranometer and

sunshine duration meter. But, installation of these devices for each station is very expensive. In addition, due to the low accuracy of these devices, the missing data have been found. Therefore, the accurate prediction of solar irradiance data is important for solar energy researches [99]. In recent layers, many investigations utilized artificial intelligence methods to predict the solar radiation data [100], [101], which a summary of them are described as follows:

Loghmari et al. [102] compared the performance of two global solar radiation models (an Artificial Neural Network (ANN) and Inverse Distance Weighting based model (IDW)) for spatial interpolation purposes. The available meteorological data was used by the ANN model to predict global solar radiation. Global solar radiation measured in the neighboring regions were used by the IDW model to predict the target. It was obtained the average relative root mean square error for the ANN and IDW models as 6.4% and 5.11%, respectively. Kashyap et al. [103] developed a model based on ANN with backpropagation algorithm for solar radiation forecasting. The predicted model was initiated and validated with 10 meteorological parameters further in sub-categories. They concluded that the best results for the developed model were obtained with the delays of 15 or 30, transfer function as *tansig*, the number of neurons in the hidden layer as 10 or 20. For this model, the value of RMSE was obtained around 25-35%. Wu et al. [104] developed a new model based on a genetic approach combing multi-model framework in order to solar radiation time series prediction. Several patterns in the stochastic solar radiation series were assumed by them in which a genetic algorithm was applied to find the optimal segment of the solar radiation series. It was obtained that the proposed model outperformed the autoregressive moving and average model (ARMA) and time delay neural network (TDNN). Meenal and Selvakumar [105] compared the performances of the support vector machine (SVM), ANN and empirical solar radiation models by considering the different combination of input variables. The input parameters were selected to be month, latitude, longitude, bright sunshine hours, day length, relative humidity, maximum and minimum temperatures. This study was done in order to predict the monthly mean daily global solar radiation (GSR) for various stations in India. They obtained that the SVM model with most influencing input parameters performs better than the ANN and empirical models.

Olatomiwa et al. [106] used an ANFIS model to estimate solar radiation in Nigeria. This model was developed based on a series of measured meteorological data that were monthly mean minimum and maximum temperatures, and sunshine duration. The root mean square error (RMSE) and determination coefficient (R^2) for training and testing phases of the model were obtained as 1.0854 and 0.8544, and 1.7585 and 0.6567, respectively. An ANN model was developed for prediction of monthly average daily global solar radiation by Alsina et al. [107]. This study was developed for prediction of solar radiation over Italy. To construct the model, 13 input parameters were considered and the results have shown the mean absolute percentage error (MAPE) of the model, ranges between 1.67% and 4.25%.

Wang et al. [108] conducted a study for prediction of solar radiation that compares three types of ANN methods. Multilayer perceptron (MLP), generalization regression neural network (GRNN) and RBFNN were applied to estimate the daily global solar radiation. The models were developed based on the air temperature, relative humidity, air pressure, water vapor pressure and sunshine duration hours measured at 12 stations in different climate zones as input variables. It was found that MLP and RBFNN models provide better accuracy than the GRNN. A SVM was applied

11

for prediction of daily and mean monthly global solar radiation in an arid climate (Ghardaia, Algeria) by Belaid and Mellit [109]. For this model, the inputs were selected to be the ambient temperature, maximum sunshine duration and extraterrestrial solar radiation. For the developed SVM model the correlation coefficient varied from 0.894 to 0.896. Also, this model performed better than an MLP. Mehdizadeh et al. [110] developed a study based on Gene Expression Programming (GEP), ANN, ANFIS and 48 empirical equations in order to estimate daily solar radiation in Kerman, Iran. They reported that the meteorological parameters-based and sunshine-based scenarios in ANFIS and ANN presented high accuracy compared to the empirical models.

2.3. Hybrid renewable energy system

The main problem to utilize the solar and wind energies is the great variation in available power which occurs from season to season, day to day, hour to hour. This would not be a problem if the load was well correlated to the energy availability, but unfortunately, this is not often the case. Efficient storage is essential for large-scale exploitation of intermittent renewable sources. Today most renewable electricity systems use battery as storage system [111]. This type of storage is expensive and large per unit of stored energy but has the advantage of high efficiency. Batteries can be used for short-term storage, but in order to keep the solar/wind power system dependable, a relatively large number of batteries will generally be needed [112]. This can result in high costs. Until now, one of the key factors constraining the advantage of renewable power sources has been the inability of batteries to store enough electricity to provide user needs during extended periods of calm or cloudy days. The introduction of hydrogen will help to overcome the storage difficulty of renewable energy. Hydrogen can be easily produced by electricity via electrolysis and reconverted to electricity by fuel cell power plants [113].

In recent years several studies have been conducted on hydrogen energy storage system for renewable energies. Energy and exergy analysis of a solar system with hydrogen storage unit was done by Ozcan et al. [114]. Kotowicz et al. [115] developed a methodology to obtain the efficiency of a hydrogen generator as a system for storage of renewable-generated energy. Uyar et al. [116] investigated a model of renewable energy system integrated to a hydrogen storage unit for better design of 100% renewable energy communities. They showed the role of hydrogen and fuel cell for supplying the required energy in transportation sectors as a clean energy system. Calderon et al. [117] proposed a PV/wind system with hydrogen storage performance to provide the electrical energy in Badajoz, Spain. The proposed system was evaluated based on an exergy analysis. They obtained a low exergy efficiency for the PV modules (8.39%) in Badajoz.

Kalinci et al. [118] evaluated energy and exergy analysis of a hybrid hydrogen energy system and applied it for Bozccada, Turkey. Marchenko et al. [119] investigated a PV/wind energy system on the Baikal Lake. They proposed a system using PV panels and wind turbine for supplying the electric power and electrolyzer, hydrogen tank and fuel cell as energy storage system. Khalid et al. [120] analyzed a renewable energy based integrated photovoltaic system (PVS) and wind turbine system (WTS) to provide electrical energy for residential applications. They used the excess electricity generated to produce hydrogen through electrolyzer and using hydrogen generated by fuel cell during peak demand periods. The overall energy and exergy efficiencies of this system were reported as 26% and 26.8%, respectively. Also, Caliskan et al. [121] investigated a hybrid renewable energy based hydrogen energy storage.

12

Energy and exergy analysis of this system has been evaluated by them. It is found the average energy efficiency for WT, PV array, electrolyzer and fuel cell by 26.15%, 9.06%, 53.55% and 33.06%, respectively.

In the areas which are connected to the grid, it is certainly not worthwhile to use the renewable hydrogen system nowadays. It is an environmentally friendly system but too costly. However in the more areas where no connection to utility grid, the renewable hydrogen system is an attractive solution. Gonzalez et al. [122] evaluated a solar hydrogen storage system and compared it with other electrical energy storage technologies. In their study, hydrogen energy storage system was classified between 100 kW and 100 MW power rating. A solar electricity supply system with seasonal hydrogen storage to supply a constant load was proposed by Andrews et al. [123]. Finding a more efficient energy storage system for a long-time is essential because throughout the world there are hundreds of thousands of villages, remote communities and islands which do not have power or are supplied on an individual basis by small gas or diesel generator sets, small WTs and PV systems. Smaoui et al. [124] presented optimal sizing of stand-alone PV/wind/hydrogen hybrid system in a desalination unit. It is proposed a methodology to find the optimal technical-economic configuration among a set of systems components. Also, for a desalination unit in stand-alone region in Iran a cost-effective wind/PV/hydrogen energy system was proposed by Maleki et al. [125]. This system was designed for increasing the freshwater availability and to provide the load demand.

The barrier of the applications of hydrogen system is its high costs in its early development stage. Economically this system cannot compete with traditional energy systems in most cases. Hence, some researchers are working to improve the hydrogen energy storage systems. Singh et al. [126] proposed a techno-economic feasibility analysis for a hydrogen fuel cell and PV hybrid renewable energy system. The proposed system was applied for the academic research building, in India. Nguyen et al. [127] developed an optimal capacity design of battery and hydrogen storage system for a PV renewable energy system. A technical feasibility and financial analysis for PV/wind hydrogen system were done by Shakya et al. [128]. This system was evaluated with PV% of 0, 12, 60, and 100 configurations in which the lowest levelized energy cost was obtained for 100% PV.

13

Chapter 3
Material and methods

Fig. 3.1 presents the target of this Ph.D. thesis. Designing a refrigeration system to supply the cold water for the refinery. The electrical energy of this unit is provided by considering a hybrid photovoltaic/wind turbine energy system with hydrogen storage system. In this system, artificial intelligence methods are employed to predict the solar radiation on the collectors. Intelligent models are developed based on the ambient temperature, pressure, relative humidity, wind speed and local time as input variables. The predicted solar radiation data are used to calculate the energy input to the photovoltaic panels. Also, artificial intelligence methods are applied to predict the wind speed using meteorological data. The estimated wind speed data are employed to calculate the generating power by wind turbines. Ambient temperature, pressure, relative humidity and local time are selected as input variables of the models.

3.1. Refrigeration system (Unit 132 of the refinery)

Unit 132 of the second refinery of the South Pars (Iran) has been considered in order to supply the cold water for the refinery. Indeed, this unit is responsible for delivering 39 kg/s cold water for cooling the equipment in the refinery. The hot water enters into the evaporator at 40 °C and leaves it at 30 °C. The cooling capacity of this process is 1631 kW. For this target, three refrigeration systems are proposed and designed to provide the cold water for the refinery. The first one is a basic refrigeration system (BRS), the second one is a basic refrigeration system with an internal heat exchanger (HXRS), and the third one is an ejector expansion refrigeration system (EERS) (these system are shown in Figs. 3.2-3.4).

Fig. 3.2 presents a BRS (and its P-h diagram) with four main components that are evaporator, condenser, expansion valve and compressor. Fig. 3.3 illustrates the HXRS (including five components that are compressor, condenser, evaporator, internal heat exchanger and expansion valve) accompanying with its P-h diagram. Indeed, this system is a standard refrigeration system with an internal heat exchanger, which this internal heat exchanger is used for sub-cooling and superheat processes respectively at the outlet of condenser and evaporator. P-h diagram of the cycle shows the superheat and sub-cooling processes are 1 to 2 and 4 to 5, respectively. An EERS is shown in Fig. 3.4 (components: evaporator, condenser, compressor, expansion valve, ejector expansion and separator) and this system is proposed for the refinery instead of the HXRS. Ejector expansion in vapor compression refrigeration system was first proposed by Kornhauser [28]. Ejector expansion compression cycle reduces the work of compression, which increases the COP of the system.
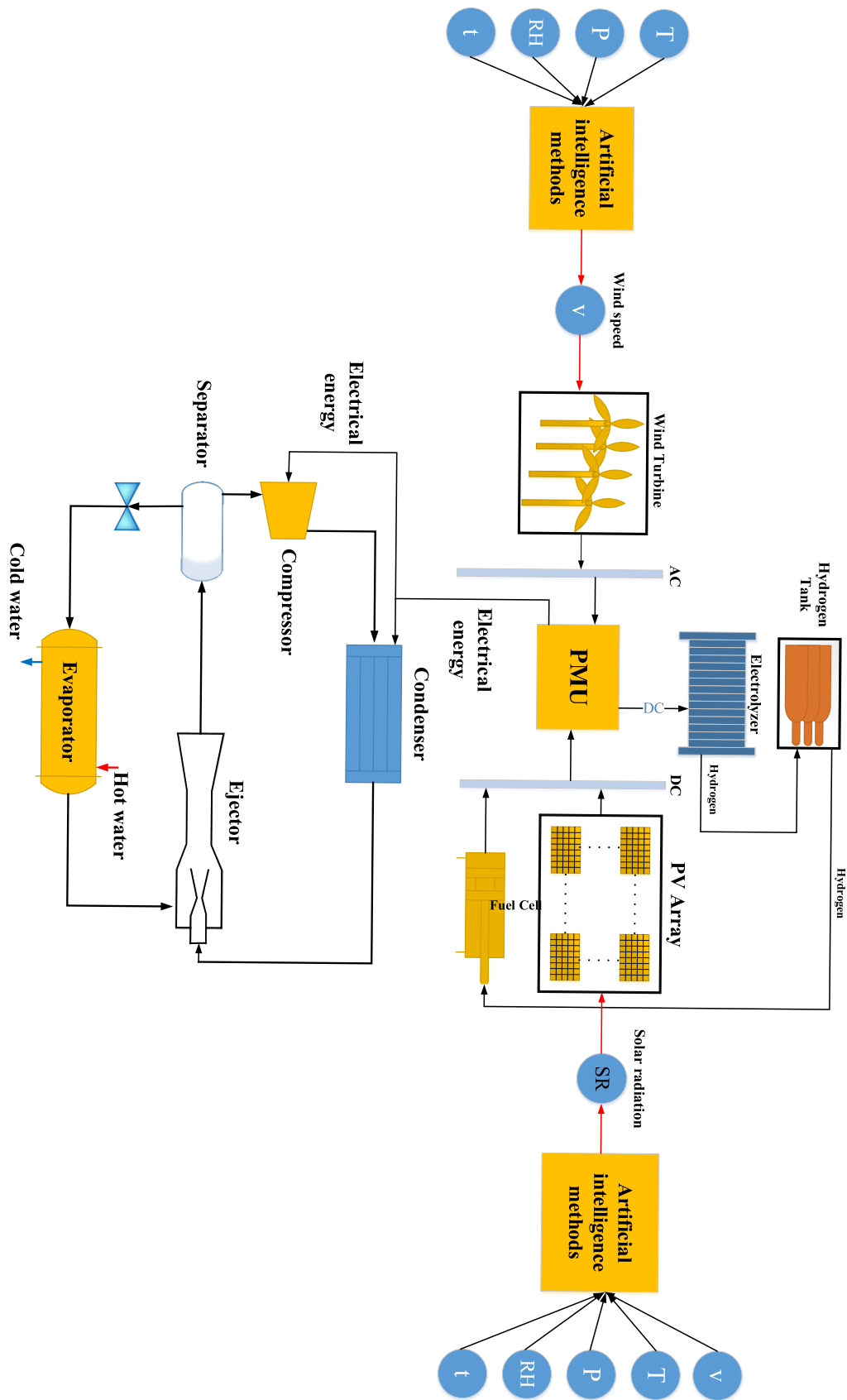
Fig. 3.1. A schematic diagram of the system.
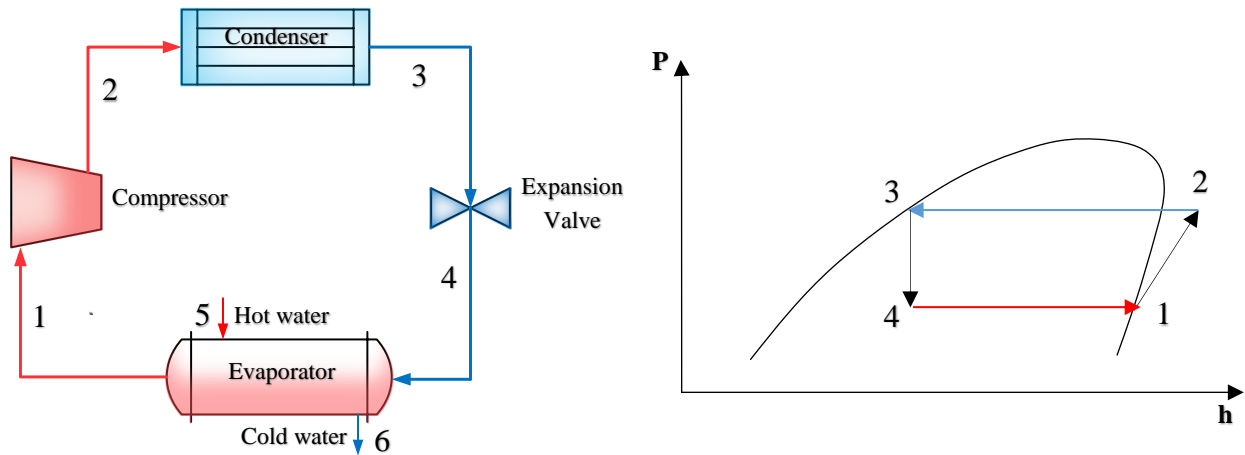
Fig. 3.2. A schematic diagram of a BRS with its P-h diagram.
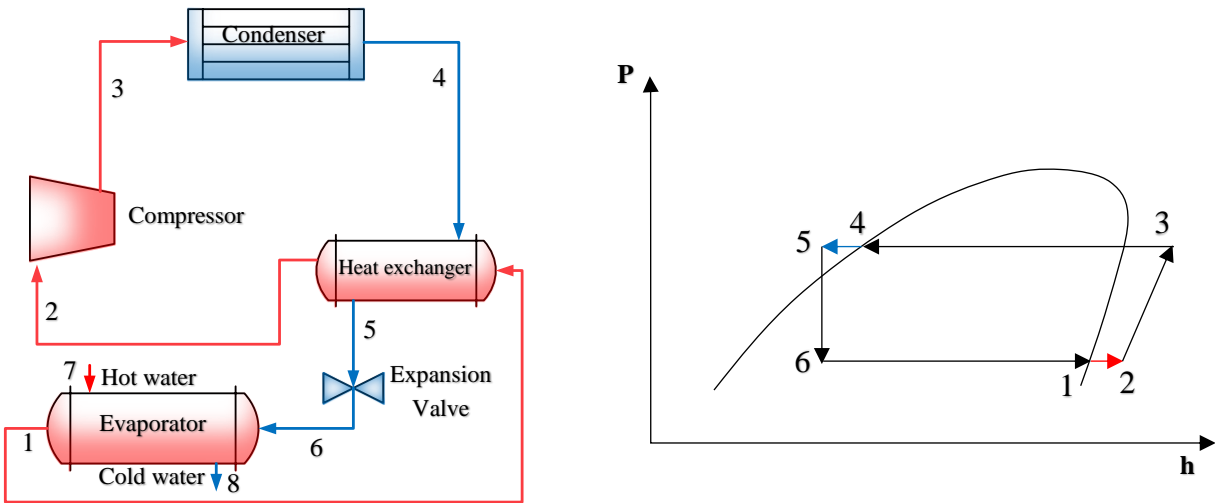
Fig. 3.3. A schematic diagram of an IHERS and its P-h diagram.

Saturated vapor and saturated liquid are considered in the outlet of evaporator and condenser, respectively. By having the amount of the condensing and evaporating temperatures, all the thermodynamic properties are determined in the evaporator and condenser. Also, by applying a mathematical model (Eqs. (3.1)- (3.51)) in Engineering Equation Solver (EES) software the values of thermodynamic properties in all points that are shown in Figs. 3.2-3.4 are obtained. Tables 3.1-3.3, show operating conditions for BRS, HXRS and EERS. Temperature, pressure, specific enthalpy, specific entropy and quality of vapor are calculated for each point of the cycles. Design conditions of the cycles are constant in all three systems.

16
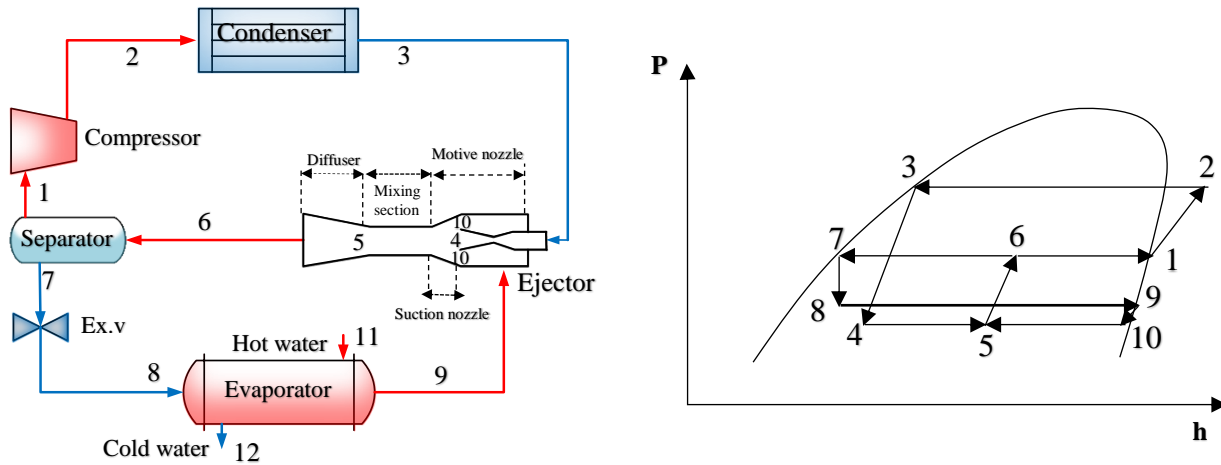
Fig. 3.4. EERS and P-h diagram of the cycle.

Table 3.1. Operating conditions for SRS (Fig. 1).

Point	T [°C]	P [kPa]	h [kJ/kg]	s [kJ/kg K]	x(%)
1	24	646.2	263.7	0.9209	100
2	68.35	1750	287.9	0.9325	-
3	61.66	1750	142.1	0.4971	0
4	24	646.2	142.1	0.5117	31.95

Table 3.2. Operating conditions for IHERS (Fig. 2).

Point	T [°C]	P [kPa]	h [kJ/kg]	s [kJ/kg K]	x(%)
1	24	646.2	263.7	0.9209	1
2	33.95	646.2	273.7	0.954	-
3	81	1750	299.6	0.9661	-
4	61.6	1750	142.1	0.4971	0
5	55.47	1750	131.9	0.4666	-
6	24	646.2	131.9	0.4776	26.27

Table 3.3. Operating conditions for EERS (Fig. 3).

Point	T [°C]	P [kPa]	h [kJ/kg]	s [kJ/kg K]	x(%)
1	26.94	705.1	265.2	0.9198	1
2	67.75	1750	287.1	0.9302	-
3	61.66	1750	142.1	0.4971	0
4	22.96	626.2	138.9	0.5017	30.84
5	22.96	626.2	190.8	0.6771	59.75
6	26.94	705.1	192.6	0.678	58.48
7	26.94	705.1	89.17	0.3335	0
8	24	646.2	89.17	0.3337	2.347
9	24	646.2	263.7	0.9209	1
10	22.96	626.2	263.1	0.9212	99.99

3.1.1. Energy and exergy analysis of the systems
Analysis for HXRS:

The operating conditions for the cycles of the BRS and HXRS are obtained with the simulation in EES software.

Moreover, for analysis of each component mass conservation law, the first and second laws of thermodynamics are

applied for each control volume. Eqs. (3.1)- (3.4) show the energy and exergy analysis for evaporator and heat exchanger in HXRS.

$$\dot{Q}_{evap} = \dot{m}_f(h_1 - h_6) = \dot{m}_w\, Cp_w(T_{w8} - T_{w7}) \tag{3.1}$$

$$\dot{I}_{eva} = \dot{m}_f[(h_1 - h_6) - T_0(S_1 - S_6)] - \dot{m}_w[(h_{w7} - h_{w8}) - T_0(S_{w7} - S_{w8})] \tag{3.2}$$

$$\dot{Q}_{H.E} = \dot{m}_f(h_2 - h_1) = \dot{m}_f(h_5 - h_4) \tag{3.3}$$

$$\dot{I}_{H.E} = \dot{m}_f\big[[(h_5 - h_4) - T_0(S_5 - S_4)] - [(h_2 - h_1) - T_0(S_2 - S_1)]\big] \tag{3.4}$$

For expansion valve:

$$h_6 = h_5 \tag{3.5}$$

$$\dot{I}_{ex.v} = \dot{m}_f[T_0(S_6 - S_5)] \tag{3.6}$$

For compressor:

$$\dot{w}_{comp} = \dot{m}_f(h_2 - h_1) \tag{3.7}$$

$$\dot{I}_{comp} = \dot{m}_f[T_0(S_2 - S_1)] \tag{3.8}$$

Finally, for condenser:

$$\dot{Q}_{cond} = \dot{m}_f(h_3 - h_2) \tag{3.9}$$

$$\dot{I}_{cond} = \dot{m}_f \times T_0\left[\frac{(h_3 - h_2)}{T_{cond}} - (S_3 - S_2)\right] + \dot{w}_{fan,cond} \tag{3.10}$$

Analysis for EERS:

Also, energy and exergy analysis for EERS have been given by Eqs. (2.11)- (2.30). Saturated liquid and saturated vapor are considered for EERS in the outlet of the condenser and evaporator respectively and by having evaporating and condensing temperature, thermodynamic properties will be obtained in points 3 and 9 of the cycle in EERS, which was shown in Fig. 3.4. Governing equations of energy and exergy analysis of the compressor are defined by following equations:

$$h_{2,is} = h(p_2, s_1) \tag{3.11}$$

$$\eta_{is,comp} = (h_1 - h_2)/(h_1 - h_{2,is}) \tag{3.12}$$

$$\eta_{is,comp} = 0.874 - 0.0135(p_{cond}/p_{eva}) \text{ [129]} \tag{3.13}$$

$$\dot{w}_{comp} = \dot{m}_3((h_2 - h_1)/(1 + \omega)) \tag{3.14}$$

$$\dot{I}_{comp} = \frac{\dot{m}_6}{\omega + 1}[T_o(s_2 - s_1)] \tag{3.15}$$

Condenser:

$$\dot{Q}_{cond} = \frac{\dot{m}_6}{\omega + 1}[(h_2 - h_3)] \tag{3.16}$$

$$\dot{I}_{cond} = \frac{\dot{m}_6}{\omega + 1}[(h_2 - h_3) - T_o(s_2 - s_3)] \tag{3.17}$$

Expansion valve:

$$h_7 = h_8 \tag{3.18}$$

$$\dot{I}_{ex.v} = \frac{\dot{m}_6\omega}{\omega + 1}T_o[(s_8 - s_7)] \tag{3.19}$$

Evaporator:

18

$$\dot{Q}_{eva} = \frac{\dot{m}_6 \omega}{\omega + 1}(h_9 - h_8) \tag{3.20}$$

$$\dot{I}_{eva} = \dot{m}_9\big((h_8 - h_9) - T_0(s_8 - s_9)\big) - \dot{m}_w\big((h_{11} - h_{12}) - T_0(s_{11} - s_{12})\big) \tag{3.21}$$

Gas-liquid separator:

Saturated vapor and saturated liquid for inlet of compressor and expansion valve respectively are considered and with analysis gas-liquid separator the amount of the specific entropy in points 1 and 7 were obtained.

$$h_1 = h(p_1, saturated\ vapor) \tag{3.22}$$
$$h_7 = h(p_1, saturated\ liquid) \tag{3.23}$$

Ejector:

Exergy analysis in ejector will be introduced by Eq. (3.24).

$$\dot{I}_{eje} = \dot{m}_6 T_o \left[s_6 - s_3 \frac{1}{\omega + 1} - s_9 \frac{\omega}{\omega + 1} \right] \tag{3.24}$$

Area ratio and pressure lift ratio are two useful parameters for designing ejector which are given by Eqs. (3.25) and (3.26), respectively[36]:

$$AR = \frac{A_{10} + A_4}{A_4} \tag{3.25}$$

$$PLR = \frac{p_{eje}}{p_{eva}} = \frac{p_6}{p_9} \tag{3.26}$$

The COP of the cycle is determined by the following relation:

$$COP = \frac{q_{eva}}{w_{comp}} \tag{3.27}$$

Yu JL et al. [130], for the compressor, defined VCC of the cycle based on the specific suction volume:

$$VCC = \frac{\omega(h_9 - h_8)}{v_1} \tag{3.28}$$

3.1.1.1. Heat exchangers design procedure

Evaporator and internal heat exchanger (MHX):

Shell-and-tube heat exchanger is the most common type of heat exchanger in industrial applications. These exchangers hold more than 65 percent of the market share [43]. For evaporator and MHX in the refrigeration system in the refinery shell and tube heat exchanger (STHX) was proposed. Thermal area and pressure loss are important for thermo-economic analysis. Outer diameter (d_o), number of passes (N_p), shell diameter (D_s), tube length (L_t), and diameter ratio ($d_r = d_o/d_i$) are design parameters which were determined by iterations initially. And then the calculations were iterated with different values of parameters until they satisfied the design requirements. The tube pitch ratio P_r is defined by the following equations [43]:

$$P_r = P_t/d_o \tag{3.29}$$
$$B = L_t/(N_b + 1) \tag{3.30}$$
$$C_t = P_t - d_o \tag{3.31}$$

Where L_t, N_b, B, P_t, and C_t are tube length, number of baffles, baffle spacing, tube pitch and tube clearance respectively.

The number of tubes N_t can be predicted in fair approximation with the shell inside diameter D_s:

$$N_t = (CTP) \frac{\pi D_s^2 / 4}{CL. P_t^2}$$ (3.32)

In which, CTP and CL are tube count constant and tube layout constant respectively.

Velocity of the fluid and Reynolds number for tube side are given by following relations:

$$v_i = \frac{\dot{m}_i}{\rho A_{c_i}}$$ (3.33)

$$A_{c_i} = \frac{\pi d_i^2}{4} \frac{N_t}{N_p}$$ (3.34)

$$Re_D = \frac{\dot{m}_i d_i}{A_{c_i} \mu} = \frac{\rho v_i d_i}{\mu}$$ (3.35)

The cross-flow area of the shell side is defined as:

$$A_{c_o} = D_s C_t B / P_t$$ (2.36)

And for shell side the equivalent diameter for the square pitch layout and Reynolds number are defined:

$$D_e = \frac{4 \left(P_t^2 - \pi \frac{d_0^2}{4} \right)}{\pi d_0}$$ (3.37)

$$Re_D = \frac{\rho v_o D_e}{\mu} = \frac{\dot{m}_o D_e}{A_{c_o} \mu}$$ (3.38)

Heat transfer coefficient for inner and outer fluid in shell and tube heat exchanger is determined by Eqs. (3.39)- (3.51).

For outer fluid:

if $Re_D \geq 2300$

$$h_o = 0.023 \, Re_D^{0.8} \, Pr^{0.3} \frac{k}{d_i}$$ (3.39)

Otherwise

$$Nu = 3.657 \text{ or } Nu = 4.364$$ (3.40)

For inner fluid:

if $Re \geq 2300$

$$f = (1.58 \, ln(Re_D) - 3.28)^{-2}$$ (3.41)

Otherwise

$$f = 16 / Re_D$$ (3.42)

Chen correlation for heat transfer coefficient is defined by Eqs. (3.43)- (3.51) [42].

$$h_i = h_{cb} + h_{nb}$$ (3.43)

Where h_{cp} and h_{nb} are heat transfer coefficient of convection boiling and nuclear boiling respectively.

$$h_{cb} = 0.023 \, Re_l^{0.8} \, Pr^{0.4} \frac{k_l}{d_i} . F(1-x)^{0.8}$$ (3.44)

$$Re_l = \frac{G(1-x)d_i}{\mu_l}$$ (3.45)

$$F=1 \quad \text{for} \quad \frac{1}{\chi} \le 0.1 \tag{3.46}$$

$$F = 2.35 \left(\frac{1}{\chi} + 0.213\right)^{0.736} \quad \text{for} \quad \frac{1}{\chi} \ge 1 \tag{3.47}$$

And Martinelli parameter is defined by Eq. (3.48):

$$\chi = \left(\frac{1-x}{x}\right)^{0.9} \left(\frac{\rho_l}{\rho_v}\right)^{0.5} \left(\frac{\mu_l}{\mu_v}\right)^{0.1} \tag{3.48}$$

Also, heat transfer coefficient for nuclear boiling is given by following equations.

$$h_{nb} = 0.00122 \left[\frac{K_l^{0.79} \, cp_l^{0.45} \, \rho_l^{0.49}}{\sigma^{0.5} \, \mu_l^{0.29} \, h_{lv}^{0.24} \, \rho_v^{0.24}}\right] \times (T_W - T_{sat})^{0.24} [(T_W - T_{sat}) \, h_{lv} \, \rho_v / T_{sat}]^{0.75} \, S' \tag{3.49}$$

$$S' = \frac{1}{1 + 2.53 \times 10^{-6} (Re_{TP})^{1.17}} \tag{3.50}$$

$$Re_{TP} = Re_l \, F^{1.25} \tag{3.51}$$

Heat transfer areas of inner and outer surfaces of an inner pipe are given by Eqs. (3.52) and (3.53), respectively.

$$A_i = \pi d_i N_t L \tag{3.52}$$

$$A_o = \pi d_o N_t L \tag{3.53}$$

Overall heat transfer coefficient is defined as [43]:

$$U_o = \frac{1/A_o}{\frac{1}{h_i A_i} + \frac{ln\left(\frac{d_o}{d_i}\right)}{2\pi L k} + \frac{1}{h_o A_o}} \tag{3.54}$$

Pressure drop in shell side is proposed by following relations:

$$\Delta P = f \frac{D_s}{D_e} (N_b + 1) \frac{1}{2} \rho v_o^2 \tag{3.55}$$

$$f = exp\left(0.576 - 0.19 Ln(Re_D)\right) \tag{3.56}$$

As well as the pressure drop in tube side is:

$$\Delta P = 4 \left(\frac{f.L_t}{d_i} + 1\right) N_p \frac{1}{2} \rho v_i^2 \tag{3.57}$$

Condenser design procedure:

Finned-tube heat exchanger for condensing process in the condenser was considered. Total heat transfer area for thermo-economic investigation will be calculated and is necessary for this analysis. The total number of tubes is:

$$N_t = \frac{L_3}{P_t} \frac{\frac{L_2}{P_c} + 1}{2} + \left(\frac{L_3}{P_t} - 1\right) \frac{\frac{L_2}{P_c} - 1}{2} \tag{3.58}$$

Total heat transfer area is composed of the primary and fin surface area that are given by Eqs. (3.59) and (3.60).

$$A_p = \pi d_o (L_1 - \delta N_f L_1) N_t + 2 \left(L_2 L_3 - \frac{\pi d_o^2}{4}\right) N_t \tag{3.59}$$

$$A_f = \left(\frac{2\pi(d_e^2 - d_o^2)}{4} + \pi d_e \delta \right) N_f L_1 N_t \tag{3.60}$$

In which, L_1, L_2, L_3, P_t, P_c, δ, and N_f are length, across and height of circular fine tube heat exchanger, transverse tube pitches, longitudinal tube pitch, fin thickness, and number of fins per unit length respectively. The minimum free-flow area is

$$A_c = \frac{L_3}{P_t} \left[(P_t - d_o)L_1 - (d_e - d_o)\delta N_f L_1 \right] \tag{3.61}$$

The hydraulic diameter is given by Eq. (3.62).

$$D_h = 4A_c L_2 / A_t \tag{3.62}$$

The mass velocity G is given by:

$$G = \dot{m}/A_c \tag{3.63}$$

The Reynolds number is given by:

$$Re = \frac{\rho v D_h}{\mu} = \frac{G D_h}{\mu} \tag{3.64}$$

The pin pitch is defined by:

$$P_f = 1/N_f \tag{3.65}$$

Convection heat transfer coefficient of the air over the pipes on the condenser is given by Eq. (3.66) [42].

$$h_o = 0.14 Re^{-0.328} \cdot \left(\frac{P_t}{P_l} \right)^{-0.502} \cdot \left(\frac{S}{d_o} \right)^{0.0312} \cdot G \cdot cp \cdot Pr^{-\frac{2}{3}} \tag{3.66}$$

Condensing coefficient inside the pipe is given by Butterworth relation [42].

$$h_i = 0.728 \left[1 + \frac{(1-x)}{x} \left(\frac{\rho_v}{\rho_l} \right)^{\frac{2}{3}} \right]^{-\frac{3}{4}} \times \left[\frac{K_l^3 \rho_l (\rho_l - \rho_v) g h_{lv}'}{\mu_l d_i (T_{sat} - T_w)} \right]^{\frac{1}{4}} \tag{3.67}$$

And

$$h_{lv}' = h_{lv} + 0.68 C p_l (T_{sat} - T_w) \tag{3.68}$$

Finally, pressure drop is define by Eqs. (3.69) and (3.70) [43]:

$$\Delta P = \frac{G^2}{2\rho_i} \left[2 \left(\frac{\rho_i}{\rho_o} - 1 \right) + \frac{4fL}{D_h} \rho_i \left(\frac{1}{\rho} \right)_m \right] \tag{3.69}$$

$$\left(\frac{1}{\rho} \right)_m = \frac{1}{\rho_m} = \frac{1}{2} \left(\frac{1}{\rho_i} + \frac{1}{\rho_o} \right) \tag{3.70}$$

Algorithm for designing heat exchangers:

Procedure design of heat exchangers has been introduced by some references [42], [43], [131]. These algorithms for designing evaporator and MHX (Fig. 3.5 (a)) and condenser (Fig. 3.5 (b)) were proposed. At first, initial data that are considered for designing the heat exchangers are entered into the program. Thermodynamic properties for refrigerant and secondary fluid are calculated. Design parameters that sought by iterations initially are considered and then flow characteristics of the fluids are determined. After that, heat transfer characteristics are calculated. Achieved values of the parameters are checked with the standard values that are defined by aforementioned references. Also, the pressure

drop for refrigerant that is inside the tubes and secondary fluids that are water in evaporator and air in the condenser will be investigated.
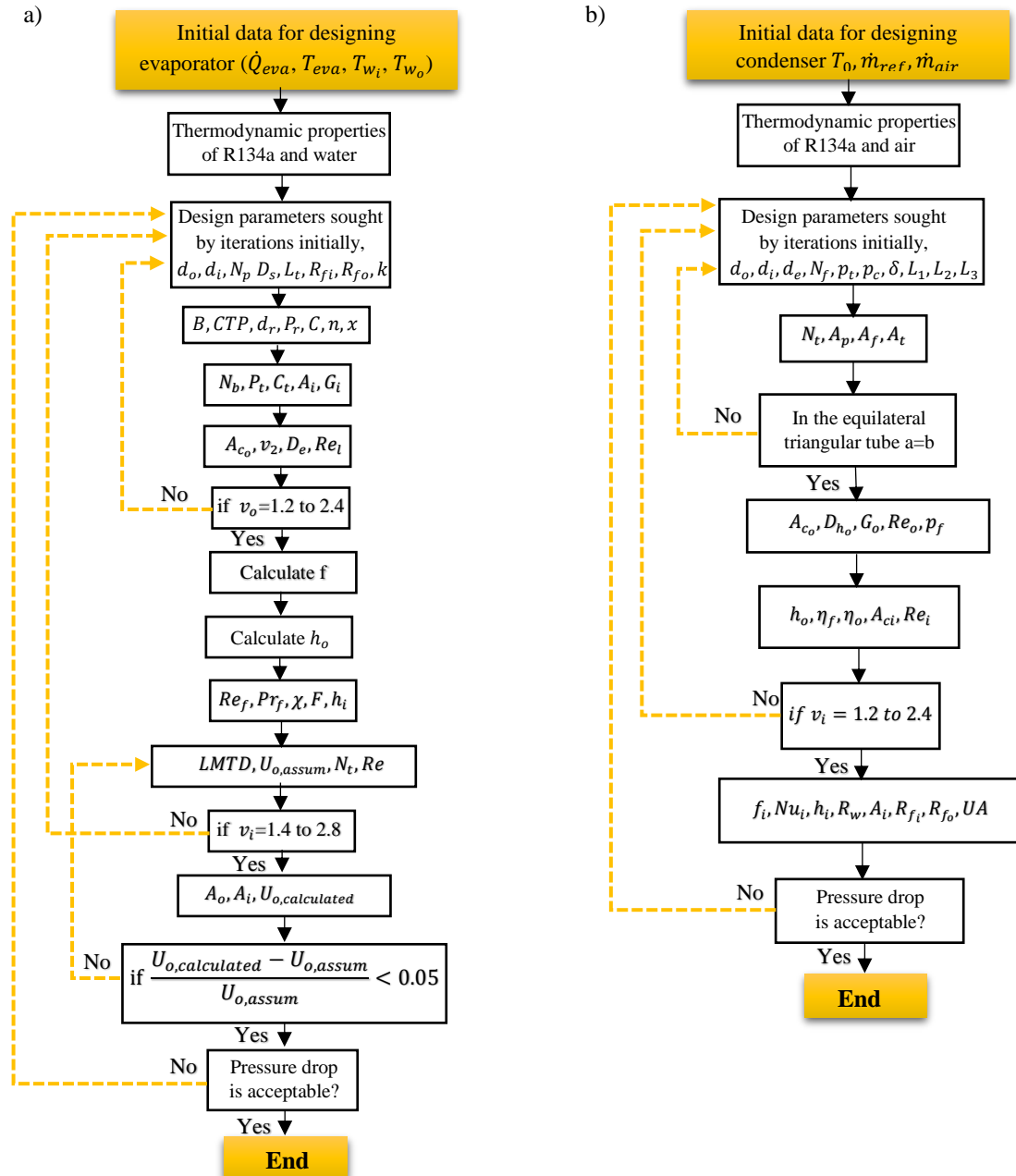
Fig. 3.5. Flowchart for designing of the evaporator (a) and condenser (b).

Fig. 3.6 demonstrates the tube surface area for a circular finned-tube heat exchanger and defines some geometrical characteristics of this heat exchanger. Also, Fig. 3.7 shows a cross-section of the square-pitch layout for shell and tube heat exchanger. The clearance and tube pitch for designing a heat exchanger is defined in this figure.
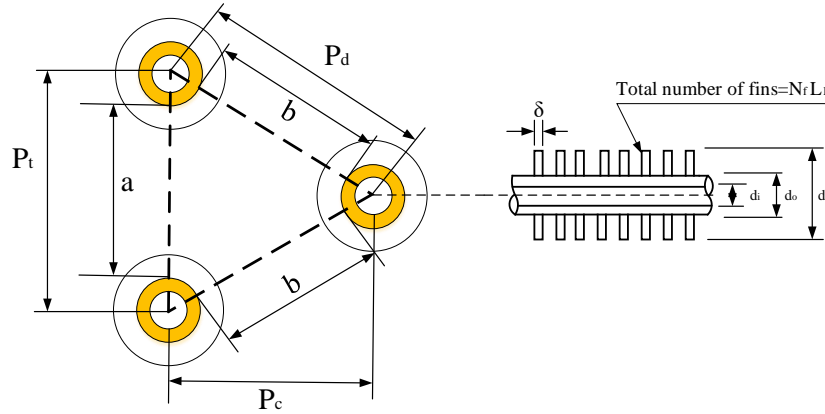
Fig. 3.6. The tube surface area.
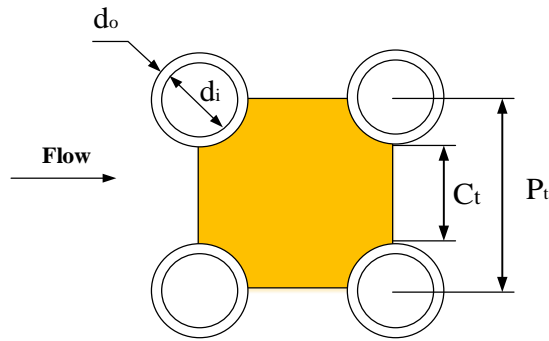
Fig. 3.7. Square-pitch layout.

3.1.1.2. Design ejector

Fig. 3.8 illustrates a schematic of the ejector device that was used for EERS. It is constituted by motive nozzle, suction nozzle, mixing section, and diffuser. Geometrical parameters that is shown in Fig. 3.8 will be determined in the result section of this study.
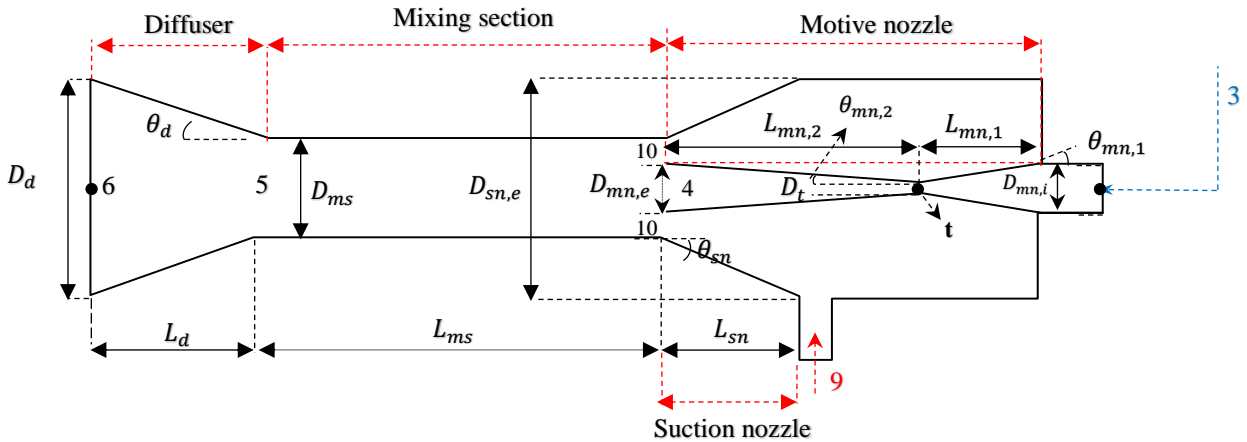
Fig. 3.8. Schematic of the ejector device.

Motive nozzle:

Sarkar et al. [132] illustrated that assumption of constant pressure for designing an ejector is better than the assumption of constant area. In the outlet of ejector motive nozzle with considered constant pressure:

$$p_4 = p_{eva} - \Delta p \tag{3.71}$$
$$h_{4,is} = h(p_4, s_3) \tag{3.72}$$
$$\eta_{mn} = \frac{h_3 - h_4}{h_3 - h_{4,is}} \tag{3.73}$$
$$v_4^2 = 2(h_3 - h_4) \tag{3.74}$$
$$A_4 \rho_4 v_4 = \frac{1}{(1+\omega)} \tag{3.75}$$
$$G_4 = \rho_4 v_4 \tag{3.76}$$
$$D_{mn,e} = \sqrt{\frac{4\dot{m}_3}{\pi G_4}} \tag{3.77}$$

Where $\omega = \dot{m}_9 / \dot{m}_3$ is ejector entrainment ratio.

Suction nozzle:

At the suction nozzle the governing equations for calculating the thermodynamic properties are:

$$p_{10} = p_{eva} - \Delta p \tag{3.78}$$
$$h_{10,is} = h(p_{10}, s_9) \tag{3.79}$$
$$\eta_{sn} = \frac{h_9 - h_{10}}{h_9 - h_{10,is}} \tag{3.80}$$
$$v_{10}^2 = 2(h_9 - h_{10}) \tag{3.81}$$
$$G_{10} = \rho_{10} v_{10} \tag{3.82}$$
$$A_{10} \rho_{10} v_{10} = \frac{\omega}{(1+\omega)} \tag{3.83}$$
$$D_{sn,e} = \sqrt{\frac{4\dot{m}_9}{\pi G_{10}}} \tag{3.84}$$

Mixing section:

And in the mixing section which is point 5 in the Fig. 3.8:

$$p_4 = p_5 = p_{10} \tag{3.85}$$
$$v_5 = \eta_{ms}^{1/2} \left(\frac{1}{1+\omega} v_4 + \frac{\omega}{1+\omega} v_{10} \right) \tag{3.86}$$
$$h_5 + \frac{v_5^2}{2} = \frac{1}{1+\omega} \left(h_4 + \frac{v_4^2}{2} \right) + \frac{\omega}{1+\omega} \left(h_{10} + \frac{v_{10}^2}{2} \right) \tag{3.87}$$
$$s_5 = s(p_5, h_5) \tag{3.88}$$
$$G_5 = \rho_5 u_5 \tag{3.89}$$
$$D_{ms} = \sqrt{\frac{4\dot{m}_{tot}}{\pi G_5}} \tag{3.90}$$

Diffuser:

At the diffuser outlet:

$$h_6 = h_5 + \frac{v_5^2}{2} \tag{3.91}$$

$$\eta_d = \frac{h_5 - h_{6,is}}{h_5 - h_6} \tag{3.92}$$

$$p_6 = p(h_{6,s}, s_5) \tag{3.93}$$

After finding properties in point 6 of the cycle, the amount of the quality at this point with Eq. (3.94) should be satisfied.

$$x_6 = \frac{1}{1 + \omega} \tag{3.94}$$

Proposed algorithm for ejector:

Computational procedure flowchart for EERS is shown in Fig. 3.9. At first, design parameters for the system are entered into the algorithm and then thermodynamic properties of refrigerants and water are calculated. By applying energy equation for evaporator and condenser, operating conditions for these two components will be obtained. After that, ejector entrainment ratio and pressure drop in suction nozzle are guessed and then the operating conditions for motive nozzle, suction nozzle, mixing section, and diffuser respectively are obtained. The quality of vapor in the outlet of diffuser should be satisfied with Eq. 3.94, otherwise, the value of ΔP and ω will be updated.
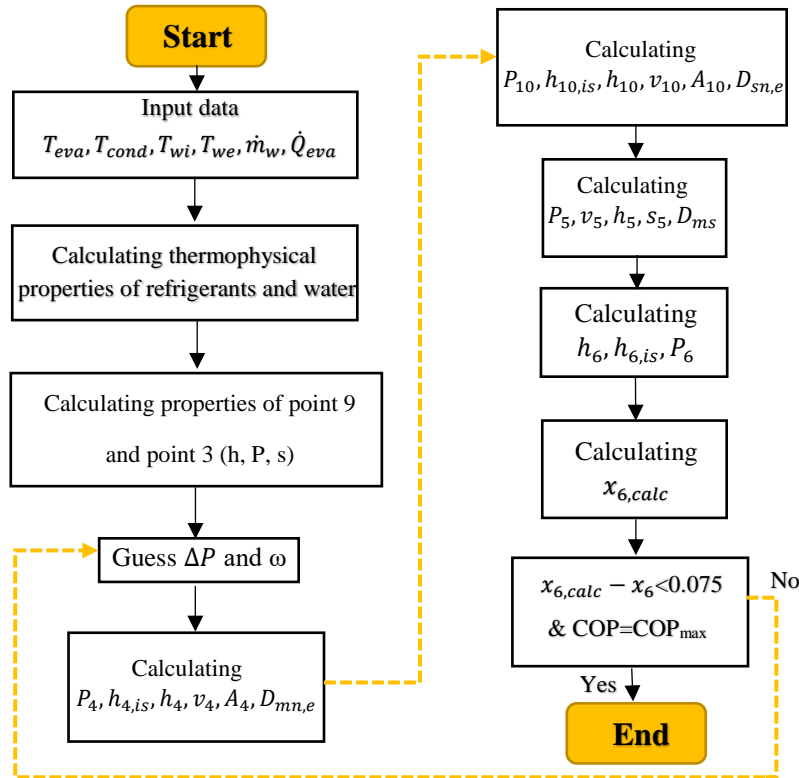
Fig. 3.9. Algorithm computer program for design EERS.

3.1.2. Thermo-economic analysis

Purchased equipment cost:

In this analysis by applying the economic conception besides the thermodynamic definitions and with the definition of economic value for energy and exergy conceptions, will have a balance between the energy and exergy next to the costs of the system. The balance of the costs in the steady state for all the systems was stated by the Eq. (3.95).

$$C_{P,tot} = C_{F,tot} + Z_{tot}^{CI} + Z_{tot}^{OMC} \tag{3.95}$$

Eq. 3.95 states which the rate of product cost of the system ($C_{P,tot}$) is equal to the rate of the fuel cost ($C_{F,tot}$), the rate of overall investment costs (Z_{tot}^{CI}), and costs related to maintenance and operation (Z_{tot}^{OMC}). The purchased equipment cost (PEC) are given by the following equations [133]:

For compressor:

$$PEC_{com} = \left(\frac{573\dot{m}_{ref}}{0.8996 - \eta_{isen}}\right)\left(\frac{P_{cond}}{P_{eva}}\right)ln\left(\frac{P_{cond}}{P_{eva}}\right) \tag{3.96}$$

$$\eta_{isen} = 0.85 - 0.046667\left(\frac{P_{cond}}{P_{eva}}\right) \text{ [129]} \tag{3.97}$$

PEC for the heat exchanger is obtained by the Eq. (3.98) [133].

$$PEC_{HEX} = 2290(A_{HEX})^{0.6} \tag{3.98}$$

And for Condenser and evaporator, PEC are given by Eqs. (3.99) and (3.100) [134].

$$PEC_{cond} = 516.6213A_{cond} + 268.45 \tag{3.99}$$

$$PEC_{eva} = 309.143A_{eva} + 231.915 \tag{3.100}$$

PEC for ejector expansion device is given by El-Sayed [135].

$$PEC_{eje} = 750\dot{m}_f\left(\frac{T_i}{P_i}\right)^{0.05} P_e^{-0.75} \tag{3.101}$$

It should be mentioned that these costs are for the 2004 year and must be updated. The costs will be updated to new costs.

$$PEC_{new} = PEC_{ref}\left(\frac{I_{new}}{I_{ref}}\right) \tag{3.102}$$

I_{new} and I_{ref} are Marshal and Swift index [136].

Total Revenue Requirement (TRR) and economic objective function:

For the analysis and optimization of the energy systems, total annual investment, fuel cost and cost of maintenance and operation must be calculated. In this section TRR method has been applied [137]. Also, the complete analysis of this method has been shown in Ref. [138]. The total PEC is defined by the Eq. (3.103).

$$PEC_{tot} = PEC_{com} + PEC_{cond} + PEC_{eva} + PEC_{H.E} \tag{3.103}$$

Total net investment (TNI) is defined by Eq. (3.104) [138].

$$TNI = PEC_{tot} + piping \ and \ installation \ costs \tag{3.104}$$

27

Piping and installation Cost is 5 percent of PEC_{tot} and TNI is given by the following equation:

$$TNI = 1.05\, PEC_{tot} \tag{3.105}$$

It is assumed that the cost of equipment at the end of the life operation is zero and with this assumption total capital recovery is:

$$TCR_j = BD_j, \qquad j = 1,2,\dots,BL \tag{3.106}$$

In which

$$BD_j = \frac{TNI}{BL} \qquad j = 1,2,\dots,BL \tag{3.107}$$

Where BD_j, BL, and TCR_j are book depreciation, book life that is 25 years in this study and total capital recovery.

Balance at the beginning of a year is equal to the total net investment and it is in order to calculate the total revenue requirement.

$$BBY_1 = TNI \tag{3.108}$$

The cost balance at the beginning of every year is obtained from Eq. (3.109).

$$BBY_j = BBY_{j-1} - BD_j \tag{3.109}$$

Return on investment (ROI) of the system is given by the following equation:

$$ROI_j = BBY_j \times i_{eff}, \qquad j = 1,2,\dots,BL \tag{3.110}$$

The fuel cost of the system for the first year is calculated by Eq. (3.111). In unit 132 of the refinery, there are two systems for working and this analysis is for one of them. Thus the time of system operating is $\tau = 4380\ h$.

$$FC_0 = C_{elect}.\tau.\dot{w}_{tot} \tag{3.111}$$

Where C_{elect} and $\dot{w}_{tot}$ are the constant cost of electricity consumption (\$/kWh) and total energy electricity consumption respectively.

The fuel cost in j year is:

$$FC_j = FC_0(1 + r_{FC})^j \tag{3.112}$$

Where r_{FC} is the rate of increasing fuel cost that considered 0.156 according to the 2016 year in Iran [139].
Operating and maintenance cost (OMC) for the first year considered 2 percent of the total PEC and is stated by Eq. (3.113). Also, OMC for j year is obtained by Eq. (3.114).

$$OMC_0 = 0.02 PEC_{tot} \tag{3.113}$$
$$OMC_j = OMC_0(1 + r_{OMC})^j \tag{3.114}$$

Total revenue requirement in the j year from aggregate the return on investment, fuel cost and operating and maintenance costs is obtained.

$$TRR_j = ROI_j + FC_j + OMC_j \tag{3.115}$$

The total revenue requirement is increasing in various years with increase operation years. Therefore it is seen a need to levelized of this cost. The levelized total revenue requirement is defined by the following equation:

$$TRR_L = CRF \times \sum_{j=1}^{BL} \frac{TRR_j}{\left(1 + i_{eff}\right)^j} \tag{3.116}$$

In which, i_{eff} is the annual effective rate of return that is calculated 0.2 in Iran. Also, CRF is capital recovery factor that is given by Eq. (3.117).

$$CRF = \frac{i_{eff}\left(1 + i_{eff}\right)^{BL}}{\left(1 + i_{eff}\right)^{BL} - 1} \tag{3.117}$$

The cost of the fuel is increasing too. The levelized fuel cost is obtained by multiple of the fuel cost in the first year in CELF.

$$FC_L = FC_0. CELF = FC_0 \times \frac{K_{FC}(1 - K_{FC}^n)}{(1 - K_{FC})} \times CRF \tag{3.118}$$

$$K_{FC} = \frac{1 + r_{FC}}{1 + i_{eff}} \tag{3.119}$$

The operating and maintenance costs obtained by this method and by the beginning of the year for levelized annual.

$$OMC_L = OMC_0 \times CELF = OMC_0 \frac{K_{OMC}(1 - K_{OMC}^n)}{(1 - K_{OMC})} \times CRF \tag{3.120}$$

$$K_{OMC} = \frac{1 + r_{OMC}}{1 + i_{eff}} \tag{3.121}$$

Finally the levelized annual cost is

$$CC_L = TRR_L - FC_L - OMC_L \tag{3.122}$$

The cost of expenses or cost of investment (superscript Cl) and operating and maintenance costs (superscript OM) can be divided into k part similar to purchased equipment cost.

$$\dot{Z}_k^{cl} = \frac{CC_L}{\tau} \frac{PEC_k}{\sum_k PEC_k} \tag{3.123}$$

$$\dot{Z}_k^{OM} = \frac{OMC_L}{\tau} \frac{PEC_K}{\sum_k PEC_k} \tag{3.124}$$

The rate of total cost of part k for the system is obtained by Eq. (3.125).

$$\dot{Z}_K = \dot{Z}_K^{CI} + \dot{Z}_K^{OM} \tag{3.125}$$

The cost of annual fuel obtained as dollar per hour by dividing the levelized annual cost of fuel per hours of operation.

$$\dot{C}_F = \frac{FC_L}{\tau} \tag{3.126}$$

Finally, the target function is total cost based on dollar per hour.

$$\dot{C}_P = \dot{C}_F + \sum \dot{Z}_K \tag{3.127}$$

3.1.3. Environmental Analysis

The refrigeration system in the refinery does not have any fuel combustion, therefore no environmental pollutant is emitted directly by the system. But the cycle works with electrical energy in the compressor and condenser fan and this electrical energy is produced by a fossil fuel power plant. The power plant for this electrical energy releases pollutant to the surrounding, which can be calculated. These contaminations are considered as a function of produced electrical energy for compressor and condenser fan, which are calculated by Eqs. (3.128)- (3.130). Table 3.4 illustrates the value of different contaminations that are released by the power plants based on gr/kWh in Iran. This table is for the 2013 year that is the last data of it [140]. According to Table 3.4, for this application, carbon monoxide (CO), carbon dioxide (CO_2) and oxide of nitrogen (NO_x) are considered as environmental pollutant, which can be calculated by the following relations [79], [141].

$$m_{CO_2} = \tau \times \left(\dot{W}_{com} + \dot{W}_{fan} \right) \times fac_{CO_2} \tag{3.128}$$

$$m_{NO_x} = \tau \times \left(\dot{W}_{com} + \dot{W}_{fan} \right) \times fac_{NO_x} \tag{3.129}$$

$$m_{CO} = \tau \times \left(\dot{W}_{com} + \dot{W}_{fan} \right) \times fac_{CO} \tag{3.130}$$

Where fac_{CO_2}, fac_{NO_x}, fac_{CO} and τ are the produced coefficient of CO_2, NO_x, CO and working time of the system per year and are equal to 694.906 gr/kWh, 2.548 gr/kWh, 0.695 gr/kWh and 4380 h, respectively [140]. It should be noted that there are two refrigeration systems in the refinery in parallel and one of them is analyzed.

Table 3.4. The amount of the pollution (gr/kWh) that is released by various power stations in Iran [140].

Type of power plant	NO_x	SO_2	SO_3	CO	SMP	CO_2	CH_4	N_2O	C
Ministry of power									
Vapor	2.307	7.752	0.033	2.530	0.169	824.899	0.022	0.004	224.972
Gas	2.403	0.505	0.013	0.091	0.124	849.370	0.017	0.002	231.646
Combined cycle	2.925	0.282	0.009	0.086	0.081	469.945	0.011	0.002	128.167
Diesel	1.525	4.605	0.070	0.001	0.292	826.379	0.036	0.012	225.376
Private sector									
Vapor	1.890	3.612	0.021	0.508	0.135	764.902	0.019	0.003	208.610
Gas	2.269	0.824	0.018	0.069	0.135	798.463	0.018	0.003	217.763
Combined cycle	3.077	0.292	0.010	0.053	0.086	483.882	0.012	0.002	131.968
Grate industries	2.283	0.029	0.001	0.465	0.069	1182.665	0.014	0.001	322.545
Total average	2.548	2.455	0.018	0.695	0.122	694.906	0.017	0.003	189.520

3.2. Machine learning algorithms

A machine learning algorithm in its most general form can be described as a function *f(x)* which takes an input vector x and generates an output vector y. Fig. 3.10 illustrates a classification of machine learning that contains two types of techniques (supervised learning and unsupervised learning). Supervised learning divided into two sections that are

classification and regression that these two methods were applied to predict the target. Also unsupervised learning uses clustering technique to forecast the target [142].
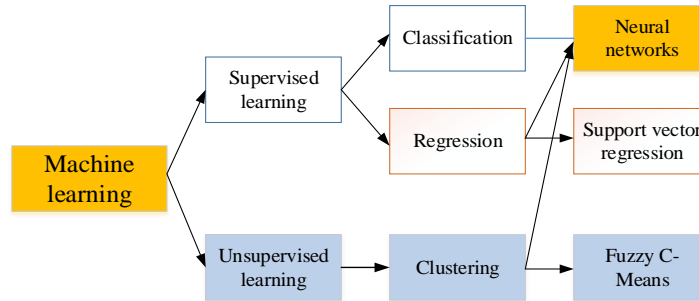
Fig. 3.10. Classification of the machine learning.

3.2.1. Artificial neural network (ANN)

An artificial neural network (ANN) is a network that attempts to imitate brain functions. The human brain contains approximately 10^{11} neurons working in perfect harmony to perform a task. ANN's are designed to do a specific task through a learning process. By providing inputs and the desired output data, an ANN finds the relationship between the input and output data. Similar to a brain, where neurons are connected by synapses, the neurons in an ANN are connected by weighted inputs. Neurons are activated when the summation of these weighted inputs exceeds the neurons activation threshold. There are seven successive steps involved in the design and implementation of an ANN:

1. Collecting data
2. Creating the network
3. Configuring the network
4. Initializing the weights and biases
5. Training the network
6. Validating the network
7. Using the network

ANN structure:

An ANN consists of three sections that are input layer, hidden layer, and the output layer. Input vector (X) is multiplied by weight vector (W) and this multiplication vector (WX) is added to a bias (b) that led to the input vector (n) that this vector enters to a neuron. The neuron applies a transfer function (*f*) to this input vector that the output vector (a) is obtained. Fig. 3.11 shows a single neuron network that explained in this section. Eq. (3.131) shows the relation between input and the output,

$$n = W_{1,1}X_1 + W_{1,2}X_2 + \cdots + W_{1,r}X_r + b \tag{3.131}$$

Also, Eqs. 3.132 and 3.133 demonstrate that during the training stage the amount of the weight(s) and bias(s) will be updated with this equation.

$$W(k + 1) = W(k) + 2\alpha e(k)X^T(k) \tag{3.132}$$

31

$$b(k + 1) = b(k) + 2\alpha e(k) \tag{3.133}$$

In which, α and e are the learning rate and error respectively.
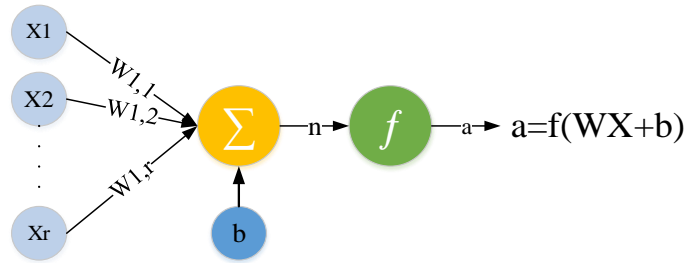
Fig. 3.11. Single neuron network.

Single layer neural network:

Single-layer neural network (SLNN) is an extended case of the simple case mentioned in the previous section. SLNN consists of one layer of neurons as shown in Fig. 3.12.
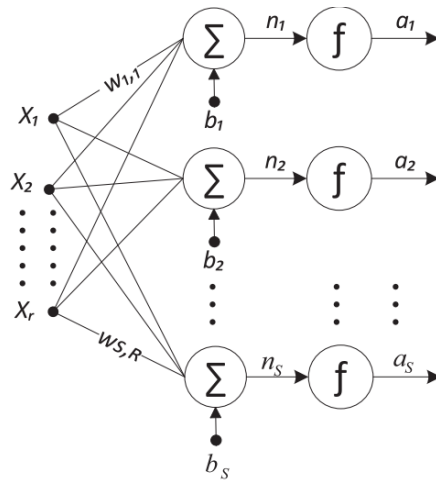
Fig. 3.12. Single Layer Neural Network.

Each input of the SLNN, x_i, is connected to all of the neurons in the layer by a weight vector, W. Every neuron adds its weight inputs $(W^T x)$ and bias to form its net input, n_i. The net input vector n_i is used by the activation function, f, to form the neuron output vector a_i. The number of inputs is typically different than the number of neurons. The weight matrix, W, is given by:

$$\begin{bmatrix} W1,1 & W1,2 & \cdots & W1,R \\ W2,1 & W2,2 & \cdots & W2,R \\ \cdots & \cdots & \cdots & \cdots \\ WS,1 & WS,2 & \cdots & WS,R \end{bmatrix} \tag{3.134}$$

Where R is the number of elements in the input vector and S is the number of neurons

Multilayer neural network:

Multi-layer neural networks (MLNN's) are used to implement complex problems that SLNN's are unable to solve. It has the ability to convert non-linearly-separable objects into a different domain where they become linearly separable. MLNN's include an input layer, output layer, and hidden layers as shown in Fig. 3.13.
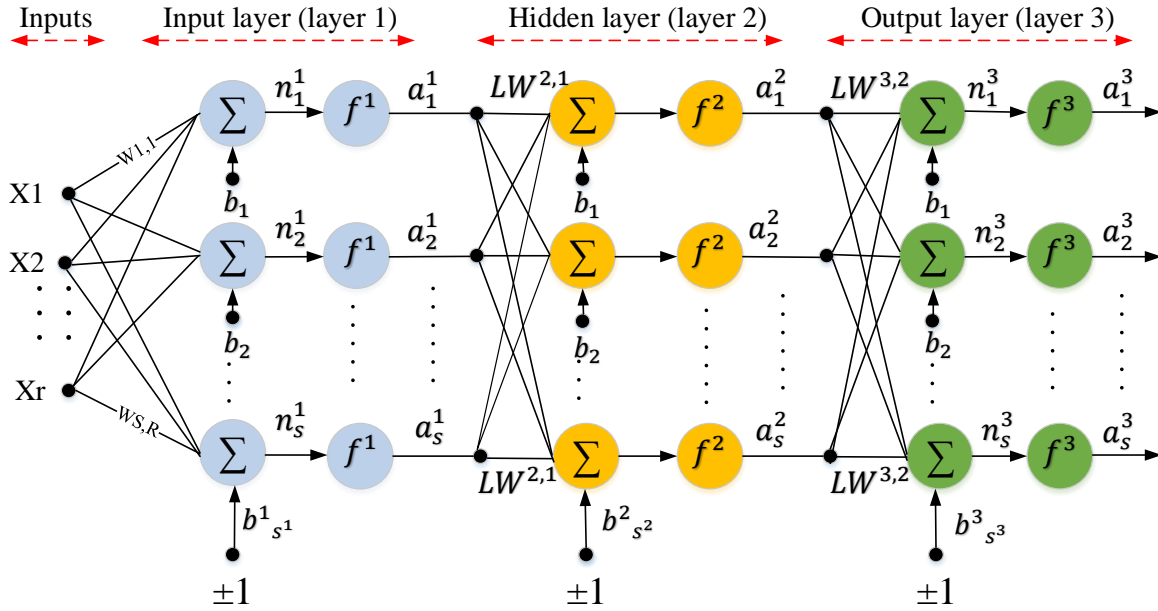
Fig. 3.13. Multilayer neural network.

In multi-layer networks the output of each layer becomes the input for the subsequent layer. Each layer has its own weight matrix. These weight matrices are varied to achieve a minimum total error. The output of a MLNN is given by:

$$a^1 = f^1(IW^{1,1}X + b^1)$$ (3.135)
$$a^2 = f^2(IW^{2,1}a^1 + b^2)$$ (3.136)
$$a^3 = f^3(IW^{3,2}a^2 + b^3)$$ (3.137)
$$a^3 = f^3(IW^{3,2}f^2(IW^{1,2}f^1(IW^{1,1}X + b^1) + b^2) + b^3)$$ (3.138)

Where, X= input vector, IW=input weight matrix, LW = hidden weight matrix, b = bias vector, and a = layer output vector. The hidden layer associated with multi-layer neural networks provides a powerful tool for performing very complex analysis.

3.2.2. RBFNN model

Radial Basis Function (RBF) neural networks operate on a somewhat different principle. Instead of having threshold units with a single value against which to compare accumulated sums of input signals, each RBF neuron has a set of values called a "reference vector" for comparison with an input set of the same cardinality. Fig. 3.14 illustrates a RBFNN that contains three layers [143]. The first layer is the input layer that contains the input neurons; the second layer is the hidden layer that is composed the RBF neurons; the third layer is the output layer contains linear basis function neurons with one node per category or class of data. The weight c and one extra coefficient for each neuron were defined by the RBF neuron (for the radial basis neuron is not the bias but the width b). The weights of the RBF

neuron determine the center for the RBF and actually it calculates the Euclidean distance between the input vector and the middle of the hypersphere. The neuron's inner potential can be obtained by:

$$g(x) = \frac{\|x - c\|}{b} \tag{3.139}$$

And the combining with the Gaussian activation function can be obtained:

$$f(x) = e^{-\frac{\|x-c\|}{b}} \tag{3.140}$$

Also, the final activation of the ith output neuron is obtained by the following equation:

$$y_i = W_{o,j} + \sum_{i=1}^{n_h} W_{i,j} \, e^{-\frac{\|x-c_i\|}{b_i}} \tag{3.141}$$

The RBFNN will be designed with the "*newrb*" function in Matlab software. The network will be trained with the 70% of the data and 30% of data will be used to test the network. The optimum performance of the network will be obtained with setting the various parameters of the network. For this network the spread of RBF and maximum number of neurons are the important user defined parameters.
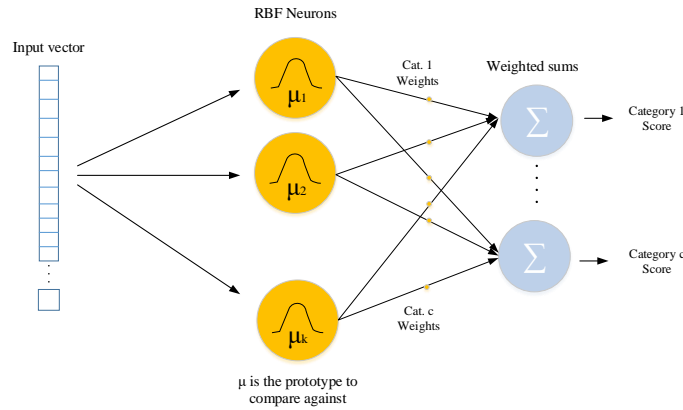
Fig. 3.14. Structure of the RBF.

3.2.3. SVR model

Support Vector Machines that have been introduced by Vapnik (2013) [74] are classification and regression techniques, which optimize its structure based on the input data. For training data $(x_i, y_i), ..., (x_n, y_n)$, where x_i are the vectors with input values and y_i the appropriate output values for x_i, the ε-insensitive SVR aims to find a function $f(x)$, that has the deviation from the target y_i at most ε at all times, while being as "flat" as possible. This problem can be written down as an optimization problem:

$$\min_{\omega,b,\xi,\xi^*} \frac{1}{2} \omega^T \omega + C \sum_{i=1}^{n} (\xi_i + \xi_i^*) \tag{3.142}$$

$$s.t. \begin{cases} y_i - (\langle \omega, x_i \rangle + b) \leq \varepsilon + \xi_i \\ (\langle \omega, x_i \rangle + b) - y_i \leq \varepsilon + \xi_i^* \\ \xi, \xi^* \geq 0 \end{cases} \tag{3.143}$$

In which, n is the number of samples, ξ_i shows the upper training error, ξ_i^* is the lower training error subject to the ε-insensitive tube $|y_i - (\langle \omega, x_i \rangle + b)|$. Also, C is the regularized constant that determines the trade-off between the

regularization term and the empirical error, and $C > 0$. The SVR creates the $f(x)$ such that: (1) ξ_i and ξ_i^* are minimized to achieve the minimal training error and (2) to make the function "flat" and penalize too complex functions we minimize $\frac{1}{2}\omega^T\omega$. The final decision function is defined by:

$$f(x, \alpha_i, \alpha_i^*) = \sum_{i=1}^{n}(\alpha_i - \alpha_i^*)\kappa(x, x_i) + b \tag{3.144}$$

And can be found by utilizing the properties Lagrange multipliers, Kernel trick and the optimality constraints. The Lagrange multipliers and Kernel trick are described in the following.

Lagrange multipliers:

In Eq. (3.144) α_i, α_i^* indicate the Lagrange multipliers. They can be obtained by maximizing the dual function of Eq. (3.142) and then can be introduced by:

$$\max_{\alpha_i, \alpha_i^*} \sum_{i=1}^{n} y_i(\alpha_i - \alpha_i^*) - \varepsilon \sum_{i=1}^{n} y_i(\alpha_i - \alpha_i^*) - \frac{1}{2}\sum_{i=1}^{n}\sum_{j=1}^{n}(\alpha_i - \alpha_i^*)(\alpha_j - \alpha_j^*)\langle x_i, x_j\rangle \tag{3.145}$$

$$s.t. \begin{cases} \sum_{i=1}^{n}(\alpha_i - \alpha_i^*) = 0 \\ 0 \leq \alpha_i \leq C \\ 0 \leq \alpha_i^* \leq C \\ i = 1,2, \ldots, n \end{cases} \tag{3.146}$$

In Eq. (3.142), only some $(\alpha_i - \alpha_i^*)$ are not equal to zero, which comes from the Karush-Kuhn-Tucker's conditions of solving a quadratic programming problem. The support vector itself refers to the approximation error of data point on non-zero coefficient equal or larger than ε. Because errors lower than ε are acceptable, the data from the training set inside the "ε-tube" do not contribute to the cost nor the solution of the problem.

Kernel trick:

The key to non-linear extension of the SVR is the Eq. (3.145) and the existence of the so-called kernel trick. The dot product of $\langle x_i, x_j\rangle$ from the Eq. (3.145) becomes a kernel function $\langle \emptyset(x_i), \emptyset(x_j)\rangle = k(x_i, x_j)$ in the case of non-linearity. The function $\emptyset: R^d \rightarrow \mathcal{H}$ presents the idea of mapping the input space into a feature space with a higher dimension. The common kernel function that satisfy this issue are:

Linear kernel: $k_{lin}(x, x') = \langle x, x'\rangle$ \hfill (3.147)

Polynomial kernel: $\langle x, x'\rangle^p$, $p \in N$ \hfill (3.148)

Radial basis function (RBF): $K(x, x') = exp(-\sigma\|x - x'\|^2)$, $\sigma \in R, \sigma > 0$ \hfill (3.149)

For this study RBF was used as kernel function that its mapping space has an infinite number of dimensions. Fig. 3.15 shows a SVRNN architecture based on Eq. (3.144) with considering the Karush-Kuhn-Tucker's conditions for solving a quadratic programming problem. The value of $(\alpha_i - \alpha_i^*)$ that are nonzero are support vectors, which are applied to obtain the decision function. It is important to find the optimum three user-determined parameters that are C, ε, and σ.

$$f(x) = \sum (\alpha_i - \alpha_i^*)\, k(x, x_i) + b$$

				Output
$\alpha_1 - \alpha_1^*$	$\alpha_2 - \alpha_2^*$		$\alpha_i - \alpha_i^*$	Weights
$k(x, x_1)$	$k(x, x_2)$	$\cdots$	$k(x, x_i)$	Dot product
$\emptyset(x_1)$	$\emptyset(x_2)$	$\emptyset(x)$ $\cdots$	$\emptyset(x_i)$	Mapped vectors
x_1	x_2	$\cdots$	x_i	Support vectors
		x		Test vector x
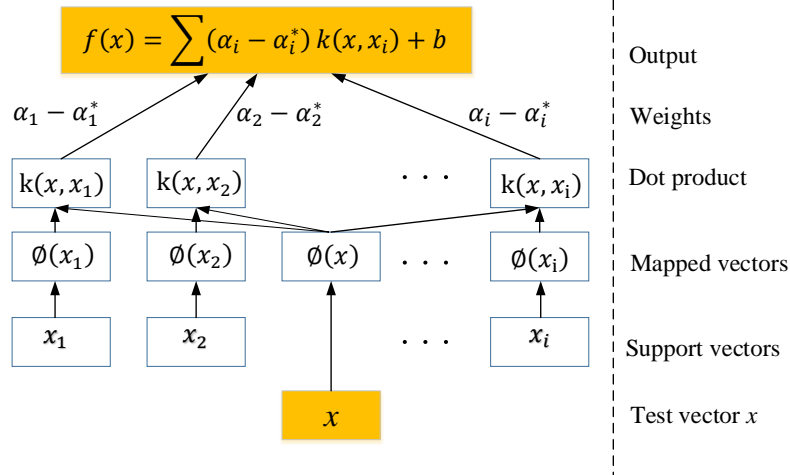
Fig. 3.15. SVR architecture.

3.2.4. FIS model

Fuzzy inference system (FIS) is represented as the process of mapping a set of input data sets into a set output data, using an approach based on fuzzy logic (an architecture of FIS is shown in Fig. 3.16). The process contains the following main parts: membership functions (MFs), fuzzy logic operators, and if-then rules. The main steps of a FIS are: the first part is called fuzzification that is defined as: compare the input(s) with the MFs on the previous part to obtain the membership values; the second part is defined as: combine the membership values on the premise part to get firing strength (degree of fulfillment) of each rule; the third part: generate the qualified consequents or each rule depending on the firing strength; and the forth part is called the defuzzification and aggregate the qualified consequents to produce a crisp output [144].
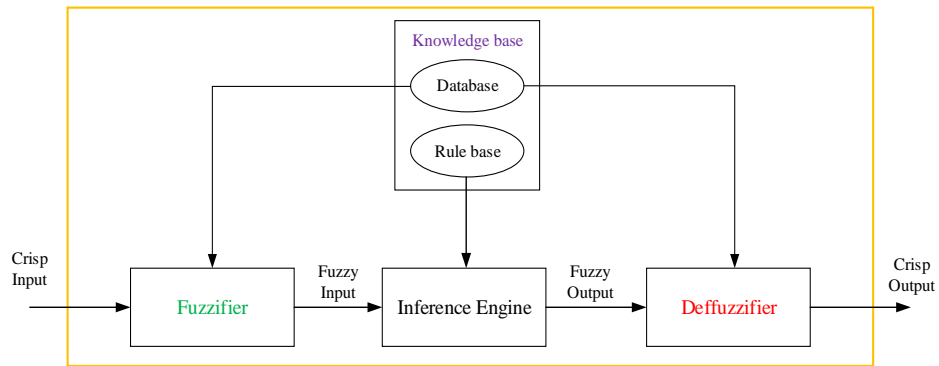
Fig. 3.16. The architecture of fuzzy inference system.

The knowledge base is defined as the jointly of the rule base (contains a fuzzy if-then rules) and the database (defines the membership functions of fuzzy sets used in the fuzzy rules). The fuzzifier by using the membership function converts the crisp input to a linguistic variable. Inference engine using if-then type fuzzy rules converts fuzzy input to the fuzzy output. Difuzzifier converts the fuzzy output of the inference engine to crisp using membership functions analogous to the ones used by the Defuzzifier. Two methods have been introduced for the FIS that are Mamdani (is the most commonly seen FIS method) and Sugeno or Takagi–Sugeno–Kang. This two type of FIS are different in the consequent of fuzzy rules. Fig. 3.17 shows the FIS structure that is proposed to predict the solar radiation in this study.

36

One model with the five inputs, and one output; also Mamdani method is selected for FIS structure. Also, IF-THEN rules, fuzzy maping, and membership function are describe in the following.
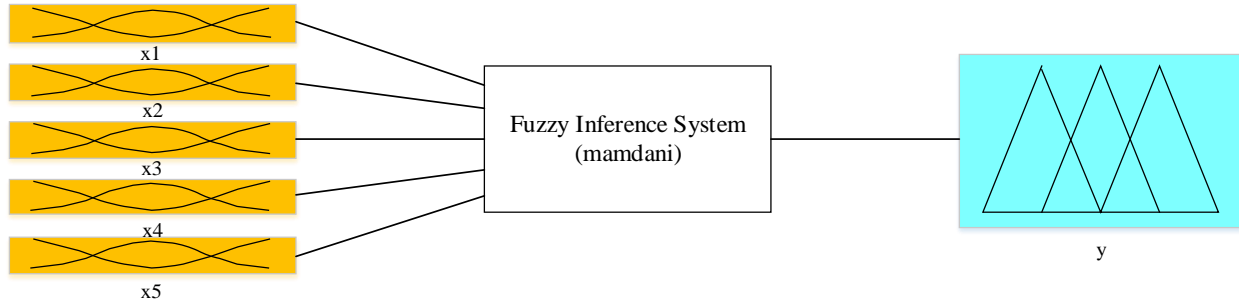
Fig. 3.17. FIS structure.

3.2.5. ANFIS model

Fuzzy rules will be obtained from the human expert in the most fuzzy systems, hence ANN were incorporated into fuzzy system to obtain the knowledge of human expert by applying the learning algorithms. This method was used for automatic fuzzy if-then rules generation. This connection (an ANN into fuzzy system) is called neuro-fuzzy system. The most frequently used ANN in neuro-fuzzy system is RBFNN in which each node has radial basis function such as Gaussian and Ellipsoidal. There are many developed neuro-fuzzy algorithms that adaptive neuro inference system is one of them. This algorithm uses RBFNN to determine the parameters of the fuzzy system. In this model Takagi–Sugeno–Kang models are involved in framework of adaptive system. For each ANFIS two basic learning algorithm are required that one of them is applied to find the suitable fuzzy logic rules and is called structure learning algorithm. The second one is the parameter learning algorithm to adjust the membership functions and other parameters according to desired performance from the system. In this study to obtain the fuzzy logic parameters, gradient-descent training algorithms are used. Fig. 3.18 shows the ANFIS structure that has been used from two fuzzy if-then rules under Takagi–Sugeno–Kang model that are given by the following:

Rule 1: If (x is A_1) and (y is B_1) then $f_1 = p_1 x + q_1 y + r_1$ (3.150)

Rule 2: If (x is A_2) and (y is B_2) then $f_2 = p_2 x + q_2 y + r_2$ (3.151)

In which r_i, p_i, and q_i are the design parameters that will be obtained during the period of training phase.

The ANFIS layers are described as follows:

Layer 1 (fuzzification layer), the signal that is obtained from each node is transferred to the other layer. Cells outputs (O_i^1) are defined by [145]:

$$O_i^1 = \mu_{A_i}(x), \quad i = 1,2$$ (3.152)

Where μ_{A_i} is associated to the membership function and A_i is linguistic variable associated with this node function.

In the most ANFIS models μ_{A_i} is selected as:

$$\mu_{A_i}(x) = exp\left\{-\left[\left(\frac{x - c_i}{a_i}\right)^2\right]^{b_i}\right\}$$ (3.153)

37

In which x is the input and $\{a_i, b_i, c_i\}$ are premise parameters.

Layer 2 (rule layer), is achieved with the membership degrees in which each node output demonstrates the firing strength of a fuzzy rule.

$$O_2^i = w_i = \mu_{A_i}(x).\mu_{B_i}(y), \quad i = 1,2 \tag{3.154}$$

Layer 3 (normalization layer), every node in this layer is a fixed node labeled N. The ith node calculates the ratio of the rule's firing strength to the sum of all rules' firing strengths:

$$O_3^i = \overline{w}_i = \frac{w_i}{w_1 + w_2}, \quad i = 1,2 \tag{3.155}$$

Layer 4 (defuzzification layer), the output value for each rule is calculated from the value of the previous layer.

$$O_4^i = \overline{w}_i f_i = \overline{w}_i(p_i x + q_i y + r_i), \quad i = 1,2 \tag{3.156}$$

In which $\overline{w}_i$ is a normalized firing strength from layer 3 and $\{p_i, q_i, r_i\}$ are the consequent parameters.

Layer 5 (sum layer), the output of ANFIS model is achieved by collecting the output values of each rule that are obtained from the previous layer.

$$O_5^i = overall\ output = \sum_i \overline{w}_i f_i = \frac{\sum_i w_i f_i}{\sum_i w_i}, \quad i = 1,2 \tag{3.157}$$

Three types of ANFIS are proposed to predict the time series data of solar radiation. The first one generate FIS structure from data using grid partition (this method generate one output Sugeno-type FIS using a grid partition on the data) (ANFIS-GP). The second one generate FIS structure using subtractive clustering (this method use subtractive clustering to create a Sugeno-type FIS structure and requires separate sets of input and output data as input arguments) (ANFIS-SC). The third one generate FIS structure using FCM clustering (this method by using fuzzy c-means (FCM) clustering generate a FIS) (ANFIS-FCM).
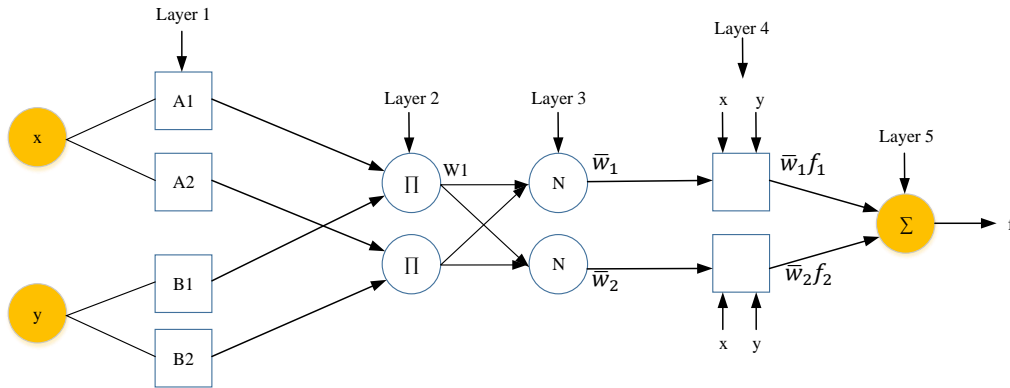
Fig. 3.18. ANFIS structure.

3.2.6. Particle Swarm Optimization (PSO) algorithm

Eberhart and Kennedy for the first time in 1995 developed particle swarm optimization (PSO) algorithm that inspired by the flocking and schooling patterns of fish and birds [146]. Swarm intelligence is defined as a problem-solving method that relies on interactions of simple processing units. This method uses a number of particles that constitute a swarm moving around in the search space looking for the best solution. Also, each particle in search space adjusts its

"flying" according to its own flying experience as well as the flying experience of other particles. Fig. 3.19 illustrate a design structure of PSO algorithm.
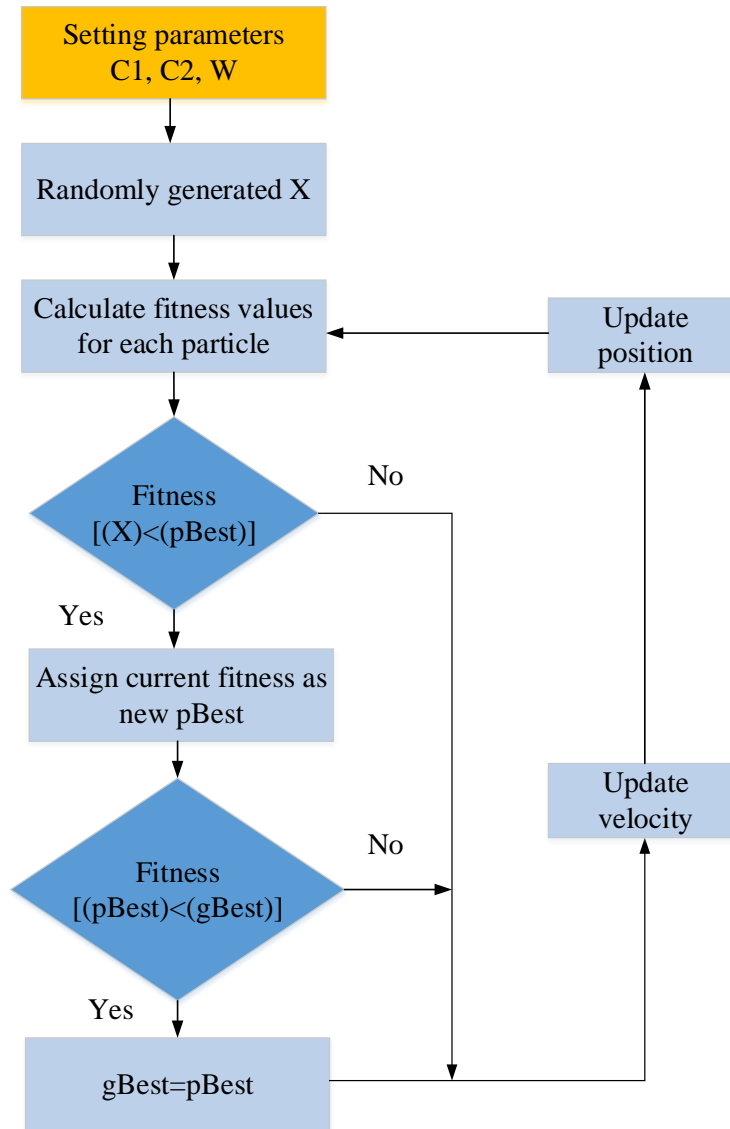
Fig. 3.19. Design structure of the PSO algorithm.

The algorithm follows three main stages that are described as follows [147]:

1. The target (or conditions) of the problem that is defined for the PSO algorithm
2. Global best (gBest) value that determines which particle's data is currently closer to the target
3. Stop condition that determines when the algorithm should be stopped

Also, each particle contains:

1. $\vec{x}_i$; this vector shows the current position in the search space for the particle i
2. $\vec{p}_i$; the best position in history of particle i is defined by this vector

3. $\vec{v}_i$; the particle's velocity of the particle i

4. $pBest_i$; this parameter indicates the quality of solution of the best position of particle i

This optimization algorithm (PSO) update the ANFIS parameters. As above mentioned, the ANFIS has two main parameters that are premise and consequent parameters. The membership functions are assumed Gaussian as in Eq. (3.153), and their parameters are $\{a_i, b_i, c_i\}$ (a_i is the variance of membership functions, b_i is a trainable parameter and c_i is the center of membership functions). These parameters are premise parameters. The consequent parameters were given in Eq. (3.156) that are $\{p_i, q_i, r_i\}$. Therefore, there are three sets of trainable parameters in the premise parameters that each of them has N genes. Here, N demonstrates the number of membership functions. Moreover, the consequent parameters are trained during the optimization process. In conclusion part, each chromosome has $(I + 1) \times R$ genes that I denotes dimension of data inputs and R is equal to number of rules. Indeed, in the first step, the parameters are initialized randomly and then are begin updated using optimization algorithms. One of the parameters set are being updated during each iteration. For instance, in the first iteration the values of a_i are updated and then in the second iteration the values of b_i are updated and then after updating all parameters again, the first parameter update is considered and so on.

3.2.7. Performance evaluation criteria

Three different statistical indicators including root mean square error (RMSE), determination coefficient (R^2) and mean square error (MSE) are considered to evaluate the forecast accuracy of the proposed models. These statistical indicators are calculated by the following equations [148],[149]:

$$RMSE = \sqrt{\frac{1}{n}\sum_{i=1}^{n}(x_i - y_i)^2} \tag{3.158}$$

$$R^2 = \left(\frac{\sum_{i=1}^{n}(x_i - \bar{x})(y_i - \bar{y})}{\sqrt{\sum_{i=1}^{n}(x_i - \bar{x})^2 \sum_{i=1}^{n}(y_i - \bar{y})^2}}\right)^2 \tag{3.159}$$

$$MSE = \frac{1}{n}\sum_{i=1}^{n}(x_i - y_i)^2 \tag{3.160}$$

Here, x_i, y_i, $\bar{x}$, $\bar{y}$ and n are actual value, predicted value, mean of actual data, mean of predicted data and number of data, respectively.

3.3. Hybrid renewable energy analysis

Despite Iran's vast reserves of hydrocarbons, but by looking to Fig. 3.20 it can be found that this country is potentially one of the best regions for solar radiation and wind energy. The Unit 132 of the second refinery is located in the south of Iran (the rectangle on the map, Fig. 3.20). The total area of Bushehr is around 22,743 km^2 and analysis of the data (Fig. 3.20 (a)) illustrated that this area receives an average of 7 kWh/m^2 solar radiation for one day. By considering only 1% of this area with average of 12% energy efficiency, can be obtained around 200 (MWh/day) electrical energy. Also, in recent years, Iran had an impressive growth in wind generation. In 2010, Iran provided 203 MW of electricity from the wind power [150]. Fig. 3.20 (b) illustrates the average wind speed data in Iran that are provided

by renewable energy organization of Iran [151]. Analysis of potential wind energy only in 26 stations of Iran shows these stations with approximately 33% energy efficiency can produce around 6500 MW electrical power [151].
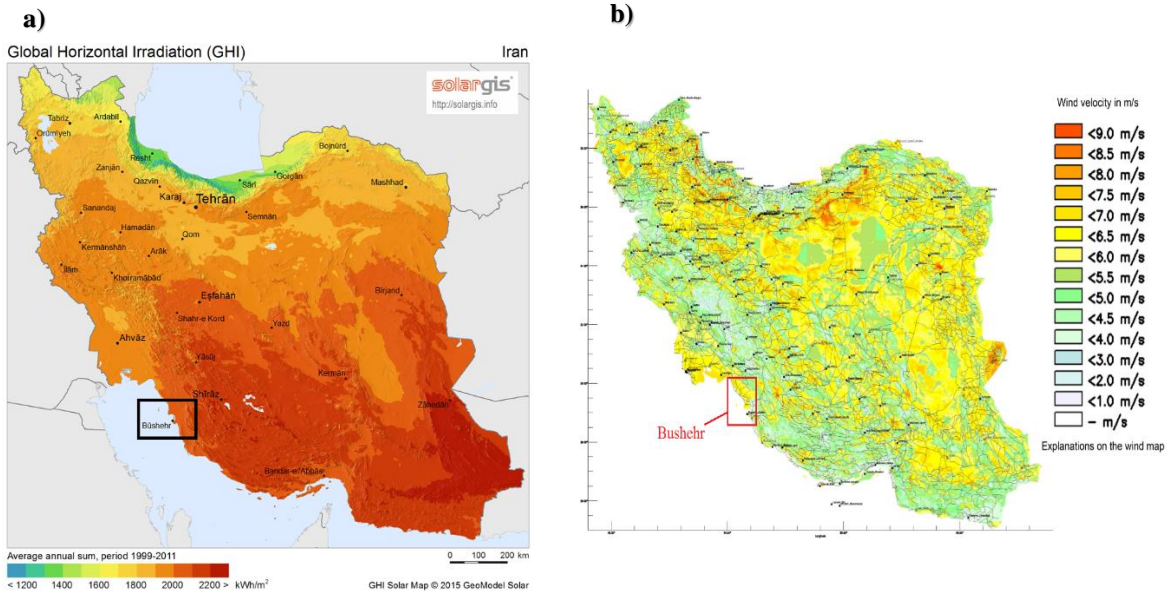
Fig. 3.20. Average annual solar radiation (a) and wind speed (b) [151].

Hybrid PV/wind energy that has been proposed for supplying the electrical energy for Unit 132 is shown in Fig. 3.21. The input energy will be provided by WTS and PVS and whenever there are no solar or wind energies, demanding energy will be supplied by energy storage system. If the total energy produced by renewable energy sources is greater than the energy demand of the unit, the excess electric energy is used by the electrolyzer to produce hydrogen and it is stored in the hydrogen tanks. The fuel cell will use stored hydrogen for supplying the electrical energy as the secondary power source in Unit 132.

Table 3.5 illustrates the technical specification of the PV panel, wind turbine, electrolyzer, fuel cell, hydrogen tank and converter that are the components of the proposed system. It should be noted that for the converter and fuel cell that have less life than 20 years, the additional cost and cost of replacement are considered. As can be seen in the table, the number of solar PV panels (5200) and wind turbines (2) are determined based on the unit required power (7600 kW/day) and produced power by the hybrid PV/WT system. Indeed, the produced power of each PV module and WT (in the case study region) will determine the number of PV panels and WTs. Also, the size of the electrolyzer depends on its input power that is obtained from the renewable energy system. The capacity of the fuel cell is related on the required energy of the unit. A converter is considered aiming to convert the electric current from DC to AC. Moreover, components efficiency are considered in order to select their size.

41
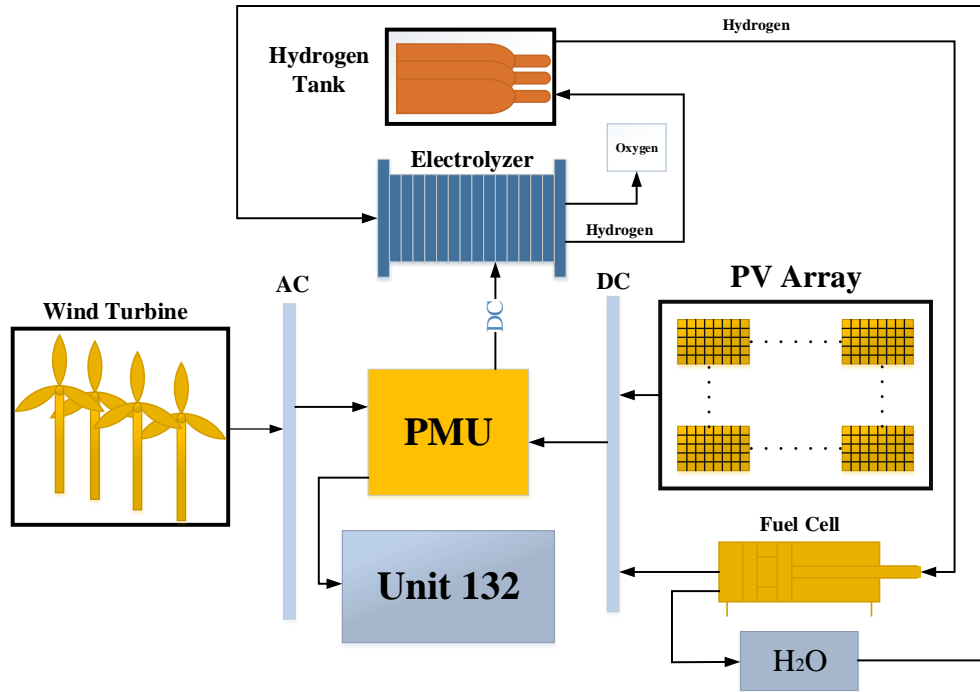
Fig. 3.21. Schematic of the hybrid renewable energy with hydrogen storage system.

Table 3.5. Technical specification of the proposed system.

Parameters	Value		Converter	
Project life time (n_p)	20 years		Initial cost	700 $/kW
Load power of the Unit 132	320 kW		Life time	10 years
Air density (ρ_a)	1.22 kg/m³		Efficiency	95%
LHV (H₂)	141764 kJ/kg		Nominal power	320 kW
T_a	25 ℃		Technical specifications of wind turbine (E-44)	
Characteristics of the PV panel			Rated power:	900 kW
	STC	NOCT	Rotor diameter:	44 m
Maximum power (P_{max})	240 Wp	181.7 Wp	Hub height in meter:	45 / 55
Voltage at maximum power (V_{mpp})	29.7 V	27.1 V	WEC concept:	Gearless, variable speed, single blade adjustment
Current at maximum power (I_{mpp})	8.08 A	6.71 A	Rotor type:	Upwind rotor with active pitch control
Open circuit voltage (V_{oc})	37.3 V	33.9 V	Rotational direction:	Clockwise
Short circuit current (I_{sc})	8.6 A	7.37 A	No. of blades:	3
Temperature		45±2 ℃	Rotational speed:	Variable, 16 - 34.5 rpm
Temperature coefficient of P_{max}	-0.442 %/℃		Annual maintenance costs of wind turbine (C Mnt-WT)	84 $/kW-year
Temperature coefficient of V_{oc}	-0.352 %/℃		Life time	20 years
Temperature coefficient of I_{sc}	0.088 %/℃		Initial cost	3,000 $/kW
Panel dimension (H/W/D)	1655×992×45 mm		Number of turbines	2
Cell type	Polycrystalline		Electrolyzer	
Initial cost	3,300 $/kW		Initial cost	1500 $/kW
Annual maintenance costs	44 $/kW-year		Annual maintenance costs	5% of initial cost-year
Life time	20 to 25 years		Nominal electrolyzer power	1500 kW
Number of PV panels	5200		Electrolyzer efficiency	74%
Hydrogen tank			Fuel cell	
Life time	20 years		Initial cost	2000 $/kW

Initial cost	500 \$/kg	Annual maintenance costs	5% of the initial cost
Capacity	7500 kg	Nominal fuel cell power	450 kW
Annual maintenance costs	5% of initial cost-year	Replacement cost of fuel cell	\$1400

3.3.1. Energy and Exergy analysis

Photovoltaic system:

Klein and Theilacker [152] developed a method for determining the monthly slope and azimuth angles. The total monthly average daily radiation is defined by:

$$\bar{H}_T = \bar{H}\,\bar{R} \tag{3.161}$$

In which, $\bar{H}$ is the monthly average daily radiation on a horizontal surface that is:

$$\bar{H} = \bar{K}_T\,\bar{H}_o \tag{3.162}$$

Where $\bar{H}_o$ is the monthly average daily extraterrestrial radiation and $\bar{K}_T$ is the monthly average clearness index. $\bar{H}_o$ is defined by Eq. (3.163) [153].

$$\bar{H}_o = \frac{24 \times 3600 \times G_{sc}}{\pi}\left(1 + 0.033\,cos\left(\frac{360\,n}{365}\right)\right) \times \left[cos\,\emptyset\,cos\,\delta\,(sin\,\omega_2 - sin\,\omega_1) + \frac{\pi(\omega_2 - \omega_1)}{180}sin\,\emptyset\,sin\,\delta\right] \tag{3.163}$$

In which G_{sc} is the energy from the sun per unit time received on a unit area of surface perpendicular to the direction of propagation of the radiation at mean earth-sun distance outside the atmosphere that is equal to $1367 W/m^2$. Also, n, $\emptyset$, δ and ω are number of the ith day of month, latitude, declination angle, and hour angle.

δ is given by:

$$\delta = 23.45\,sin\left(360\,\frac{284 + n}{365}\right) \tag{3.164}$$

Also, $\bar{R}$ is the ratio of monthly mean daily global solar radiation on an inclined plate to that on a horizontal plate:

$$\bar{R} = D + \frac{\bar{H}_d}{\bar{H}}\left(\frac{1 + cos\beta}{2}\right) + \rho_g\left(\frac{1 - cos\beta}{2}\right) \tag{3.165}$$

Where β is slope angle, and D is calculated by:

$$D = \begin{cases} max\left(0, G(\omega_{ss}, \omega_{sr})\right) \; if \; \omega_{ss} \geq \omega_{sr} \\ max(0, [G(\omega_{ss}, -\omega_s) + G(\omega_s, \omega_{sr})]) \; if \; \omega_{sr} > \omega_{ss} \end{cases} \tag{3.166}$$

In which ω_{ss} and ω_{sr} are the sunset and sunrise hour angles for beam radiation on a tilted surface, respectively. Where $G(\omega_1, \omega_2)$ can be determined by:

$$G(\omega_1, \omega_2) = \frac{1}{2d}\left[\left(\frac{bA}{2} - \acute{a}B\right)(\omega_1 - \omega_2)\frac{\pi}{180} + (\acute{a}A - bB)(sin\omega_1 - sin\omega_2) - \acute{a}C(cos\omega_1 - cos\omega_2)\right.$$
$$\left. + \left(\frac{bA}{2}\right)(sin\omega_1\,cos\omega_1 - sin\omega_2\,cos\,\omega_2) + \left(\frac{bC}{2}\right)(sin_{w_1}^2 - sin_{w_2}^2)\right] \tag{3.167}$$

In which, $\acute{a}$ is:

$$\acute{a} = a - \frac{\bar{H}_d}{\bar{H}} \tag{3.168}$$

Also, ω_{sr} and ω_{ss} are introduced by Eqs. (3.169)- (3.172).

$$|\omega_{sr}| = min\left[\omega_s, cos^{-1}\frac{AB + C\sqrt{A^2 - B^2 + C^2}}{A^2 + C^2}\right] \tag{3.169}$$

$$\omega_{sr} = \begin{cases} -|\omega_{sr}| \ if \ (A > 0 \ and \ B > 0) \ or \ (A \geq B) \\ +|\omega_{sr}| \ otherwise \end{cases} \tag{3.170}$$

$$|\omega_{ss}| = min\left[\omega_s, cos^{-1}\frac{AB - C\sqrt{A^2 - B^2 + C^2}}{A^2 + C^2}\right] \tag{3.171}$$

$$\omega_{ss} = \begin{cases} +|\omega_{ss}| \ if \ (A > 0 \ and \ B > 0) \ or \ (A \geq B) \\ -|\omega_{ss}| \ otherwise \end{cases} \tag{3.172}$$

In which A, B, and C are functions of solar geometry and position of the solar surface that are given by:

$$A = cos\beta + tan\varphi \ cos\gamma \ sin\beta \tag{3.173}$$

$$B = cos\omega_s \ cos\beta + tan\delta \ sin\beta \ cos\gamma \tag{3.174}$$

$$C = \frac{sin\beta \ sin\gamma}{cos\varphi} \tag{3.175}$$

As well as a, b and d are constant coefficients that are given by the following equations:

$$a = 0.4090 + 0.5016 \ sin(\omega_s - 60) \tag{3.176}$$

$$b = 0.6609 - 0.4767 \ sin(\omega_s - 60) \tag{3.177}$$

$$d = sin(\omega_s) - \frac{\pi}{180}cos(\omega_s) \tag{3.178}$$

Monthly average diffuse fraction correlations are defined by [153]:

For $\omega_s \leq 81.4°$ and $0.3 \leq \overline{K}_T \leq 0.8$

$$\frac{\overline{H}_d}{\overline{H}} = 1.391 - 3.560 \ \overline{K}_T + 4.189\overline{K}_T^2 - 2.137\overline{K}_T^3 \tag{3.179}$$

And also for $\omega_s > 81.4°$ and $0.3 \leq \overline{K}_T \leq 0.8$

$$\frac{\overline{H}_d}{\overline{H}} = 1.311 - 3.022 \ \overline{K}_T + 3.427 \ \overline{K}_T^2 - 1.821\overline{K}_T^3 \tag{3.180}$$

The output power of the PV array for the ith hour of the day is:

$$P_i = A_c G_{T,i}\eta_{mp}\eta_e \tag{3.181}$$

In which A_c, $G_{T,i}$, η_{mp} and η_e are the array area, incident solar radiation, the maximum power point efficiency of the array and the efficiency of any power-conditioning equipment, respectively. The maximum power point efficiency is:

$$\eta_{mp} = \eta_{mp,ref}\left[1 + \frac{\mu_{mp}}{\mu_{mp,ref}}(T_a - T_{ref}) + \frac{\mu_{mp}G_T}{\mu_{mp,ref}}\frac{\tau\alpha}{U_L}\left(1 - \frac{\eta_{mp}}{\tau\alpha}\right)\right] \tag{3.182}$$

The term $\eta_{mp}/\tau\alpha$ is always small compared to unity and thus can be approximated by $\eta_{mp,ref}$ without introducing significant error.

Based on the first law of thermodynamics the energy efficiency is:

$$\eta = \frac{energy \ output}{energy \ input} \tag{3.183}$$

The input exergy of the PV system is:

$$E_{x_{in}} = AG_T \left[1 - \frac{4}{3}\left(\frac{T_a}{T_s}\right) + \frac{1}{3}\left(\frac{T_a}{T_s}\right)^4 \right]$$

(3.184)

Also, the exergy output of the PV system is defined by consideration of the thermal and electrical exergy that is:

$$E_{x_{out}} = E_{x_{thermal}} + E_{x_{electrical}}$$

(3.185)

In which, thermal exergy of the system is:

$$E_{x_{thermal}} = Q\left[1 - \frac{T_a}{T_m}\right]$$

(3.186)

Where Q is the heat emitted to the surround which is defined by:

$$Q = UA(T_m - T_a)$$

(3.187)

In which U is the overall heat loss coefficient and is composed of the convection and radiation heat transfer coefficient that are given by the Eqs. (3.188) and (3.189). Convection heat transfer coefficient is:

$$h_{conv} = 2.8 + 3v_m$$

(3.188)

And radiation heat transfer coefficient is proposed by Ref. [154]:

$$h_{rad} = \varepsilon\sigma\left(T_{sky} + T_m\right)\left(T_{sky}^2 + T_m^2\right)$$

(3.189)

In which effective temperature of the sky is $T_{sky} = T_a - 6$.

The temperature of the module based on the normal operating cell temperature is:

$$T_m = T_a + (NOCT - 20)\frac{G_T}{800}$$

(3.190)

Finally, the electrical exergy of the system that has been defined by Ref. [155] is:

$$E_{x_{electrical}} = V_{oc} \times I_{sc} \times FF$$

(3.191)

In which, FF is the fill factor and is equal to:

$$FF = \frac{V_{mp}I_{mp}}{V_{oc}I_{sc}}$$

(3.192)

The exergy efficiency based on the second law of thermodynamics is expressed by:

$$\psi = \frac{Exergy\ output}{Exergy\ input}$$

(3.193)

Wind turbine system:

The energy analysis for a WT is defined by the following equation:

$$ke_1 = w_{out} + ke_2$$

(3.194)

In which ke and w_{out} are the kinetic energy of the wind-flow and the output work that extracted by rotor blades, respectively. Eq. (3.195) defines the kinetic energy of the wind:

$$ke = \frac{1}{2}\rho Atv^3$$

(3.195)

For any design of WT the theoretical maximum power efficiency (Cp_{max}) is around 59%. Since WT cannot work in the Cp_{max}, the actual generated power for each WT is:

$$P_m = \frac{1}{2}\rho CpAv^3$$

(3.196)

45

Fig. 3.22 shows a schematic of three main sections of a WTS. The mechanical power of the rotor is calculated by Eq. (3.197). It must be determined how much of this power will be transferred to the electrical grid. For this target, according to Fig. 3.22, it is necessary to calculate the efficiencies of the gearbox, generator and power electronics. The amount of the actual generated power is:

$$P_e = \eta_{gb}\,\eta_{gn}\,\eta_p\,P_m \tag{3.197}$$

The efficiencies of the gearbox, generator and power electronics device were assumed to be η_{gb}=0.95, η_{gn}=0.97 and η_p=0.98, respectively [156].

Fig. 3.22. Three main sections of a wind turbine.

Exergy analysis for WT is given by the following equation:

$$\dot{Ex}_{flow_1} = \dot{W}_{out} + \dot{Ex}_{flow_2} + \dot{Ex}_{dest} \tag{3.198}$$

In which $\dot{Ex}_{flow_1}$ is the exergy rate of the flow in the inlet of WT, $\dot{W}_{out}$ is the rate of the output work and $\dot{Ex}_{dest}$ is defined as the rate of the exergy destruction of the WT. The $\dot{Ex}_{flow_1}$ is:

$$Ex_{flow} = \left(Ex_k + Ex_p + \Delta H - T_a\Delta S\right) + Ex_{ch} \tag{3.199}$$

Where Ex_k, Ex_p, ΔH, T_a, ΔS and Ex_{ch} are kinetic energy, potential energy (is considered to be zero), change in enthalpy, ambient temperature, change in entropy and chemical energy. The kinetic exergy is:

$$Ex_k = E_{generated} \tag{3.200}$$

the enthalpy difference is calculated by:

$$\Delta H = \dot{m}cp_a(T_2 - T_1) \tag{3.201}$$

in which, $\dot{m}$, cp_a, T_1 and T_2 are the mass flow rate of the air, the air specific heat and the wind chill temperature at the inlet and outlet of the WT, respectively. The wind chill temperature is [157]:

$$T_{i,wind-chi} = 13.12 + 0.6215T_a - 11.37v_i^{0.16} + 0.3965T_a v_i^{0.16} \tag{3.202}$$

The wind speed and $T_{i,wind-chi}$ are at 10-meter elevation and ℃, respectively. The amount of the wind speed after the WT is defined by Sahin et al. [157] correlation.

$$v_2 = \sqrt[3]{\frac{2\left(E_{potential} - E_{generated}\right)}{\rho At}} \tag{3.203}$$

Physical exergy of the air is given by an equation that has been developed by Bejan et al. [138].

$$Ex_{ph} = (cp_a + \Omega cp_v)T_0\left[\frac{T}{T_0} - 1 - ln\left(\frac{T}{T_0}\right)\right] + (1 + 1.6078\Omega)RT_0 ln\left(\frac{P}{P_0}\right) \tag{3.204}$$

In which cp_a, cp_v, Ω, R and P_0 are the air specific heat, vapor specific heat, humidity ratio, gas constant and reference pressure. The pressure in the inlet and outlet of the WT is:

$$P_i = P_a \pm \frac{\rho}{2}v_i^2 \tag{3.205}$$

The chemical exergy is:

$$Ex_{ch} = RT_0[(1 + 1.6078\Omega)ln[(1 + 1.6078\Omega_0)/(1 + 1.6078\Omega)] + 1 + 1.6078\Omega ln(\Omega/\Omega_0)] \tag{3.206}$$

Also, heat loss of the WT is:

$$\dot{Q}_{loss} = \dot{m}_a cp_a(T_2 - T_1) \tag{3.207}$$

And entropy generation is:

$$\dot{I} = T_0\left(cpln\left(\frac{T_2}{T_1}\right) - Rln\left(\frac{P_2}{P_1}\right) - \frac{\dot{m}cp(T_a - T_{ave})}{T_a}\right) \tag{3.208}$$

The specific exergy destruction can be defined by:

$$Ex_{des} = \frac{T_0\Delta S}{\rho A v} \tag{3.209}$$

Finally, the energy and exergy efficiencies of the WT are:

$$\eta = \frac{\dot{W}_{out}}{P} \tag{3.210}$$

$$\psi = \frac{\dot{W}_{out}}{\dot{E}x_{flow}} \tag{3.211}$$

Electrolyzer and fuel cell:

Based on the following formula, electrolyzer splits water into hydrogen and oxygen using the excess electrical energy from PVS and WTS.

$$H_2O + Power \rightarrow H_2 + 1/2\, O_2 \tag{3.212}$$

The energy efficiency of the electrolyzer is defined by the lower heating value of hydrogen produced and power consumed by the process and is given by:

$$\eta = \frac{\dot{m}_{H_2}LHV_{H_2}}{Power\ input} \tag{3.213}$$

The exergy efficiency of the electrolyzer is given by consideration of physical and chemical exergy of the hydrogen and is defined by Eq. (3.124).

$$\varepsilon = \frac{\dot{E}x_{H_2}}{Power\ input} = \frac{\dot{m}_{H_2}(ex_{ph} + ex_{ch})_{H_2}}{Power\ input} \tag{3.214}$$

Physical exergy of the hydrogen is:

$$ex_{ph} = (h - h_0) - T_0(s - s_0) \tag{3.215}$$

And for an ideal gas it can be written as:

47

$$ex_{ph} = c_p T_0 \left[\frac{T}{T_0} - 1 - ln\left(\frac{T}{T_0}\right) + ln\left(\frac{P}{P_0}\right)^{\frac{k-1}{k}} \right]$$
(3.216)

In which c_p, T_0, P_0 and k are the heat capacity at the constant pressure, ambient temperature, ambient pressure and the adiabatic exponent.

Also, physical exergy is given by:

$$ex_{ch} = \sum x_{H_2} ex_{0,H_2} + R_{H_2} T_0 \sum x_{H_2} ln\, x_{H_2}$$
(3.217)

Economic analysis:

The life cycle cost (LCC) is used of hybrid system that was considered in this study. It is defined by consideration of the annual capital cost (CC), the annual maintenance cost (MC), the cost of installation (IC) and the cost of replacement (RC) of the components.

$$LCC = CC + MC + IC + RC$$
(3.218)

LCC of photovoltaic system:

The initial capital cost of the PVS is determined as:

$$CC_{PV} = A_{PV} C_{PV} \left(\frac{i_r (1 + i_r)^{n_p}}{(1 + i_r)^{n_p} - 1} \right)$$
(3.219)

in which A_{PV}, C_{PV}, i_r and n_p are area of PV array, unit cost of the PV panels, interest rate of the system and the life span, consecutively.

Also, the annual maintenance cost is defined by:

$$MC_{PV} = C_{Mnt-PV}\, A_{PV}$$
(3.220)

where C_{Mnt-PV} is annual maintenance cost of each PV panel.

LCC of wind turbine system:

The annual capital cost for WTS according to the swept area of the blades (A_{WT}) is:

$$CC_{WT} = A_{WT} C_{WT} \left(\frac{i_r (1 + i_r)^{n_p}}{(1 + i_r)^{n_p} - 1} \right)$$
(3.221)

In which C_{WT} is the unit cost of the WTS that is defined by the initial cost of each WT and the cost of installation of WT.

The annual maintenance cost for WTS can be evaluated as following equation:

$$MC_{PV} = C_{Mnt-PV} A_{PV}$$
(3.222)

LCC of fuel cell and electrolyzer:

As well as the capital cost of the fuel cell is expressible as:

$$CC_{FC} = PW_{FC} \cdot \left(\frac{i_r (1 + i_r)^{n_p}}{(1 + i_r)^{n_p} - 1} \right)$$
(3.223)

In which PW_{FC} is the single payment present worth factor. It should be noted that the life time of fuel cell and electrolyzer are considered five years [125].

$$PW_{FC} = C_{FC} \sum_{k=0,5,10,15} \frac{1}{(1+i_r)^k} \tag{3.224}$$

where C_{FC} is the fuel cell cost.

Also, LCC of electrolyzer is obtained as a same way as before explained for the fuel cell.

LCC of hydrogen tank (H₂):

The capital cost of the hydrogen tank is determined by the following equation:

$$CC_{HT} = N_{H_2}.C_{H_2} \left(\frac{i_r(1+i_r)^{n_p}}{(1+i_r)^{n_p} - 1} \right) \tag{3.225}$$

In which N_{H_2} and C_{H_2} are number of hydrogen tank and the initial cost of an electrolyzer.

Chapter 4
Results and Discussion

4.1. Refrigeration unit

The operating conditions of the proposed systems are obtained with a mathematical modeling of the thermodynamic cycle in EES software. Table 4.1 illustrates a comparison between the simulated cycle and actual data of Unit 132 of the refinery. The results show the errors ((actual data − simulated data/actual data) × 100) are less than 5 percent which are due to the theoretical assumption and error of the numerical value of the refrigerant properties in the software with the actual data of the cycle.

Table 4.1. Comparison between actual data of the cycle and simulated data in the software.

	Actual data of the cycle	Simulated data by software	Error (%)
Mass of flow (kg/s)	12.6	12.4	1.59
Work of compressor (kW)	371.2	381.4	-2.75
Heat loss from the air condenser (kW)	2002	2032	-1.5
Temperature of the cold fluid in the outlet of the heat exchanger (℃)	34	33.95	0.147
Temperature of the hot fluid in the outlet of the heat exchanger (℃)	56	55.47	0.946

The EERS is compared with Sarkar [158] system on isobutane as working fluid. With condensing temperature varying from 35 to 55℃, the comparison for T_{eva}=15℃, $\eta_{sn}, \eta_{mn}, \eta_d$=0.85, and η_{ms}=1 is shown in Fig. 4.1 As can be seen in the graph, the COP calculated from the present model is in agreement with Sarkar [158].
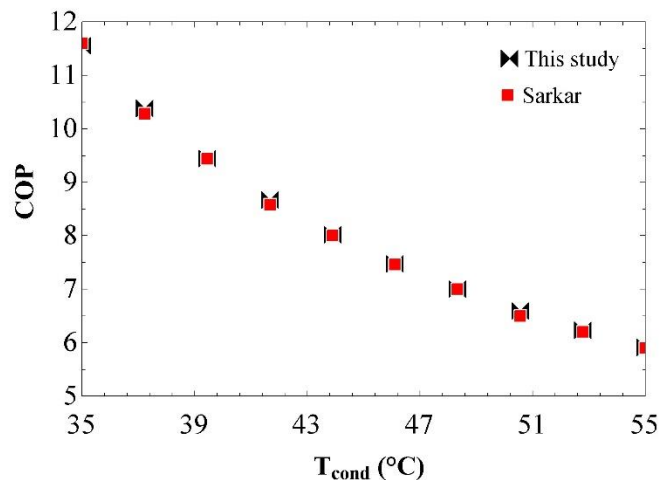
Fig. 4.1. Comparison between the proposed model and Sarkar [158].

Tables 4.2-4.4 represents the sizing of the evaporator, condenser, and ejector before and after optimization for the R134a EERS. By considering the optimum evaporation and condensing temperatures, the area of the evaporator (from

193.4 m² to 148.3 m²) and condenser (from 975.5 m² to 926.7 m²) decrease. For the ejector device by considering the optimum temperatures, the values of the $D_{mn,t}$, $D_{mn,t}$, $D_{mn,t}$, and $D_{mn,t}$ increase approximately by 4%.

Table 4.2. Sizing of the evaporator.

	Exist evaporator	Optimized evaporator
Area of the evaporator	$193.4\ m^2$	$148.3\ m^2$
Cylinder outside diameter	700 mm	650 mm
Cylinder inside diameter	684 mm	634 mm
Tube length	5000 mm	4500mm
Number of tube	622	530
Tube pith	25 mm	25 mm
Tube passes	1	1
Tube outer diameter	20 mm	20 mm
Tube wall thickness	1.65 mm	1.65 mm
Number of baffle	6	6
Baffle thickness	9.52 mm	9.52 mm

Table 4.3. Sizing of the condenser.

	Exist condenser	Optimized condenser
Area of the condenser	$975.5\ m^2$	$926.7\ m^2$
Unit length	6609.6 mm	6609.6 mm
Width	1489.82 mm	1421.48mm
Tube passes	2	2
Number of fan	4	4
Fan blade diameter	1371.6 mm	1371.6 mm
Tube outer diameter	30 mm	30 mm
Tube wall thickness	1.65 mm	1.65 mm
Fin thickness	0.58 mm	0.58 mm
Fin outer diameter	62 mm	62 mm
Header width	1354.05 mm	1285.7 mm
Header depth	304.8 mm	304.8 mm
Header height	533.85	533.85

Table 4.4. Sizing of the ejector.

$\dfrac{L_{mn,1}}{D_{mn,1}}$	$\theta_{mn,1}$	$\dfrac{L_{mn,2}}{D_{mn,e}}$	$\theta_{mn,2}$	$\dfrac{L_{sn}}{D_{sn}}$	θ_{sn}	$\dfrac{L_{ms}}{D_{ms}}$	$\dfrac{L_d}{D_d}$	θ_d	$D_{mn,e}$	$D_{mn,t}$	D_{ms}	$D_{sn,e}$
1	23	11.11	1.3	1	18.4	11	4	3.8	0.2668	0.1323	0.5546	0.6107
									With optimum T_{eva} and T_{cond}			
			Proposed by Ref. [159]						0.2773	0.1375	0.5777	0.6239

Also, Chainwongsa et al. [159] and Disawas et al. [161] have proposed different values for $L_{mn,2}/D_{mn,e}$ and $\theta_{mn,2}$ which are 8 and 2.3, respectively.

Energy analysis based on the first law of thermodynamics was done for the EERS and HXRS and is shown in Fig. 4.2. Both systems are investigated with R134a, R407C, and R410A refrigerants. The COP is a ratio of useful cooling provided to work required that as is presented in the graph, the EERS is more efficient system compared with the HXRS. Also, R134a is more efficient than R407C and R410A for the both proposed systems. The COP of the R134a EERS is 11% more than R134a HXRS. Bilir Sag et al. [162] proposed an ejector for a refrigeration system and

51

concluded that the COP increased about 7 to 11%. Also, Aghazadeh Dokandari et al. [163] in a refrigeration system with an ejector obtained a COP improvement of about 5 to 7% over the standard refrigeration cycle. Deng et al. [164] illustrated that the ejector as expander device in a refrigeration system improved the COP by up to 22%. According to the results of this study and before mentioned studies, it can be concluded that ejector expansion device can improve the COP of the cycle. This system is an ideal system from a thermodynamic point of view, but it might not be able to pass the economic criteria. Hence, thermos-economic assessment is investigated in the following of this study.
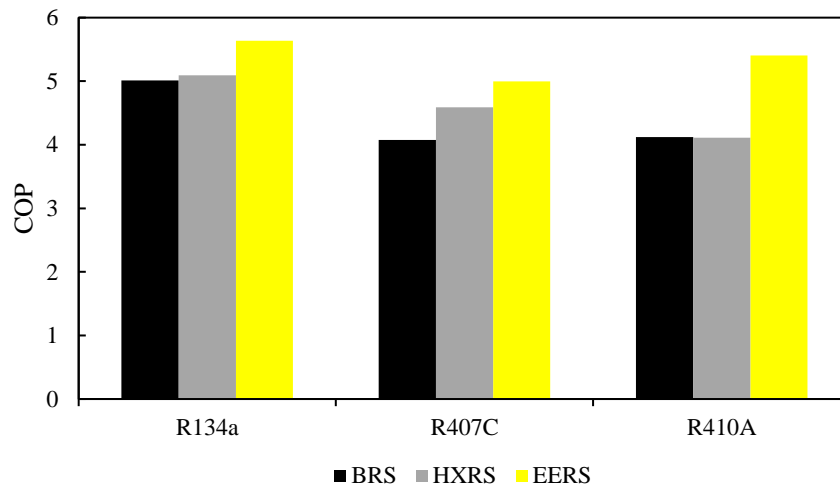
Fig. 4.2. Comparison between the EERS and HXRS based on energy analysis.

Fig. 4.3 represents the exergy analysis based on the second law of thermodynamics for the EERS and HXRS. R134a, R410A, and R407C are considered as working fluid for each system. In this graph, the exergy destruction for each component of the system is given. Minimum and maximum HXRS exergy destruction are obtained for the middle heat exchanger and condenser, respectively. For the EERS, the ejector and condenser have the lower and higher exergy destruction, respectively. Exergy destruction for the expansion valve in the HXRS accounts for 19% (40.67 kW) of the total; this value in the EERS is less than 1% (0.6471 kW) of the total. The lower exergy destruction is achieved for the EERS with R134a refrigerant. The amount of the exergy destroyed for the R407C EERS is lower than R410A EERS. Deng et al. [46] investigated the exergy destroyed for an EERS and concluded that the exergy destruction for the EERS is less than the standard refrigeration system.
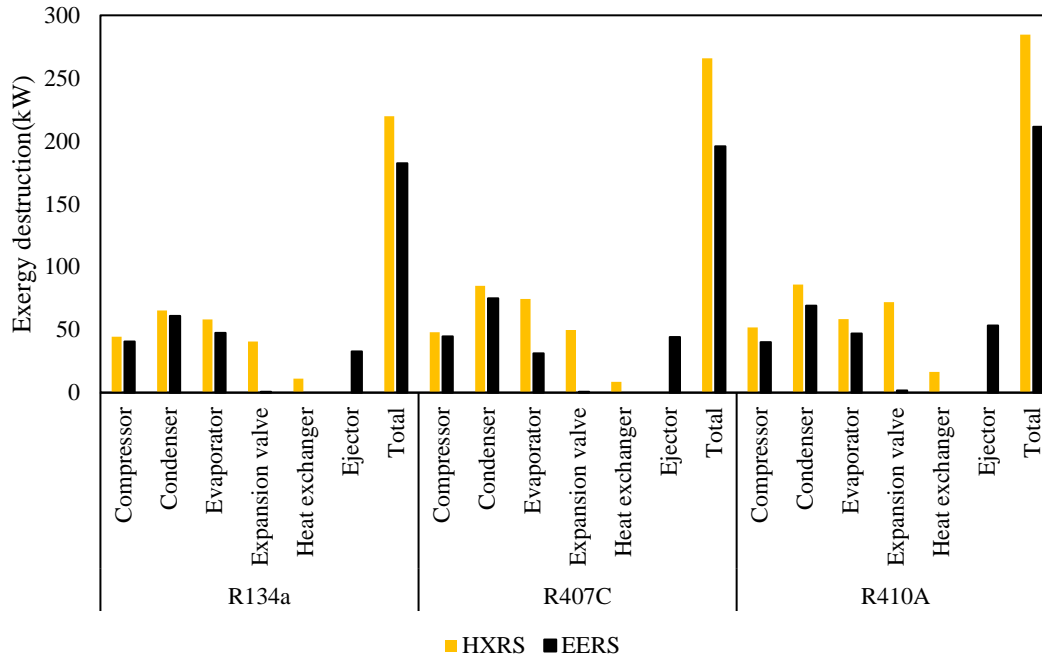
Fig. 4.3. Exergy analysis in each component with different refrigerants on the EERS and HXRS.

Fig. 4.4 demonstrates the effect of pressure drop in suction nozzle on COP, $COP_{imp}(COP - COP_{BRS}/COP_{BRS})$, VCC, $VCC_{imp}(VCC - VCC_{BRS}/VCC_{BRS})$, PR, and PLR. This variation can be divided into two sections. From $\Delta P = 0.5$ kPa to 20 kPa and from 20 kPa to 50 kPa. The graph represents with the pressure drop increasing, the COP, COP_{imp}, VCC, VCC_{imp}, and PR first increase up to a peak value and then decrease. Therefore it is found that there is an optimum pressure drop in the EERS that leads to a maximum performance of the system. This pressure drop causes an increasing for COP and VCC from 5.57 to 5.63 (1.077 %) and 4210 to 4250 (1%) kJ/m³, respectively. It is found an advantage for ejector cycle that recovers the throttling loss and decreases the pressure ratio ($PR = P_2/P_1$) of the compressor that it leads to decrease the work of the compressor. The amount of the PR for the basic refrigeration cycle is 2.708 kPa and this value for EERS in $\Delta P = 20 \, kPa$ is equal to 2.480 kPa. Also, the pressure lift ratio between $\Delta P = 0.5$ kPa and 20 kPa changes from 1.080 to 1.092. The optimum pressure drop was considered 20 kPa in which the maximum COP_{imp} and VCC_{imp} will be obtained that are 0.124 and 0.112 respectively. This conclusion has an agreement with the previous studies [36], [165].
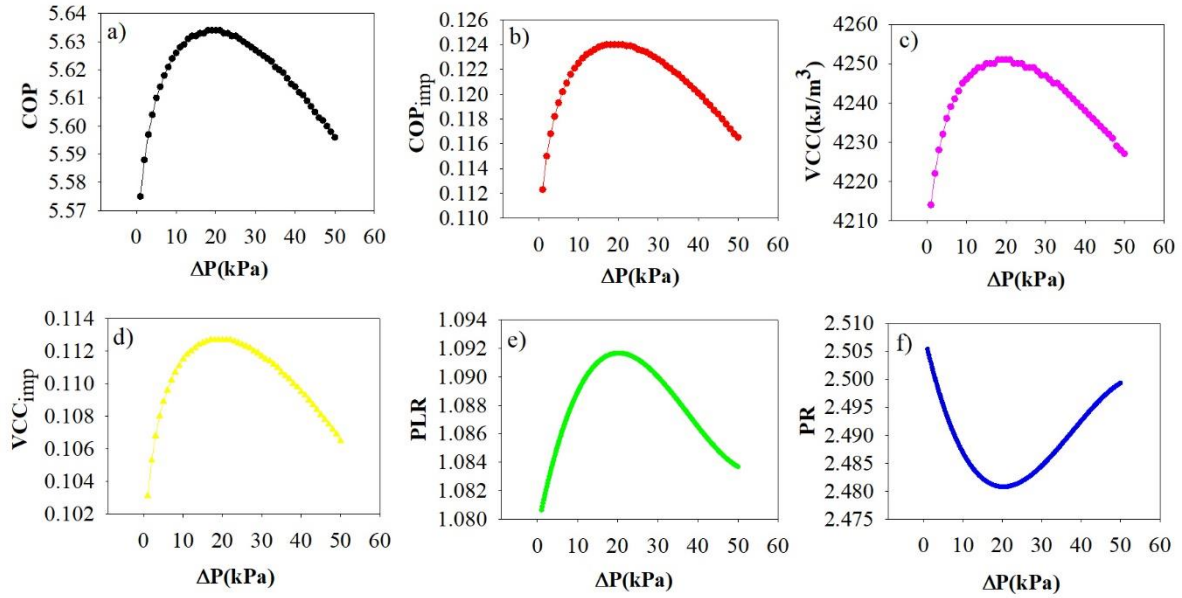
Fig. 4.4. Pressure drop in suction nozzle variation versus COP, COP_{imp}, VCC, VCC_{imp}, PR, and PLR.

Fig. 4.5 illustrates the effect of the condensing temperature on AR, COP, COP_{imp}, VCC, PLR, and PR. The results demonstrate that the AR for the R134a EERS at constant evaporation temperature with an increase in the condensing temperature increases (for each 1℃, 0.03% increment). As the condensing temperature increases from 54℃ to 62℃, the COP decreases and PR increases which led the power of the compressor to increase. The increase in the compressor power causes system COP to decrease as seen in Fig. 4.5 (this conclusion is in agreement with [50]). Also, when the condensing temperature increases, the VCC and PLR increase, and COP_{imp} decreases. PLR is defined as (P_6/P_9) and when the condensing temperature increases, the value of P_6 increases that led the PLR to rise. Also, the variation of the VCC is justified by Eq. (3.28) in which with the condensing temperature increasing, the specific volume in the inlet of compressor decreases that leads to increases in VCC. Clearly, the efficiency of the EERS is directly proportional to condensing temperature.
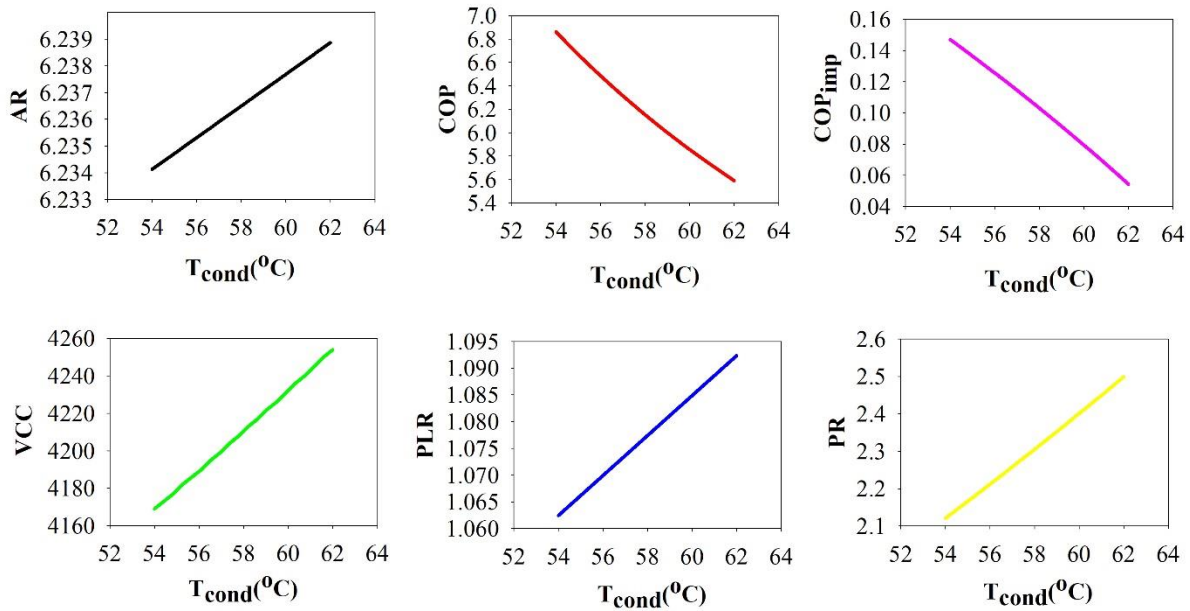
Fig. 4.5. Condensation temperature variation versus COP, COP_{imp}, VCC, VCC_{imp}, PR and PLR.

Fig. 4.6 represents the variation of evaporation temperature on COP_{imp}, VCC_{imp}, and PLR. The graph shows that for a constant condensing temperature (61.66°C), COP_{imp} increases with an increase in the evaporation temperature. The effect of the changing evaporation temperature on VCC_{imp} demonstrates that VCC_{imp} decreases from 0.14 to 0.06. The obtained conclusion is in agreement with [36]. Also, according to Eq. (3.26) with an increment for evaporation temperature, the amount of the evaporation pressure increases, as a result, the value of PLR decreases.
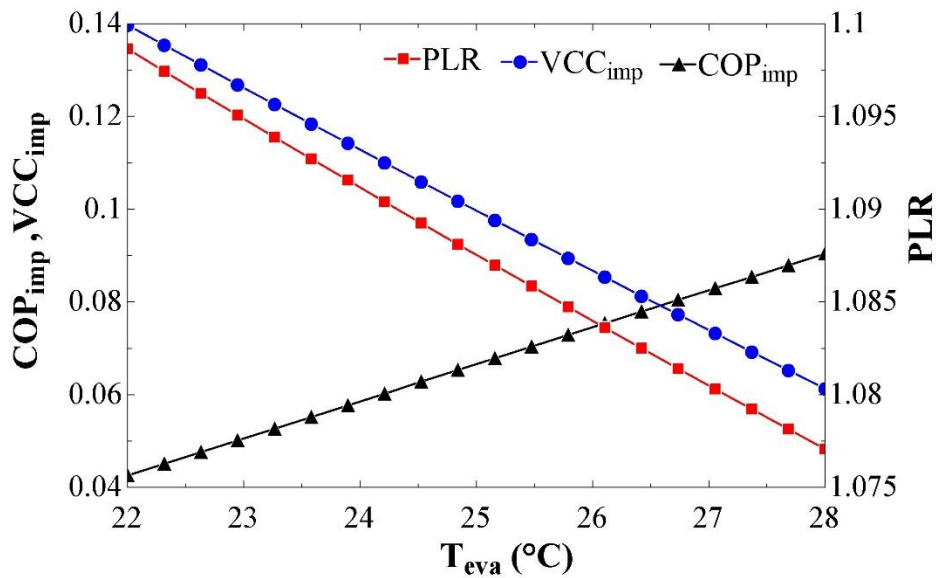
Fig. 4.6. Evaporation temperature changing on COP_{imp}, VCC_{imp} and PLR.

Effect of pressure drop in suction nozzle, evaporation and condensing temperatures on ejector diameters is shown in Figs. 4.7, 4.8, and 4.9. Fig. 4.7 demonstrates the effect of the pressure drop in suction nozzle on motive nozzle throat, motive nozzle exit, suction nozzle exit, and mixing section diameters. Based on Eq. (3.84) when the pressure drop in suction nozzle decreases the amount of the $\dot{m}_9$ decreases and the mass flux in suction nozzle exit increases which leads the suction nozzle exit diameter decreases. Also, the mixing section diameter decreases with a lower tilt compared to the suction nozzle diameter. Motive nozzle throat and motive nozzle exit diameters have a fairly steady trend. Fig. 4.8 represents the effect of the evaporation temperature on the ejector diameters. Based on the data in the figure when the evaporation temperature increases the entire ejector diameter decrease. The motive nozzle exit diameter decreases as a result of decreasing in the $\dot{m}_3$ and increasing in mass flux at the outlet of motive nozzle simultaneously (based on Eq. (3.77)). Increasing in evaporation temperature causes the critical mass flux in the motive nozzle throat remains unchanged and by decreasing the $\dot{m}_3$, throat diameter decreases. As the evaporation temperature increases the amount of the $\dot{m}_9$ increases but the mass flux in suction nozzle increases with a higher rate than $\dot{m}_9$. Therefore based on Eq. (3.84) the suction nozzle diameter decreases. Fig. 4.9 shows the effect of the condensation temperature on the ejector diameters. Based on Eq. (3.90) when the condensation temperature increases, the amount of the $\dot{m}_{tot}$ increases (0.14%). On the other hand, the mass flux in the mixing section increases by 13.54%. As a result, the rate of the increase of the mass flux in the mixing section is higher than $\dot{m}_{tot}$ which leads the mixing section diameter to decrease. There is no remarkable variation on the $D_{mn,t}$, $D_{mn,e}$ and $D_{sn,e}$ with condensation temperature increasing. These conclusions are in agreement with the conclusions of Hassanain et al. [33] study.
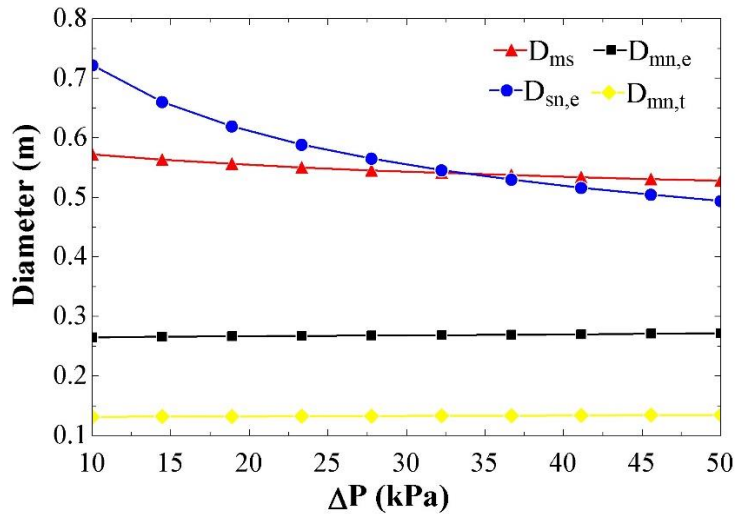
Fig. 4.7. Effect of pressure drop in suction nozzle over the ejector diameters.
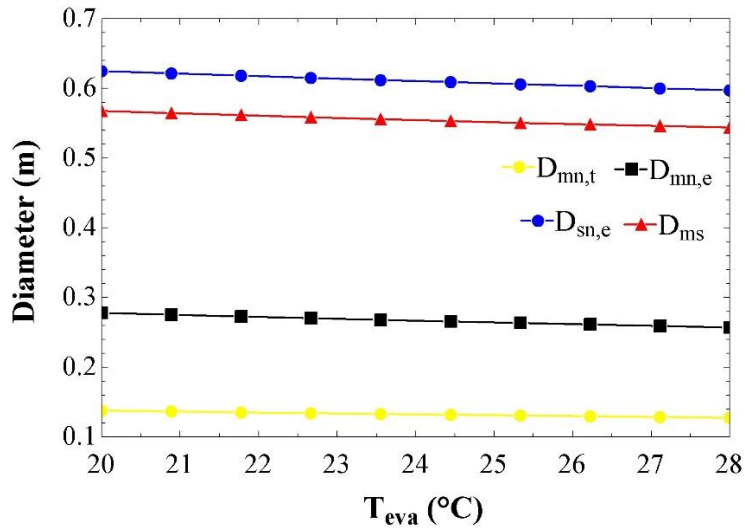
Fig. 4.8. Effect of evaporation temperature on the ejector diameters.
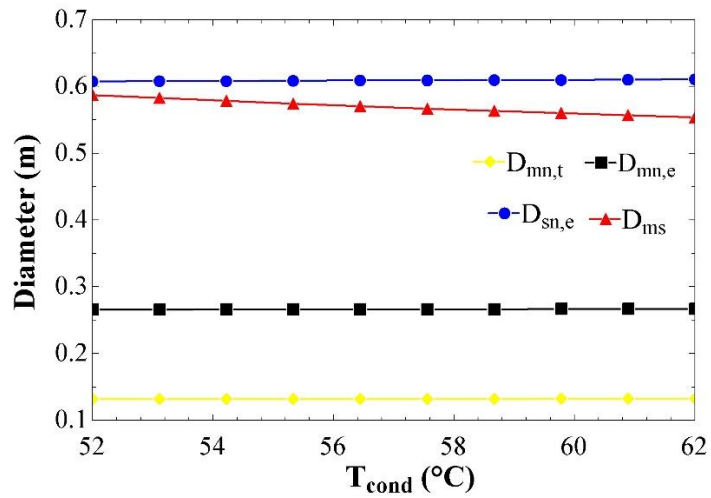
Fig. 4.9. Effect of condensing temperature on the ejector diameters.

The effect of changing pressure drop in suction nozzle on COP has been investigated in the previous section (Fig. 4.4) and the optimum value has been obtained for designing the ejector. Fig. 4.10 shows this investigation on the cost of the ejector which illustrates the optimum ΔP leads to the maximum cost of the ejector. As regards the cost of the ejector compared to the profit of higher performance of the system is negligible so $\Delta P = 20\ kPa$ is considered for designing the ejector in suction nozzle. Also, when the evaporation and condensing temperature increase the value of PEC_{eje} increases.
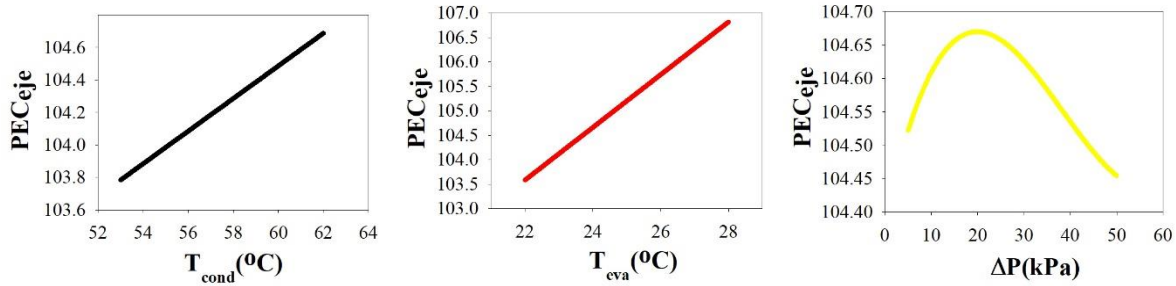
Fig. 4.10. Variation of the pressure drop over cost of ejector device.

The total costs of components that include the cost of investment and maintenance costs are analyzed and shown in a pie chart in Fig. 4.11. It can be seen that the highest portion of costs is occupied by condenser by approximately 75 percent. This analysis is carried out for the EERS and HXRS with R134a refrigerant. It is noteworthy that the percentage of the costs for evaporator in the EERS is more than HXRS and the portion of the compressor is almost steady for both systems. Fig. 4.12 demonstrates the costs of the components and purchased power of the proposed systems. The pie chart shows the percentage of purchased power for the EERS is approximately 59% whereas this value for the HXRS is around 64%.

Fig. 4.11. Proportion of each components of the EERS and HXRS over the costs.
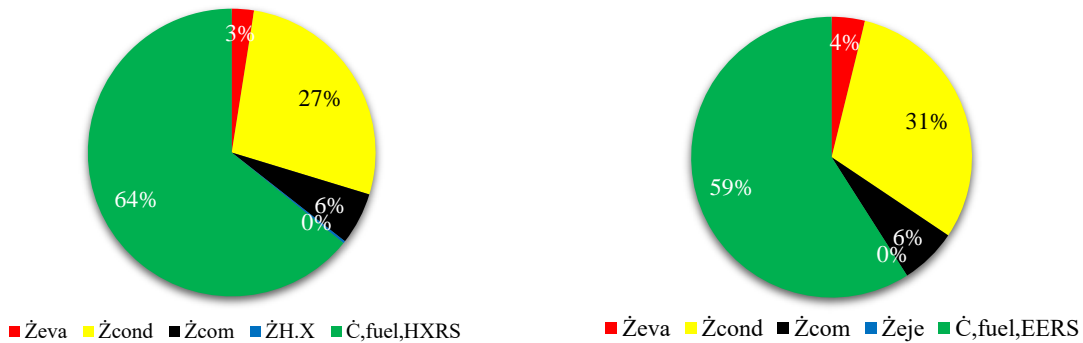
Fig. 4.12. Proportion of the components over the costs of equipment and purchased fuel.

As can be seen in Fig 4.13, the effect of the changing evaporation temperature on the rate of the total costs of the components is evaluated. According to the figure, there is a moderate decrease in the costs of compressor versus T_{eva}

increasing. The evaporation temperature changes between 18℃ and 28℃. It is clear that during evaporation temperature variation, the amount of the $\dot{Z}_{eje}$ and $\dot{Z}_{cond}$ don't have a significant change. As the evaporation temperature increases, the trend of $\dot{Z}_{eva}$ observes a gradual rise.
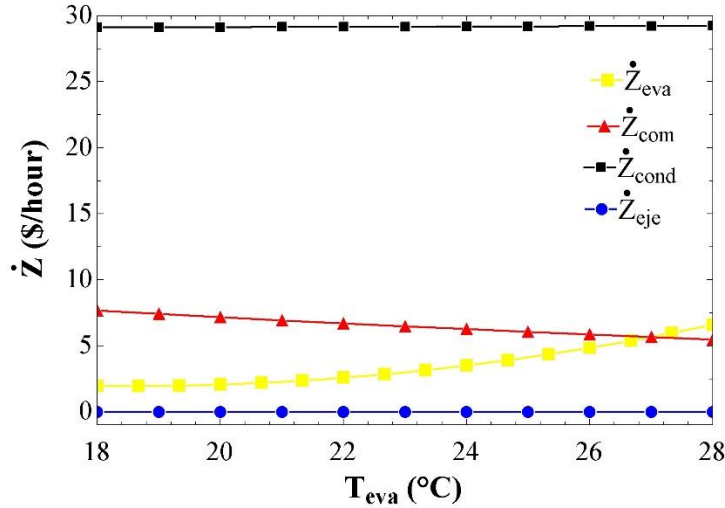
Fig. 4.13. Rate of the total cost in each component according to the changing evaporation temperature in the R134a EERS.

The total costs of the condenser, evaporator, compressor, and ejector versus the changing condensing temperature is shown in Fig. 4.14. The results indicate when the condensing temperature increases (from 50 ℃ to 63℃), the amount of the $\dot{Z}$ for the ejector and evaporator is fairly steady over all the variation and the $\dot{Z}$ for the compressor gradually increases (almost 5% increases for 1℃ increment in T_{cond}). But the trend of the $\dot{Z}_{cond}$ can be divided into two distinct section: from $T_{cond} = 50℃$ to 58.5℃ in which the rate of costs decrease and after that from 58.5℃ to 63℃, it increases.
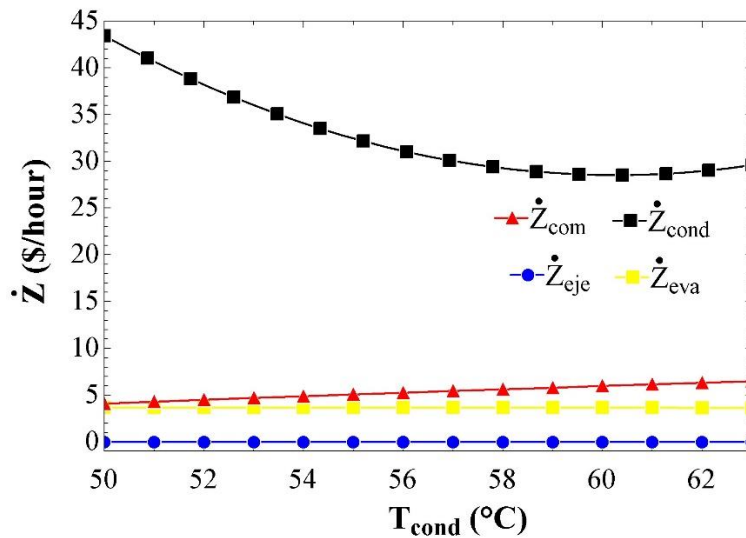
Fig. 4.14. Cost of each component versus condensing temperature in the R134a EERS.

Fig. 4.15 represents the effect of changing T_{eva}, R134a evaporation temperature, on costs of the components (by considering the cost of investment, operating and maintenance costs) of the EERS. As can be seen, the value of the

59

$\dot{Z}_k$ decreases from 18°C to 20°C and then increases from 20°C to 28°C. Therefore, the minimum $\dot{Z}_k$ is obtained by considering $T_{eva} = 20$°C for designing the evaporator.
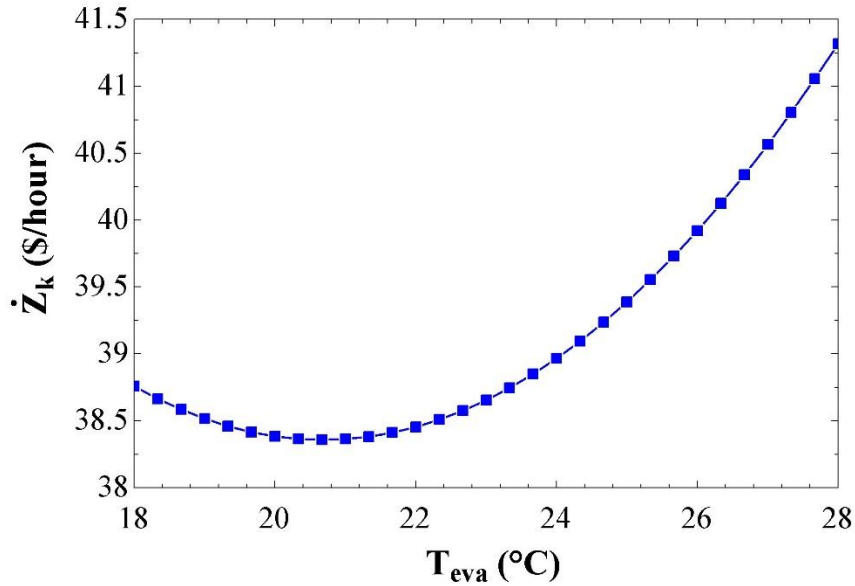
Fig. 4.15. Variation of T_{eva} versus the total cost of components in the R134a EERS.

Also Fig. 4.16 illustrates the variation of the condensing temperature on the $\dot{Z}_k$ for the R134a EERS. As can be seen, with the condensing temperature increasing (from 50°C to 58.50°C), the $\dot{Z}_k$ of the system first decreases and it reached to the minimum value and then increases. As a result, it is proposed to consider the condensing temperature as 58.50°C in which the minimum cost of the components was obtained.
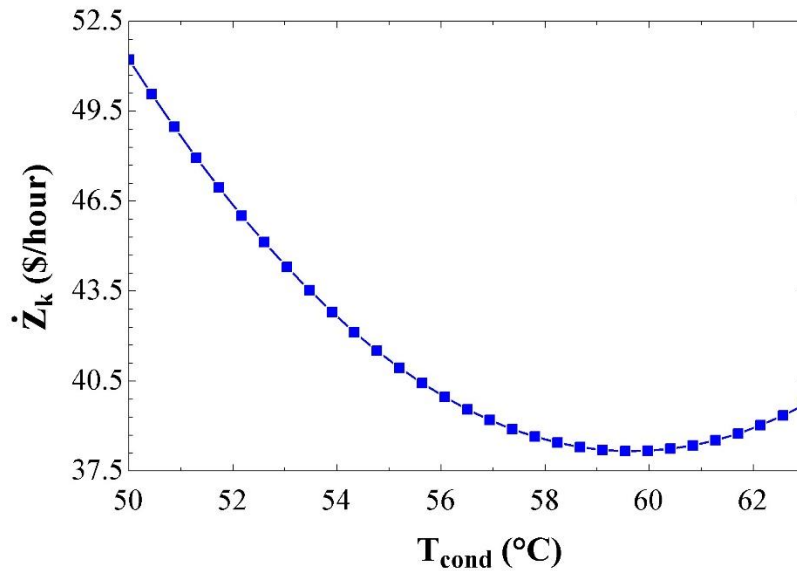
Fig. 4.16. Investigation on changing condensing temperature versus the total cost of components in the R134a EERS.

The total cost of the components ($\dot{Z}_k$), the cost of the fuel ($\dot{C}_{fuel}$), and the total cost of the refrigeration system ($\dot{C}_p$) are evaluated in Fig. 4.17. This figure shows $\dot{C}_p$ for the EERS is less than HXRS. The cost of the components for the R134a EERS are 3% lower than R134a HXRS. The fuel of the system for the EERS is approximately 22% lower than HXRS which it is the important parameter for this analysis. Also, the final goal of this analysis that is $\dot{C}_p$, for the R134a EERS is reported 15.2% lower than R134a HXRS.
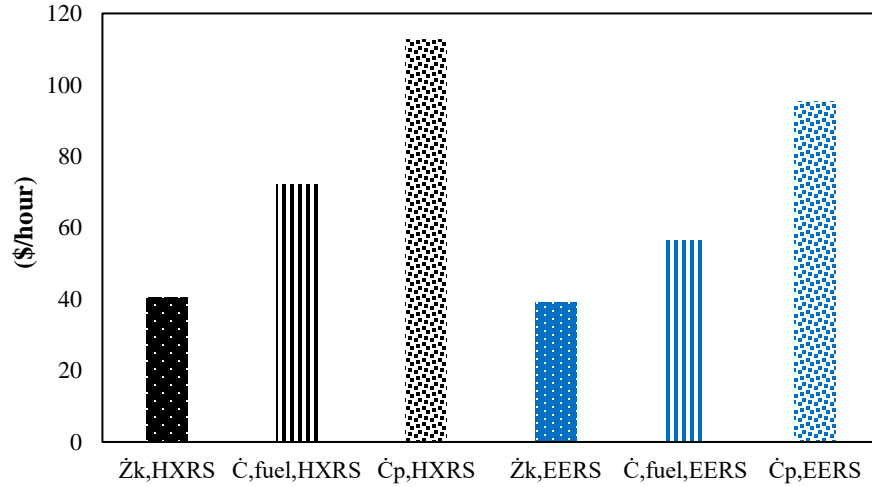
Fig. 4.17. Comparison of the costs of the components, fuel and total cost of RS on the EERS and HXRS.

Considering the environmental impacts is necessary for designing and modeling the thermal and cooling new systems due to the increasing environmental concerns and specifically global warming issues [166]. The amount of the CO, CO_2, and NO_x that were released by the BRS, HXRS, and EERS is shown in Fig. 4.18. It is shown CO_2 has the maximum value of the pollution and this investigation is for three systems with three refrigerants. The lowest contamination is seen for EERS with R134a refrigerant.
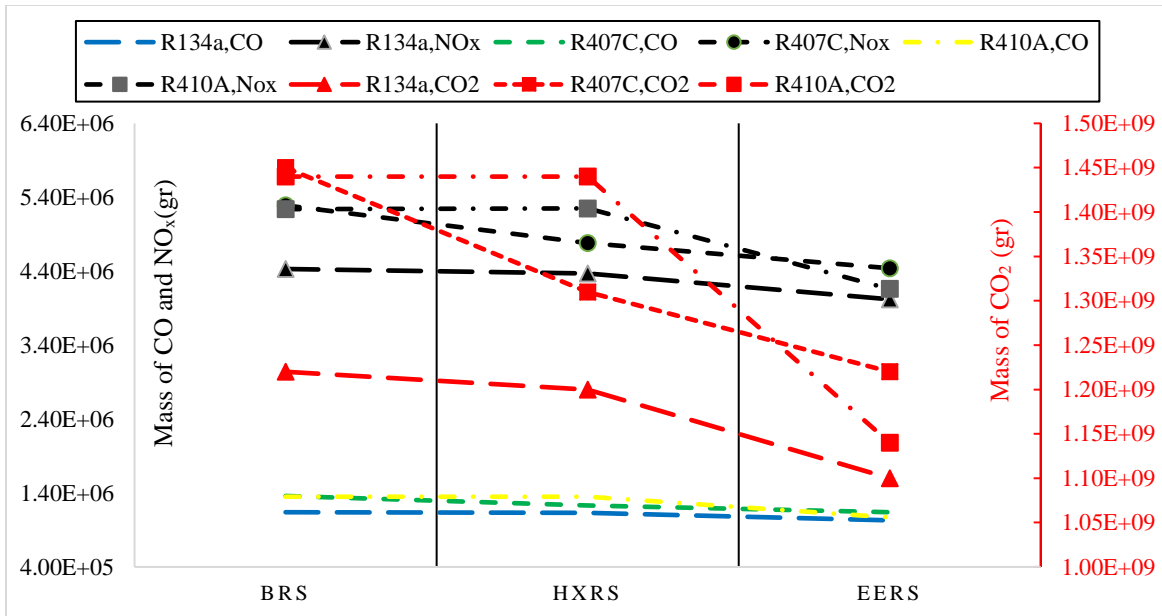
Fig. 4.18. Comparison of carbon monoxide, carbon dioxide and oxide of nitrogen that were produced by BRS, HXRS, and EERS with R134a, R407C, and R410A refrigerants.

4.2. Machine learning algorithms

4.2.1. Solar radiation prediction

There are a number of traditional methods for prediction of solar radiation that most of them are involve the statistical analysis of the data [167]. In addition, development of an empirical model using mathematical methods, such as least squares curve fitting or nonlinear regression. In dynamic systems, these models cannot predict the targets with high accuracy. Hence, authors proposed machine learning algorithms to predict hourly solar irradiance. For prediction of solar radiation two networks were proposed, which are described as follows.

For N_1:

In this network, pressure, temperature, relative humidity, wind speed and local time are used as inputs of the network and the MLFFNN, RBFNN, SVR, and FIS models are applied to predict the solar radiation for the study zone. The networks use data that have been provided by NASA [25]. The proposed models are trained with the hourly data collections. During data training, a smaller error between the outputs and targets can be found. When the new data are interred into the neural network, it can be achieved high error in outputs that this situation is called overfitting. In this study, some methods are applied to avoid overfitting problem. These methods are:

1. Divided the data into two sections: the train data and test data. In this method, the error between the outputs and targets is evaluated for two sets of data.

2. The second method to avoid overfitting is using automated regularization. The basic idea of the Bayesian framework procedure is first to create random values and then to add them to weights and biases. In this way, Bayesian regularization provides a variance that is distributed between random values. This concept is implemented in *trainbr* algorithm in Matlab software.

3. MSE can be modified to avoid overfitting problem. This statistical parameter relies on changing a certain factor to the MSE that contains a sum square error of the weight and biases.

4. It is noteworthy that SVR model has a regularization parameter, which makes the user think about avoiding overfitting problem.

For N_2:

In this network, proposed models use the past values of hourly solar radiation to estimate the future values. The MLFFNN, SVR, FIS, ANFIS-FCM, ANFIS-GP and ANFIS-SC are designed in order to predict the targets.

MLFFNN model:

A three layer feed-forward neural network was used to predict the targets in this study. The network was trained with six different data training algorithms that are LM, BFG, RP, SCG, CGP and BR (are shown in Table 4.5). Several tests using a different number of neurons in the hidden layer were performed. Finding the number of neurons in the hidden layer and type of data training algorithm can help to obtain the maximum performance for the developed model. The best performance was obtained with 150 neurons in the hidden layer. Also, the results show that LM has the best performance for predicting the targets with the highest correlation coefficient as 0.9887, lowest RMSE as 41.0876 (Wh/m^2) and lowest MSE as1688.188 (Wh/m^2) for the test data *(these performance evaluation measures are described in Appendix B)*. As can be seen in Table 1, BR, SCG and RP illustrate a satisfactory output with a correlation coefficient close to 0.98. Also, BFG has the maximum computation time and number of iterations with the low performance of this network (N_1).

Table 4.5. Comparison of the different data training algorithms in MLFFNN (N_1).

	Algorithm	RMSE (Wh/m^2)		R		Computation time	Epoch	MSE (Wh/m^2)	
		train	test	train	test			train	test
LM	trainlm	20.2989	41.0876	0.9968	0.9887	0:00:01	19	412.0455	1688.188
BFG	trainbfg	104.4125	129.8327	0.9122	0.8696	0:01:34	2000	10901.964	16856.518
RP	trainrp	48.7892	59.5264	0.9829	0.9652	0:00:01	182	2380.385	3543.394
SCG	trainscg	39.0337	69.3104	0.9878	0.9670	0:00:03	227	1523.6318	4803.928
CGP	traincgp	59.2158	76.1573	0.97299	0.9586	0:00:04	147	3506.513	5799.929
BR	trainbr	41.453	46.6413	0.98711	0.9819	0:00:09	33	1718.352	2175.407

Table 4.6 shows the time-series prediction of the solar irradiance (N_2) for the MLFFNN in the case study zone. The best performance was obtained with 70 neurons in the hidden layer. Six data training algorithms were applied to estimate the targets. LM and BR have the best performance respectively with R=0.9526 and 0.9570 for the test data.

Table 4.6. Different data training algorithms in MLFFNN (N_2) to predict solar irradiance.

	Algorithm	RMSE (Wh/m^2)		R		Computation time	Epoch	MSE (Wh/m^2)	
		train	test	train	test			train	test
LM	trainlm	52.2695	80.4823	0.9787	0.9526	0:00:01	18	2732.097	6477.3995
BFG	trainbfg	69.1641	87.1539	0.9632	0.9431	0:01:27	2000	4783.67	87.1539
RP	trainrp	64.7522	85.0304	0.9677	0.9429	0:00:00	99	4192.850	7230.174
SCG	trainscg	65.0755	80.9183	0.9674	0.9485	0:00:00	65	4234.825	6547.776
CGP	traincgp	78.9906	96.1576	0.9525	0.9302	0:00:00	41	6239.518	9246.273
BR	trainbr	67.4387	73.8315	0.9649	0.9570	0:00:02	41	4547.978	5451.097

RBF model:

Another type of neural network that has been applied to predict the solar radiation is RBF. This network adds neurons to the hidden layer until it achieves the goal (specific MSE). The main user-determined parameters in this network are spread of radial basis functions and the maximum number of neurons. The results of the proposed RBF model is shown in Table 3. The maximum number of neurons was determined 400 neurons and the amount of the R, RMSE and MSE for different spread of the model are given in Table 4.7. The large spread shows the smoother the function approximation. Too small a spread illustrates that the network needs many neurons to fit a smooth function and the network might not generalize well. Too large a spread means that the network needs a lot of neurons to fit a fast-changing function. In this investigation, the network was trained with 70% of the data and 30% of data was used to test the network. The results show that the network with the spread to be 6 has the best performance that for test data R=0.88011 and RMSE=150.1416 (Wh/m^2).

Table 4.7. RBFNN with different spread parameter for finding the best performance.

	RMSE (Wh/m^2)		R		MSE (Wh/m^2)	
Spread	train	test	train	test	train	test
3	57.715	205.438	0.9856	0.7179	3331.086	42204.912
4	60.037	163.747	0.9844	0.8195	3604.504	26813.365
5	63.857	161.446	0.9824	0.8432	4077.755	26065.027
6	67.189	150.141	0.9805	0.8801	4514.375	22542.507
7	69.378	171.432	0.9792	0.8733	4813.315	29389.247
8	71.321	159.967	0.9780	0.8699	5086.758	25589.632

SVR model:

The SVR model was proposed to predict the targets in this study. For this model, there are three user-determined parameters to obtain the best performance of the model. Parameters ε (is the error defined by the user), σ (is a predefined value which controls the width of the Gaussian function), and C (cost parameter C handles the trade-off between errors in the predictions (first term) and complexity (second term)) account for a significant effect on the SVR performance. As a result, in choosing user-defined parameters, a large number of trials were carried out with different combinations of C and σ. Fig. 4.19 illustrates different user-defined parameters for predicting the solar radiation in which the best performance was obtained in $\varepsilon=0.5$, $\sigma=1$, and $c=500$ with R=0.9999, RMSE=1.054 (Wh/m^2) and MSE=1.0262 (Wh/m^2).

Also, this model is applied to predict the time-series data of hourly solar radiation (N_2). To obtain the best performance of the model several iterations are done. Four models of the SVR technique are shown in Table 4.8 in which Model-4 (with R=0.9999, RMSE=3.026 (Wh/m^2) and MSE=9.1363 (Wh/m^2)) indicates the highest accuracy of the model. In addition, these model are shown in Fig. 4.20.

Table 4.8. Different aspect of designer-determined parameters for the proposed SVR.

Model		RMSE (Wh/m^2)	R	MSE (Wh/m^2)
1	$\varepsilon=0.5$, $\sigma=0.5$, $C=100$	276.185	0.6477	76278.28
2	$\varepsilon=1$, $\sigma=1$, $C=100$	166.554	0.8119	27740.23
3	$\varepsilon=0.5$, $\sigma=1$, $C=500$	14.1872	0.9987	201.277
4	$\varepsilon=0.5$, $\sigma=1$, $C=1000$	3.026	0.9999	9.1363
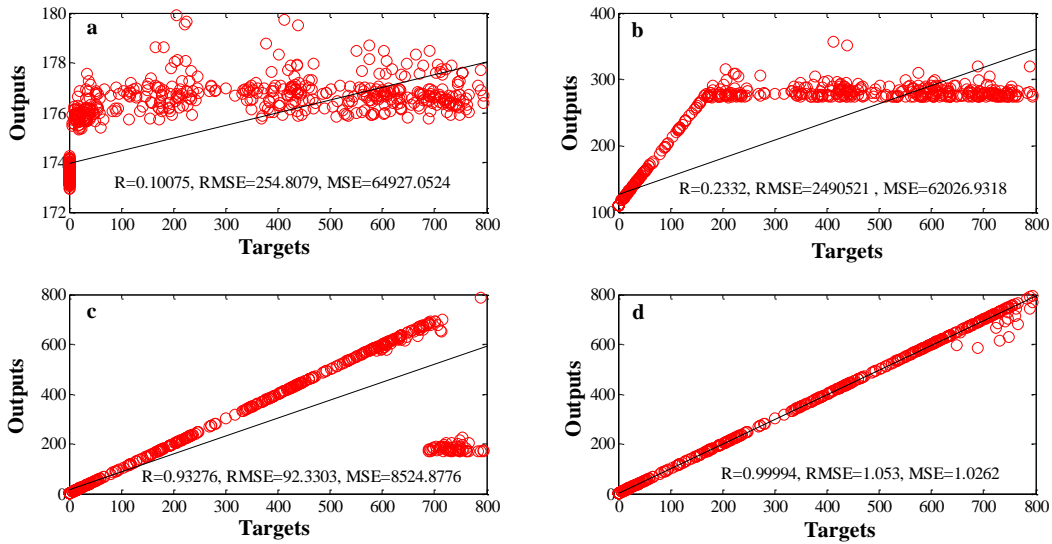
Fig. 4.19. The SVR model for predicting the target with ε=1, σ=1, *C*=1 (a), ε=1, σ=1, *C*=100 (b), ε=1, σ=0.5, *C*=500 (c), and ε=0.5, σ=1, *C*=500 (d).
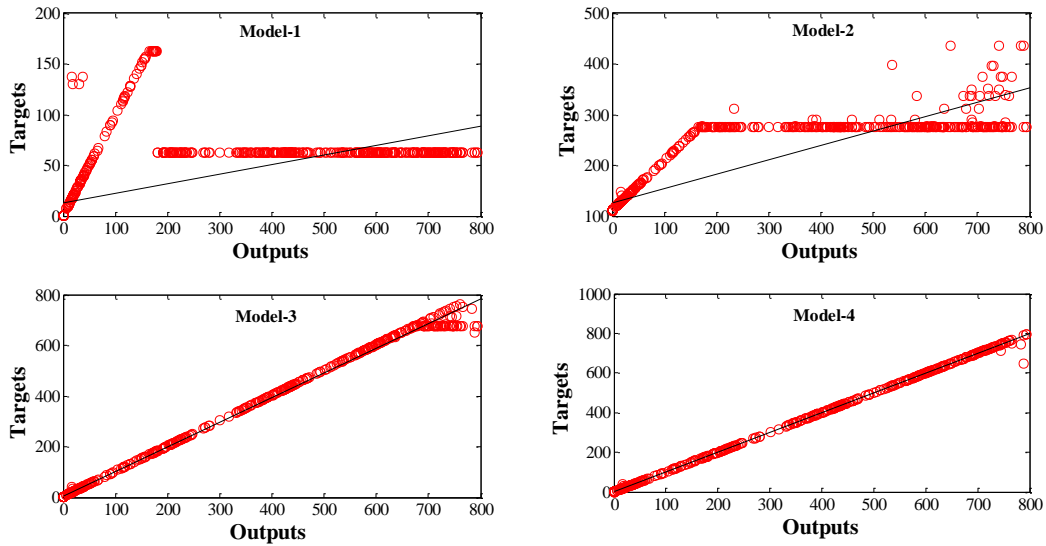
Fig. 4.20. The SVR model to predict the time-series hourly solar radiation (N$_2$) (based on Table 4.8).

FIS model:

Forecasting model based the FIS was proposed to predict the solar irradiance. The data were divided into two sections as 70% for the network training and 30% for the test data. At first, the number of fuzzy rules in order to obtain the maximum performance was determined. Fig. 4.21 shows the best performance of the model by considering the four MFs as inputs and target [$\underbrace{4\,4\,4\,4}_{Inputs}$ $\underbrace{4}_{Targets}$]. For this model, MFs were determined as *gaussmf* for the inputs and output and the Mamdani model as FIS structure. Gaussian MF is popular method for specifying fuzzy sets. Selecting the type of MF and its number is mostly dependent on the application and problem. The number of MFs are obtained through a trial and error process. In addition, for N$_2$ the train and test data are shown in Fig. 4.22 in which R values

for the N_2 (train: 0.96207 and test: 0.94683) are greater than N_1 (train: 0.92955 and test: 0.8787) and this model for the time-series prediction has the better performance.
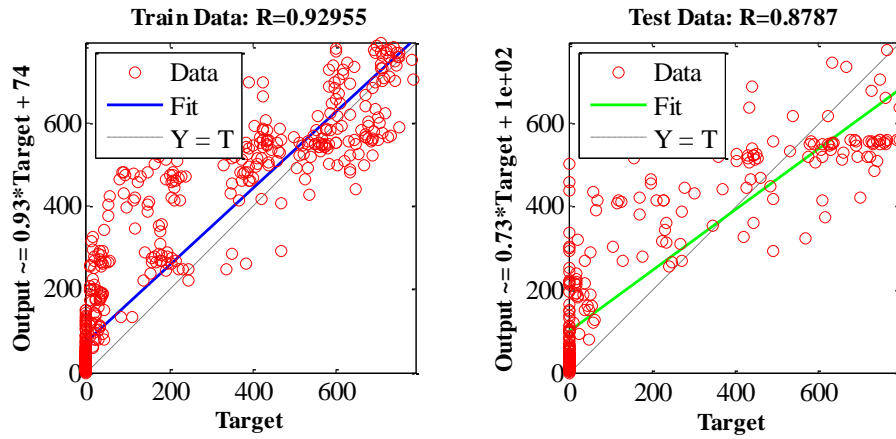
Fig. 4.21. Train and test data for the FIS in N_1.
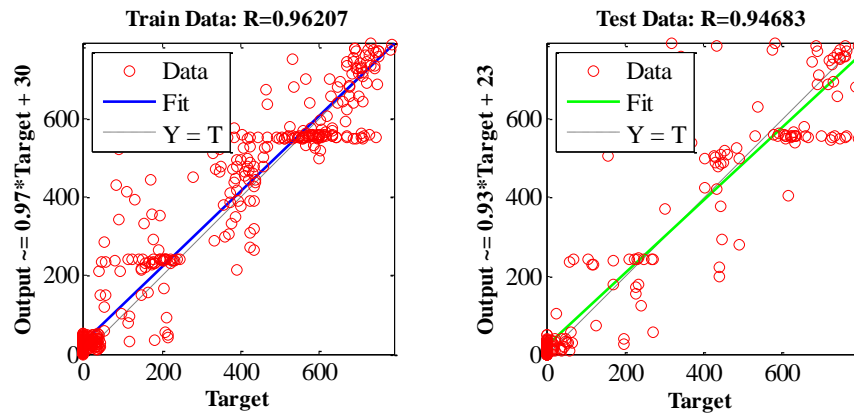
Fig. 4.22. Train and test data for the FIS in N_2.

Fig. 4.23 indicates the FIS decision surface for two inputs (x1: local time (hour) and x2: temperature (K)) and target (y: solar irradiance (Wh/m^2)). According to the decision surface, one can see the variation of local time has the maximum effect to predict the hourly solar irradiance.
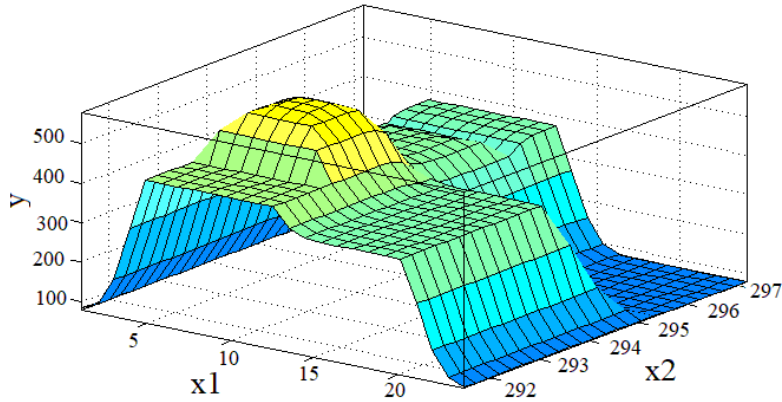
Fig. 4.23. FIS decision surface for the solar radiation prediction, x1: local time (hour), x2: temperature (K), y: solar irradiance (Wh/m^2).

ANFIS model:

Three types of the ANFIS model were developed to predict the time-series solar irradiance (N$_2$). The first one is ANFIS-FCM that uses fuzzy c-means clustering to determine the number of rules and MFs for the antecedents and consequents. For finding the optimum performance three different ANFIS-FCM were evaluated that are shown in Table 5. This table represents the results of this investigation in which was used from R and RMSE for evaluating the outputs (for train and test data). ANFIS-FCM (2) has the best performance with 10 clusters and partition matrix exponent=2, (this parameter controls the amount of fuzzy overlap between clusters that larger values demonstrate a greater degree of overlap). Also, the input and output MFs are *gaussmf* and *linear* respectively. Fig. 4.24 illustrates the structure of the ANFIS-FCM (2) with four inputs and one output. Ten clusters were generated for each input with 10 rules.
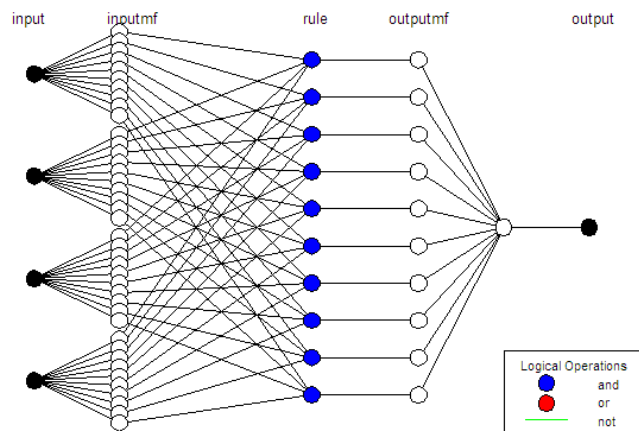
Fig. 4.24. Structure of the ANFIS-FCM (2).

The second one is ANFIS-SC that uses subtractive clustering to generate a Sugeno-type FIS structure. The main parameter for designing this model is the influence radius (radii) which is a vector that specifies a cluster center's range of influence in each of the data dimensions. This model was used to predict the target with different radii that

67

Table 4.9 shows ANFIS-SC (3) has the maximum performance. The third one is ANFIS-GP that uses grid partition on the data for generating a single-output Sugeno-type FIS. Input MF type is *gaussmf* and the output MF type is *linear* for this model. Also, the model evaluated with different number of MFs that are shown in Table 4.9. The values of correlation coefficient and RMSE for this model show the ANFIS-GP (3) with 4 MFs has the maximum correlation coefficient as 0.9493 and minimum RMSE as 86.1513 (Wh/m^2) for the test data. The maximum performance for the current investigation in ANFIS-GP model is obtained with the higher MFs (as can be seen in Table 4.9).

Table 4.9. Different types of ANFIS methods.

			RMSE		R	
FCM	Number of clusters	Partition Matrix Exponent	Train	Test	Train	Test
FCM(1)	5	2	59.7021	88.719	0.9715	0.94613
FCM(2)	10	2	56.671	83.1365	0.97436	0.95279
FCM(3)	20	4	53.1077	86.8542	0.97752	0.94777
Sub-Clustering	Influence Radius					
Sub-Clustering (1)	0.1		56.0014	10398.3099	0.97497	0.19884
Sub-Clustering (2)	0.2		53.0843	88.8146	0.97754	0.94497
Sub-Clustering (3)	0.4		56.0832	84.8125	0.9749	0.94956
Grid-Part	Number of MFs					
Grid-Part(1)	2		58.1909	86.3136	0.97295	0.9483
Grid-Part(2)	3		54.4955	88.3549	0.97632	0.94535
Grid-Part(3)	4		50.0626	86.1513	0.98005	0.94938

Comparison of the developed models:

Fig. 4.25 demonstrates a comparison between the developed models to predict the solar radiation (N_1). This graph shows the correlations between the targets and outputs for all data. The SVR model has the best performance to forecast the hourly solar irradiance with the correlation coefficient as 0.99839 for all data. Also, the MLFFNN reports the satisfactory outputs with the R=0.98481 and RMSE=44.5356 (Wh/m^2). The RBFNN illustrates an acceptance correlation between the outputs and targets in the training stage but the test data have lower performance as compared to the training stage. In addition, FIS model can predict the targets with the correlation coefficient of 0.8787 and RMSE of 171.256 (Wh/m^2).

Fig. 4.26 shows the correlation between targets and outputs for time-series prediction of solar irradiance (N_2) with different proposed models. Although all the developed models can successfully predict the targets with approximately above 0.95% accuracy, SVR has the best performance between the all developed models with R=0.9999, and RMSE=3.0266 (Wh/m^2).
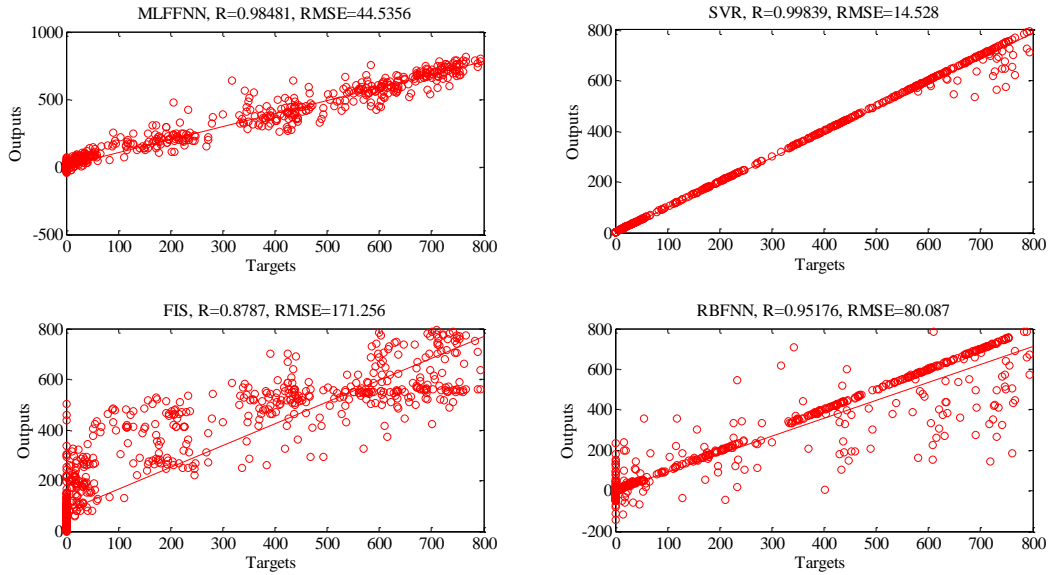
Fig. 4.25. Comparison of the forecasting model in N_1.
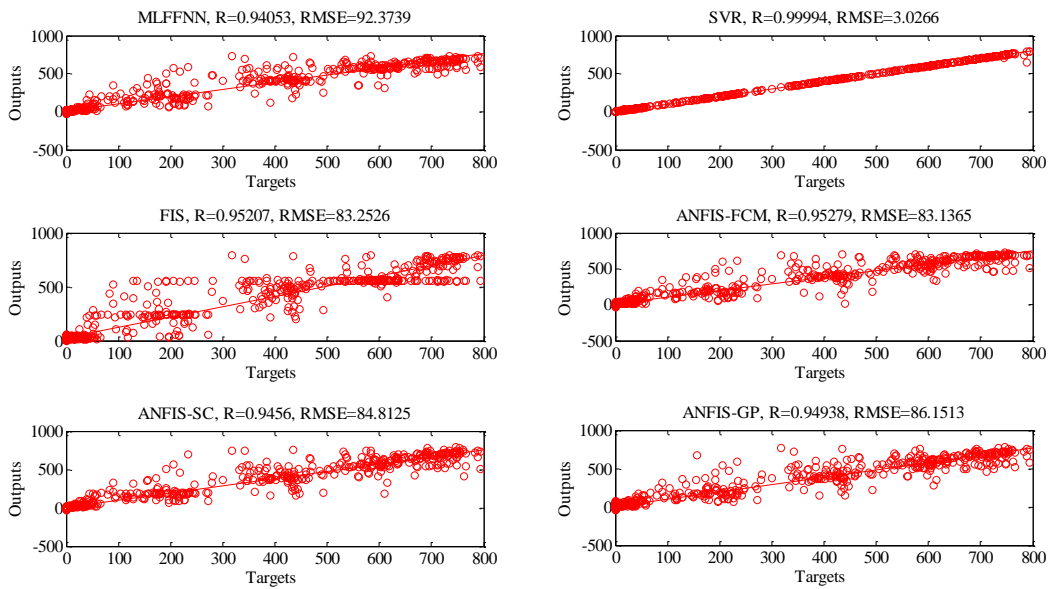
Fig. 4.26. Time series prediction of different proposed models.

The developed models were applied to estimate the solar irradiance in the case study region for 72 hours and the outputs are shown in Fig. 4.27 (for N_1). As before mentioned the SVR model has the best performance for forecasting the targets and also it can be seen that the other developed models have reported acceptance outputs. Also, Fig. 4.28 indicates the solar irradiance prediction based time-series data (N_2) for the future 24 hours in the study zone. The outputs are very close to each other but for this prediction FIS and SVR have the better performance.
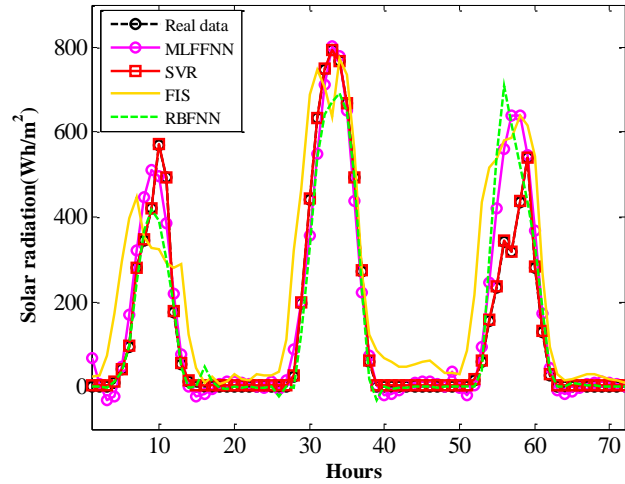
Fig. 4.27. Prediction of solar irradiance for 72 hours (N_1).
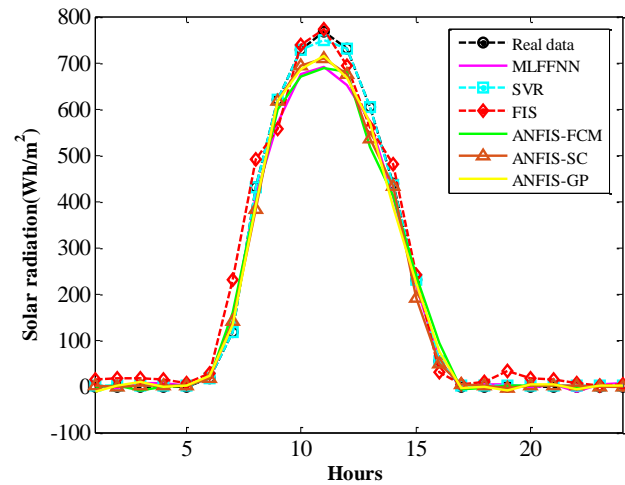
Fig. 4.28. Prediction of solar irradiance for 24 hours (N_2).

Table 4.10 demonstrates the correlation coefficient for some different proposed models in order to estimate solar irradiance from literature studies. Hourly solar radiation prediction is a dynamic system and statistical models cannot estimate the targets with the high accuracy. As can be seen in Table 4.10, Chen et al. [168] reported approximately R=0.7 for statistical methods in order to forecast solar radiation. But other studies have shown that machine learning algorithms can predict this system with high efficiency. This article was shown that the developed models can predict the targets with the high performance. Olatomiwa et al. [169] developed an ANN with maximum accuracy (R=0.9551) to predict the solar radiation, but this study obtained an ANN with R=0.9887 in the test data. Also developed SVR model reported a performance higher than Ramedani et al. [170] model.

Table 4.10. Performance of the different proposed models for predicting solar irradiance from literature review.

	Model	R		Model	R
Chen et al. [168]	Statistical method	0.7	Quej et al. [171]	SVM	0.8209
	Fuzzy algorithm	0.8613		ANFIS	0.8024
	Neural network	0.8915		ANN	0.8012
Olatomiwa et al. [172]	SVM-Firefly Algorithm	0.8918	Ibrahim et al. [9]	ANN	0.828413
	ANN	0.8635		ANN-FFA	0.8699
	Genetic Programming	0.7895		Random forests	0.7947
Ramedani et al. [170]	ANN	0.8938	Bou-Rabee et al. [173]	ANN	85.6
	ANFIS	0.8949	Gupta et al. [169]	ANN	0.9551
	SVR-RBF	0.8888	Bakirci [174]	Empirical	0.8831

4.2.2. Wind speed prediction

Wind power generation depends on wind speed, thus, wind speed prediction becomes increasingly important for modern wind farm management and supply-demand balancing in the smart grid. However, wind speed is generally very difficult to estimate, due to its non-stationary and intermittent nature. There are a number of traditional methods for prediction of wind speed that most of them are involve the statistical analysis of the data. In dynamic systems, these models cannot predict the targets with high accuracy. Hence, authors proposed machine learning algorithms to predict the targets in these dynamic systems. The network was developed with temperature, pressure, local time and relative humidity as input variables and the targets are wind speed, wind direction and output power of a WT. To evaluate the performance of the models three statistical parameters that are root mean square error (RMSE), correlation coefficient (R) and mean square error (MSE) are used. These parameters are described in *Appendix A*. During data training, a smaller error between the outputs and targets can be found. When the new data are interred to the neural network, it can be achieved high error in outputs that this situation is called overfitting. In this study to avoid overfitting problem, the data were divided into two sections as 70% training datasets and 30% as testing datasets.

MLFFNN model:

ANN is a promising method for adaptive the prediction of targets. Table 4.11 illustrates prediction of the wind speed and its direction using MLFFNN. To obtain the best performance nine data training algorithms were applied. The results show in January for 10-min interval data, BR and LM algorithms have the maximum R and minimum RMSE and MSE. But the computation time and number of iteration for LM are lower than BR algorithm. Also, BFG algorithm reports an accuracy above 96%. RP and SCG algorithms are faster than others training algorithms. It is observed that prediction wind direction is harder than wind speed for the network. The designed network needs much the computation time to predict the wind direction. Fig. 4.29 demonstrates the training phase of the model to predict wind speed for 24 hours. Moreover, for prediction of wind direction the training phase of the model with different data training algorithms are shown in Fig. 4.30. Both figures illustrate that LM and BR can successfully train the models. Reaching good forecasting accuracy for MLFFNN also depends on the suitable number of neurons in the hidden layer. The smallest errors of statistical indices were obtained for 75 neurons in the hidden layer for wind speed prediction and 175 neurons for wind direction forecasting model.

Table 4.11. Prediction of the wind speed and its direction using MLFFNN.

	Algorithm	RMSE(m/s)	R	Computation time	Epoch	MSE(m/s)
Wind speed prediction for January with 10-min interval						
LM	trainlm	0.3226	0.9828	0:02:03	423	0.1041
BFG	trainbfg	0.4689	0.9634	0:00:41	342	0.2199
RP	trainrp	0.7169	0.9124	0:00:07	361	0.5140
SCG	trainscg	0.8361	0.8786	0:00:04	115	0.6991
CGB	traincgb	0.7705	0.8980	0:00:10	132	0.5937
CGF	traincgf	0.7634	0.8999	0:00:16	202	0.5828
CGP	traincgp	0.7888	0.8930	0:00:13	163	0.6212
OSS	trainoss	0.7730	0.8973	0:00:17	191	0.5976
BR	trainbr	0.2958	0.9856	0:05:13	1059	0.0875

	Algorithm	RMSE(°)	R	Computation time	Epoch	MSE(°)
Wind direction prediction for January with 10-min interval						
LM	trainlm	25.954	0.9791	0:02:39	214	673.644
BFG	trainbfg	69.372	0.8397	0:50:34	10000	4812.477
RP	trainrp	66.087	0.8557	0:00:18	459	4367.534
SCG	trainscg	65.027	0.8595	0:00:24	322	4260.725
CGB	traincgb	72.749	0.8218	0:00:24	142	5292.431
CGF	traincgf	76.359	0.8015	0:00:24	139	5830.768
CGP	traincgp	72.556	0.8229	0:00:34	199	5264.469
OSS	trainoss	80.573	0.7759	0:00:48	153	6492.079
BR	trainbr	30.306	0.9714	0:06:28	488	918.468
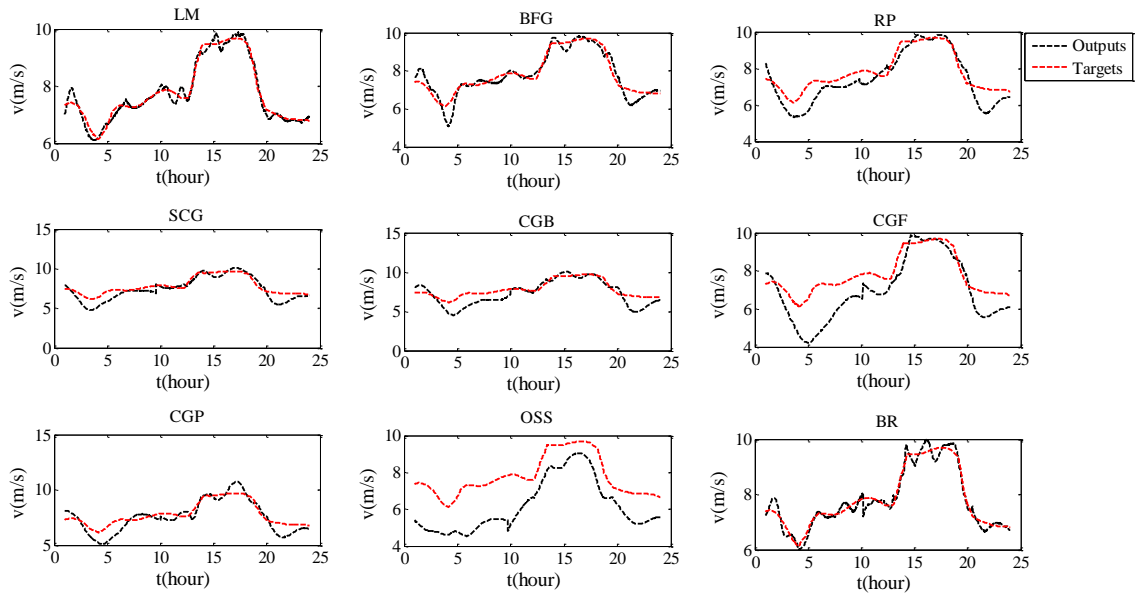
Fig. 4.29. Comparison of the different training algorithms for wind speed prediction for MLFFNN.
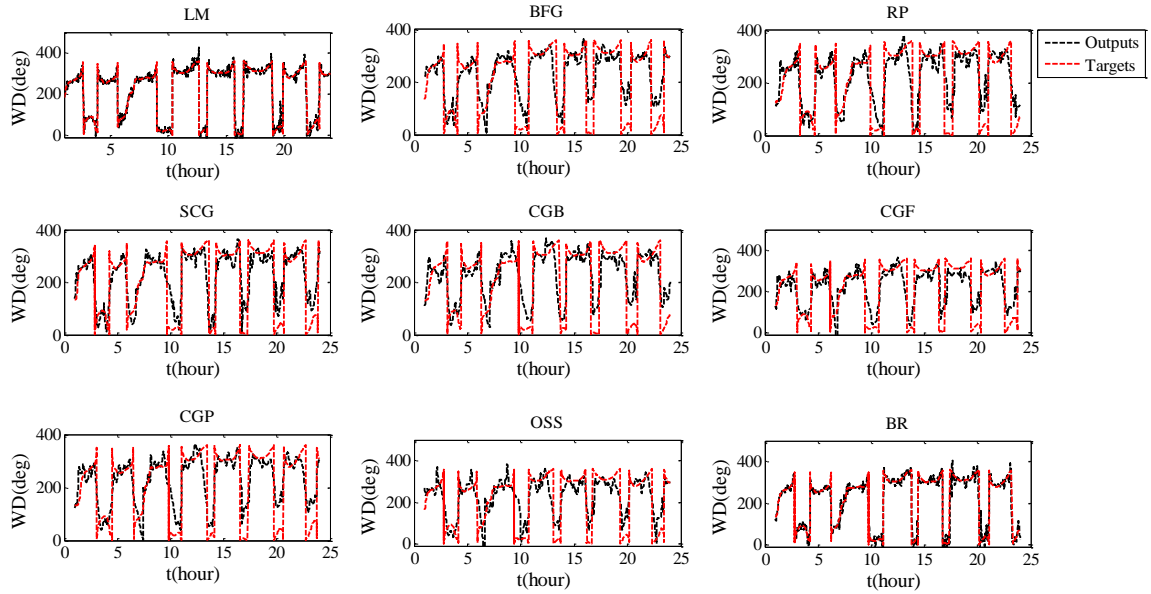
Fig. 4.30. Comparison of training algorithms for prediction of wind direction for MLFFNN.

Figure 4.31 illustrates the testing phase of wind speed prediction for 24 hours of January. This graph shows that the overfitting problem has considered for designing the network and the results with new data have an approximately similar trend with the data training process. For this prediction, LM, BFG and BR show satisfactory predicted wind speed data.
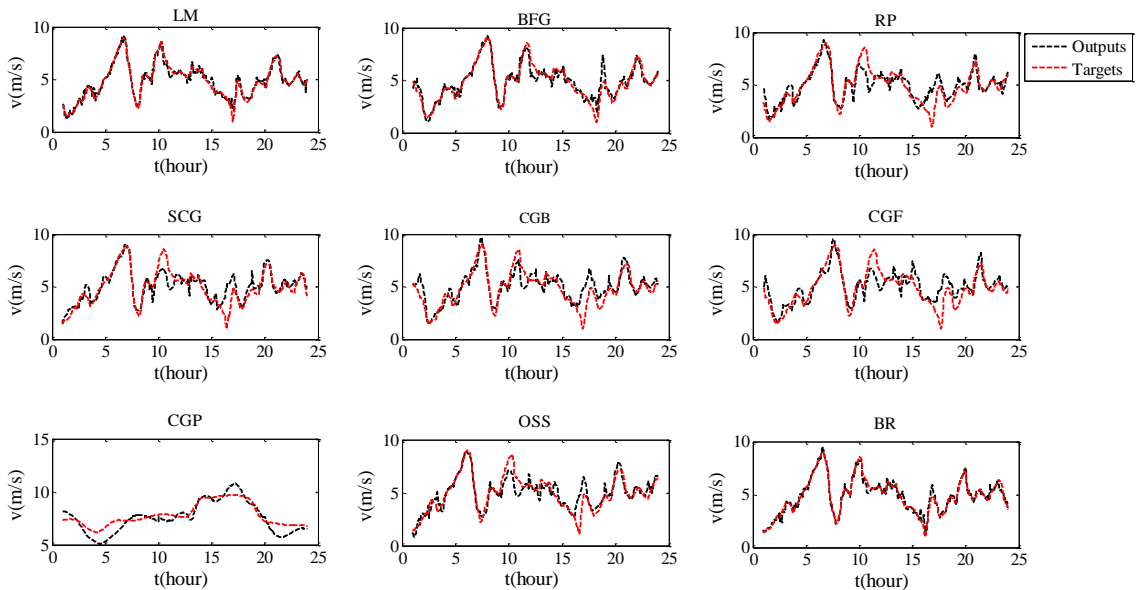
Fig. 4.31. Test data of MLFFNN for 24 hours.

SVR-RBF model:

Support vector regression was developed to predict the targets. This model was implemented based on RBF as a kernel function. Hence, this model was called SVR-RBF. This model was adjusted with three user-defined parameters. These parameters are ε (is the error defined by the user), σ (is a predefined value which controls the

width of the Gaussian function) and *C* (cost parameter *C* handles the trade-off between errors in the predictions (first term) and complexity (second term)). Different values of these parameters are reported in Table 4.12. The best performance of the model was achieved for Model-4 of SVR in terms of RMSE=0.0184 (m/s), R=0.9999 and MSE=0.0003 (m/s).

Table 4.12. Design parameters of SVR-RBF for wind speed forecasting (10-min interval)

Model		RMSE (m/s)	R	MSE (m/s)
1	$\varepsilon=1$, $\sigma=1$, $C=1$	0.8647	0.9286	0.7478
2	$\varepsilon=0.5$, $\sigma=1$, $C=100$	0.4504	0.9811	0.0202
3	$\varepsilon=0.02$, $\sigma=1$, $C=1000$	0.0191	0.9999	0.0003
4	$\varepsilon=0.02$, $\sigma=0.5$, $C=1000$	0.0184	0.9999	0.0003

Also, Fig. 4.32 demonstrates the prediction of wind direction in six different values of user-determined parameters. The performance of the model with different values of ε, σ and *C* is shown in this graph in which Fig. 4.32 (f) shows the best performance by $\varepsilon=0.5$, $\sigma=1$ and $C=1000$.
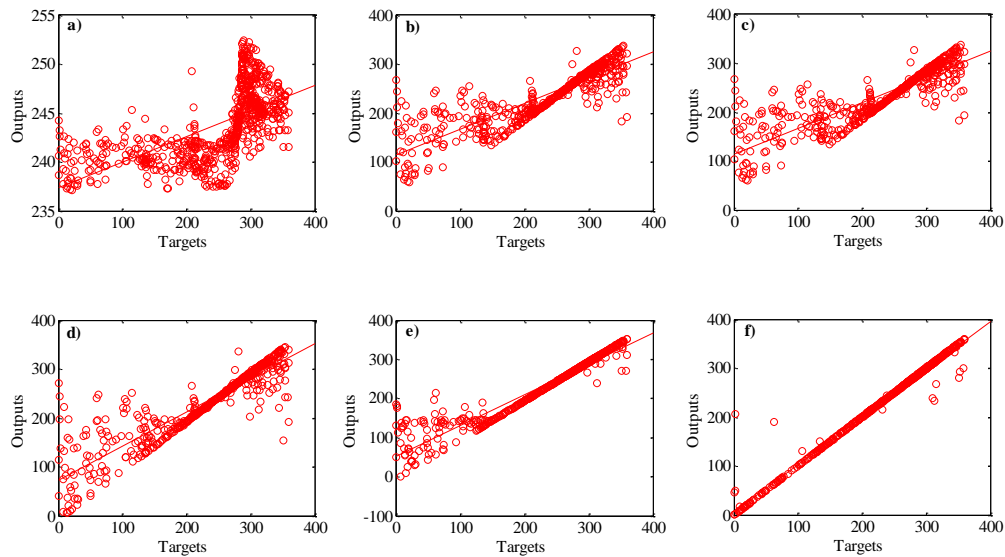
Fig. 4.32. SVR-RBF with different user-determined parameters: (a), $\varepsilon=1$, $\sigma=1$, $C=1$, (b), $\varepsilon=1$, $\sigma=1$, $C=30$, (c), $\varepsilon=0.5$, $\sigma=1$, $C=30$, (d), $\varepsilon=0.5$, $\sigma=1$, $C=50$, (e), $\varepsilon=0.02$, $\sigma=0.5$, $C=100$, (f), $\varepsilon=0.5$, $\sigma=1$, $C=1000$.

ANFIS-PSO model:

The developed ANFIS model is called ANFIS-FCM that uses fuzzy c-means clustering to generate a fuzzy inference system. Obtaining good accuracy using ANFIS can be achieved by adjusting the suitable number of clusters for the model. It depends on the number of data that are considered for training model. A large number of trials were done to obtain the suitable number of clusters for the model. Finally, the model was developed with 300 clusters in which the maximum accuracy for the model obtained. Generally, for this specific problem, as can be seen in Table 4.13, the ANFIS model cannot predict the target with high accuracy. Hence, a PSO algorithm was considered to optimize the ANFIS parameters. The PSO parameters were selected as follows: the size of

population is 200, the maximum iteration is 1500, $C_1 = 1$ (personal learning coefficient), $C_2 = 2$ (global learning coefficient) and Inertia weight was considered as 1. The correlation coefficient, which indicates the goodness of fit of the model, for the ANFIS model is reported to be 0.8991 and 0.8995 for the training and testing datasets, respectively. The PSO algorithm can successfully improve the performance of the ANFIS model and the novel method outperforms the ANFIS model.

Table 4.13. A comparison between ANFIS and ANFIS-PSO models for 5-min interval of wind speed data.

	RMSE (m/s)		R		MSE (m/s)	
	Train	Test	Train	Test	Train	Test
ANFIS	0.8466	0.8420	0.8898	0.8888	0.7167	0.7090
ANFIS-PSO	0.1700	0.2321	0.9958	0.9922	0.0289	0.0538

Figure 4.33 demonstrates the prediction of wind speed with the ANFIS-PSO model agrees well with the target data and the magnitude of the disagreement between the actual and predicted data is small.
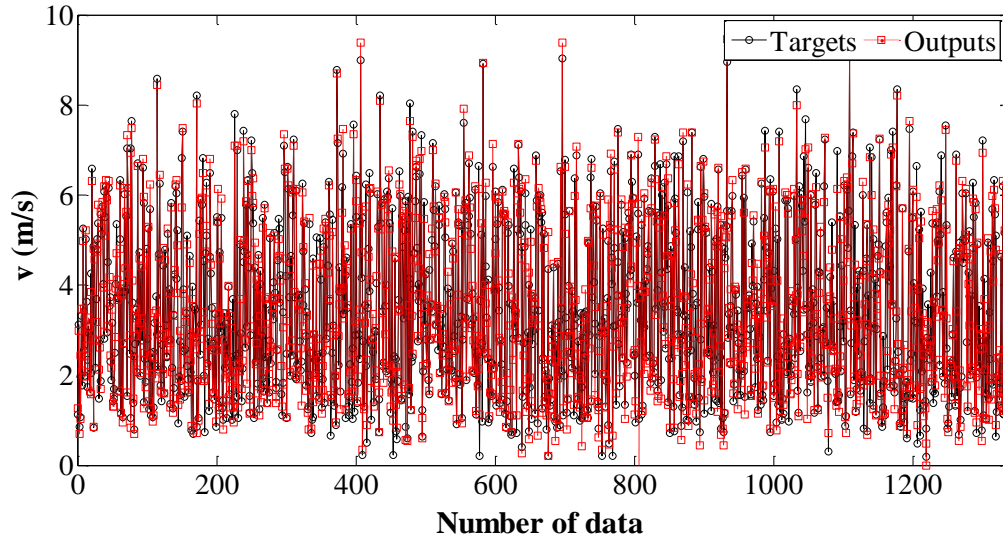
Fig. 4.33. Actual and predicted wind speed data for 10-min interval using ANFIS-PSO.

Models comparison:

The developed models were applied to predict the targets. Actually, we proposed a network with pressure, temperature, local time and relative humidity as inputs variables that can predict wind speed, wind direction and output power of the considered WT in the case study region. Four samples of datasets were considered to evaluate the proposed models. Wind speed data with 5-min interval (8,928 data), 10-min interval (4,464 data), 30-min interval (1,488) and 1-h interval (744 data) for June 2017 were selected for this investigation. Comparison of the models for RMSE, R and MSE values can be observed clearly in Table 4.14. The lowest statistical errors and the highest correlation coefficient were obtained with the SVR-RBF model for all time intervals. The obtained correlation coefficient of the MLFFNN and ANFIS-PSO models (for 5-min and 10-min intervals) illustrate the predicted wind speed (outputs) agrees well with the actual data (targets) and the magnitude of the disagreement

between the outputs and targets is small. For 30-min and 1-h intervals, the SVR-RBF outperforms the MLFFNN and ANFIS-PSO models in terms of RMSE, R and MSE. Moreover, the MLFFNN and ANFIS-PSO models approximately have the same ability to predict the wind speed data.

Table 4.14. A comparison between the developed models to predict wind speed data.

	RMSE(m/s)		R		MSE(m/s)	
	Train	Test	Train	Test	Train	Test
5-min interval						
MLFFNN	0.2143	0.2450	0.9933	0.99108	0.0459	0.0600
SVR-RBF	0.0206	0.0213	0.9999	0.9999	4.23E-04	4.53E-04
ANFIS-PSO	0.1700	0.2321	0.9958	0.9922	0.0289	0.0538
10-min interval						
MLFFNN	0.1373	0.2216	0.9972	0.9924	0.0189	0.0491
SVR-RBF	0.0439	0.0526	0.9997	0.9996	0.0019	0.0028
ANFIS-PSO	0.1819	0.3549	0.9951	0.9824	0.0331	0.1259
30-min interval						
MLFFNN	0.2053	0.7437	0.9940	0.9123	0.0421	0.5532
SVR-RBF	0.1800	0.1808	0.9951	0.9957	0.0324	0.0327
ANFIS-PSO	0.4566	0.7965	0.9686	0.9103	0.2085	0.6344
1-h interval						
MLFFNN	0.3589	0.9382	0.9831	0.8631	0.1288	0.8803
SVR-RBF	0.3669	0.3651	0.9824	0.9796	0.1346	0.1333
ANFIS-PSO	0.590	1.0312	0.9474	0.8534	0.3481	1.0634

Also, the performances of the MLFFNN, SVR-RBF and ANFIS-PSO models for wind direction forecasting are compared using a comprehensive wind direction samples. For the 5-min interval, the correlation coefficient is 0.9612 for MLFFNN and ANFIS-PSO and is 0.9918 for SVR-RBF. As expected, the SVR-RBF is more accurate than MLFFNN and ANFIS-PSO models. Generally, the developed models have lower performance for prediction of wind direction compared to wind speed forecasting. This investigation is shown in Table 4.15.

Table 4.15. A comparison between the developed models to predict wind direction data.

	RMSE(°)		R		MSE(°)	
5-min interval						
	Train	Test	Train	Test	Train	Test
MLFFNN	15.922	23.572	0.9822	0.9612	253.528	555.67
SVR-RBF	8.1018	14.2148	0.9945	0.9918	65.638	202.061
ANFIS-PSO	16.2761	23.7135	0.9817	0.9612	264.910	562.3316
10-min interval						
MLFFNN	20.498	29.110	0.9710	0.9373	420.204	847.441
SVR-RBF	23.306	25.907	0.9592	0.9379	640.394	671.173
ANFIS-PSO	22.7428	0.37068	0.9638	0.9074	517.2342	1374.0433
30-min interval						
MLFFNN	32.212	54.418	0.9243	0.8007	1037.616	2961.400
SVR-RBF	8.5732	8.4891	0.9955	0.9927	73.5002	72.0641
ANFIS-PSO	44.189	61.2601	0.8570	0.7201	1952.6645	3752.7941
1-h interval						
MLFFNN	33.459	69.933	0.9236	0.6284	1119.529	4890.751
SVR-RBF	13.9711	19.4433	0.9824	0.9765	195.1904	378.0410
ANFIS-PSO	40.255	87.9549	0.8784	0.5368	1620.4624	7736.056

4.3. Hybrid renewable energy system

Solar/wind energy potential:

Fig. 4.34 demonstrates the variation of the wind speed for the case study region in 2016. The hub center for the considered wind turbine (E-44) is 55 m. The average wind speed for this region measured at the hub center (measured by Duffie and Beckman [153] correlation) is around 7 m/s. Wind speed in the hub center is the main parameter to calculate the mechanical power of the rotor. Fig. 4.35 illustrates the average temperature for the study zone between 2000 and 2016. As can be observed in the figure, the average temperature for 6 months (from April to October) is above 28°C. This value of temperature shows that the energy efficiency for PV modules will be decreased in these months. Because the energy efficiency of PV modules is in relation to the ambient temperature (based on Eqs. (3.182) and (3.183)). Solar radiation on top of atmosphere (a) and over the collectors (b) from 2000 to 2016 are shown in Fig. 4.36. The maximum solar radiation on the PV collectors (horizontal) in May, June, July and August is approximately 8 kWh/m^2/day. The solar data were provided by NASA [25].
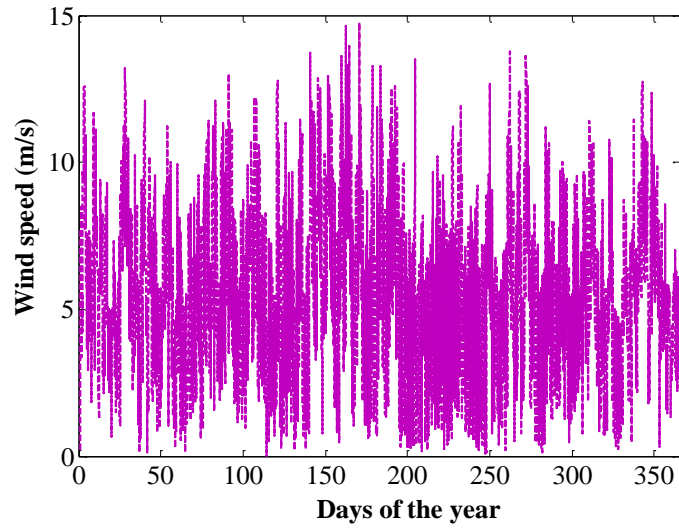
Fig. 4.34. Wind speed (m/s) for Bushehr in 2016.
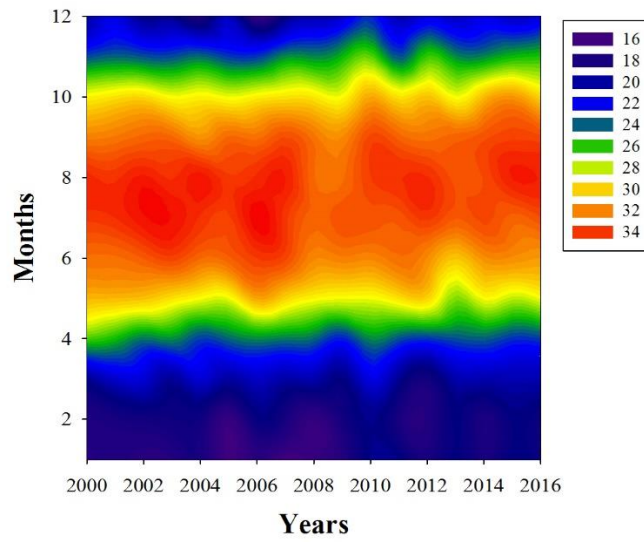
Fig. 4.35. Variation of the temperature (℃) between 2000 and 2016 in Bushehr.
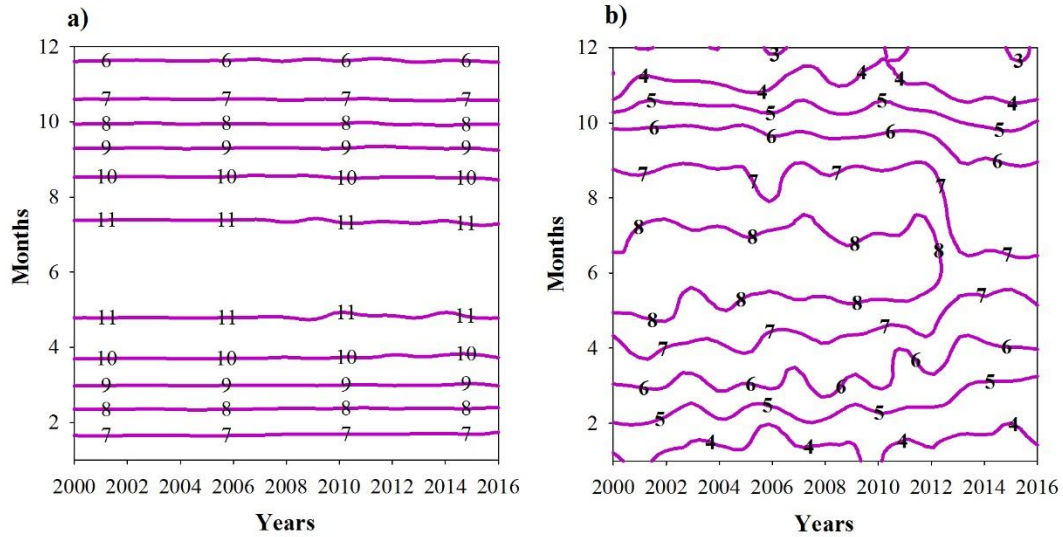
Fig. 4.36. Solar radiation on top of atmosphere (a) and on the collectors (b) based on kWh/m^2/day.

Sun tracker system due to having the moving part is more expensive compared to stationary collectors. Also, in this system ongoing maintenance is generally required. Hence, determining the optimum slope angle is important for receiving the more solar radiation on flat-plate collectors. The amount of the monthly tilt angle of the collectors for the study zone is shown in Fig. 4.37.
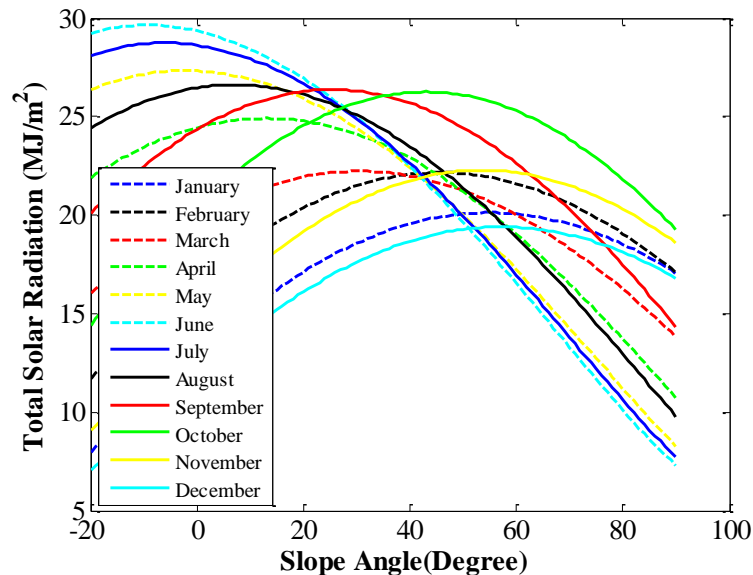
Fig. 4.37. Monthly optimum slope angle of solar collectors.

The effect of the monthly optimum slope angle for the solar collectors is reported in Fig. 4.38. The results show, with monthly optimum tilt angle, the amount of the solar radiation is increased about 20% for an annual period. But in March, April, May and June the values of the solar radiation with monthly slope angle is close to the values of horizontal collectors. In January and December, the amounts of the solar radiation with optimum slope angle is approximately 50% more than the horizontal collectors.
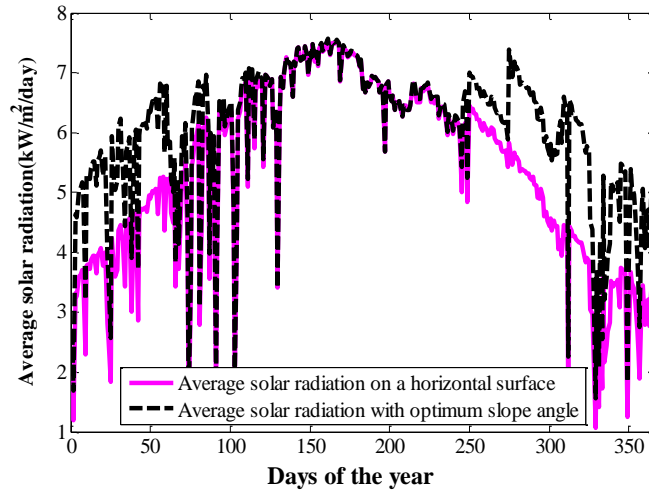
Fig. 4.38. Average solar radiation on the horizontal and tilted surfaces.

Liu and Jordan [175] proposed azimuth angle for the northern hemisphere and southern hemisphere to be 0° and 180°, respectively. In this investigation, the azimuth angle for the study region is determined to be 30° (is shown in Fig. 4.39). The proposed azimuth angle was calculated by using the yearly slope angle (regarding Eqs. (3.161)- (3.180)).
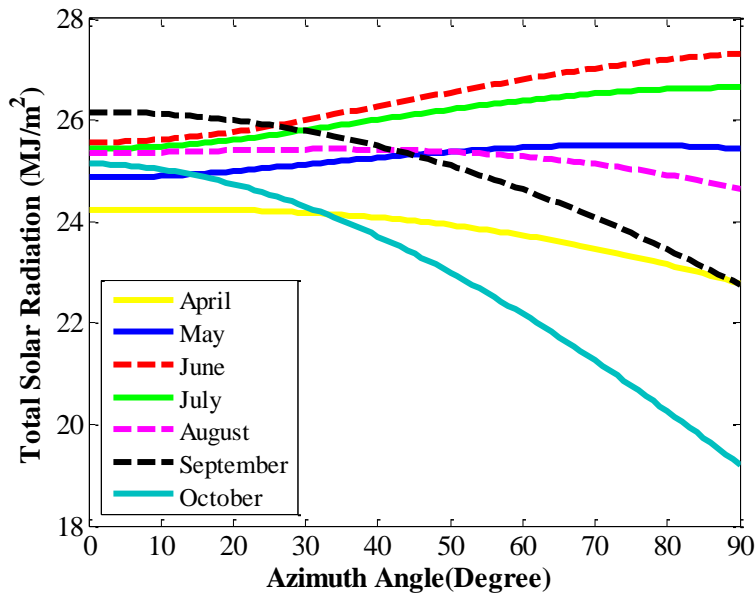
Fig. 4.39. Optimum azimuth angle for solar collectors in Bushehr.

Produced power:

The proposed system is a stand-alone system with all the energy coming from sun and wind. Fig. 4.40 shows the amount of the provided energy by the PV, WT and fuel cell systems for an annual period for the unit. According to the pie chart, PVS accounts for 43% of the total. A third of the required energy is provided by WTS. Also, the fuel cell by using the stored hydrogen supplies 26% of the total energy.
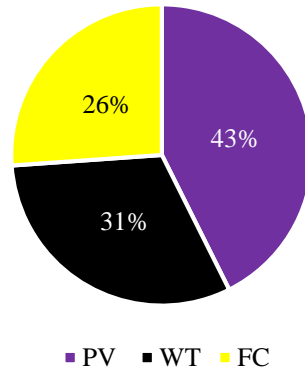
Fig. 4.40. Percentage of the provided energy by PVS, WTS and ful cell.

Fig. 4.41 demonstrates the curves of the power coefficient and electric power produced of the WT that have been obtained in the study region. As can be seen in Fig. 4.41 (a), from 0 to 2 m/s, the power coefficient is zero; from 2 to 7 m/s, it increases and reaches to the maximum value; between 7 and 14 m/s, there is a moderate decrease. Moreover, Fig. 4.41 (b) shows the curve of generated power versus the wind speed. Regarding the graph, between 0 and 4 m/s, cannot be seen an impressive produced power. Also, between 4 and 14 m/s, the trend is obviously upwards and reaches to around 700 kW.
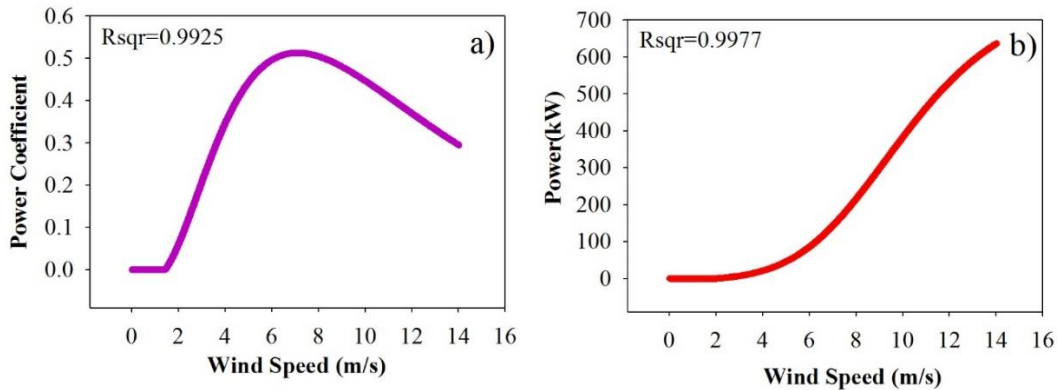
Fig. 4.41. Power coefficient (a) and electric power produced (kW) (b) versus wind speed (m/s) for the WT.

Fig. 4.42 represents a dynamic model of the generated power for an annual period for the PV and WT systems. Power produced by PVS (Fig. 4.42 (a)) for six months is more than 1000 kW from 6:00 to 14:00. The generated power decreases for June, July, August and September and reaches to 600 kW. Power generated by WTS (Fig. 4.42 (b)) has different values for each time series but the maximum power is shown in May, June and July for the study zone. Also, from 5:00 to 16:00 the obtained power of WTS is above 800 kW. Fig. 4.43 demonstrates the productive power of the PVS (a) and WTS (b) in 12, 13 and 14 of June 2016. WTS produces more power in these days. Average daily wind power that has been produced by WTS is almost 170 kW and this power for PVS is roughly 233 kW.

Fig. 4.44 shows the model of the stored power by the energy storage system for one year in the study zone. To provide the demand energy rate of the unit, the storage system is considered with the 50 MW at the start of the system. It is

clear that during January to May, the stored power rises gradually; between April and July, the stored power reaches to the maximum value that is approximately 280 MW; then from June to December, this power will be consumed. The amount of the stored power at the end of the period will be reached to the start point.
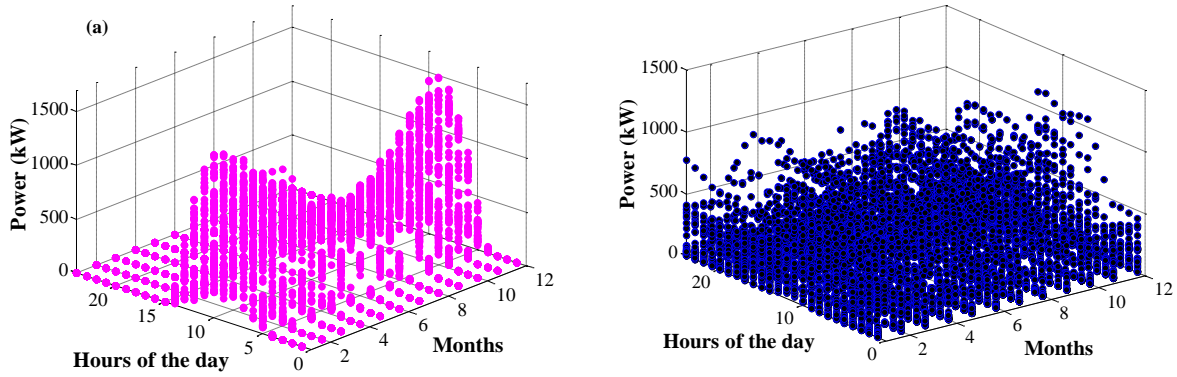
Fig. 4.42. Produced power by the PVS (a) and WTS (b).
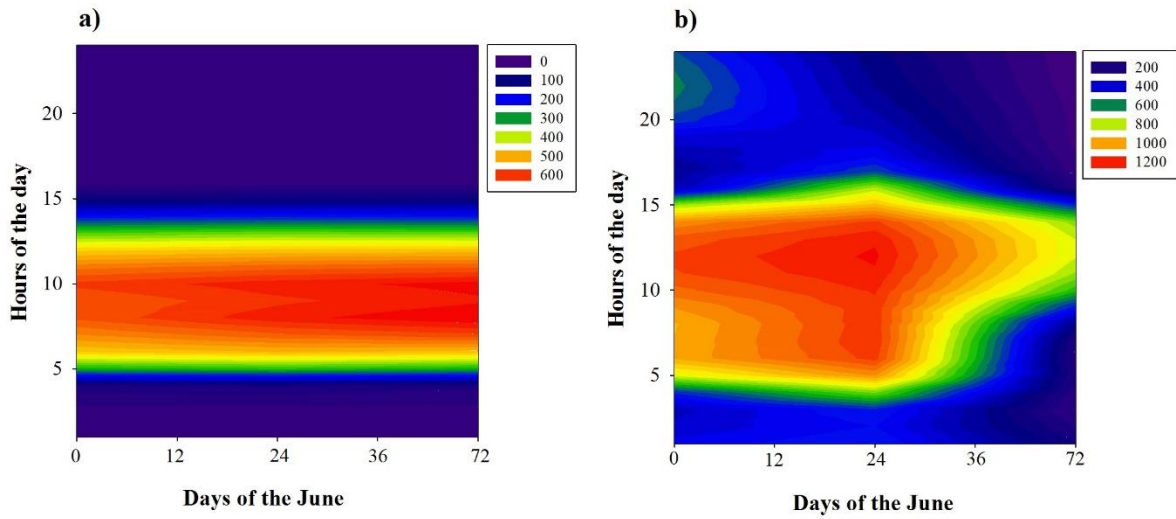
Fig. 4.43. Produced power (kW) by PVS (a) and WTS (b) for June 12th, 13th and 14th.
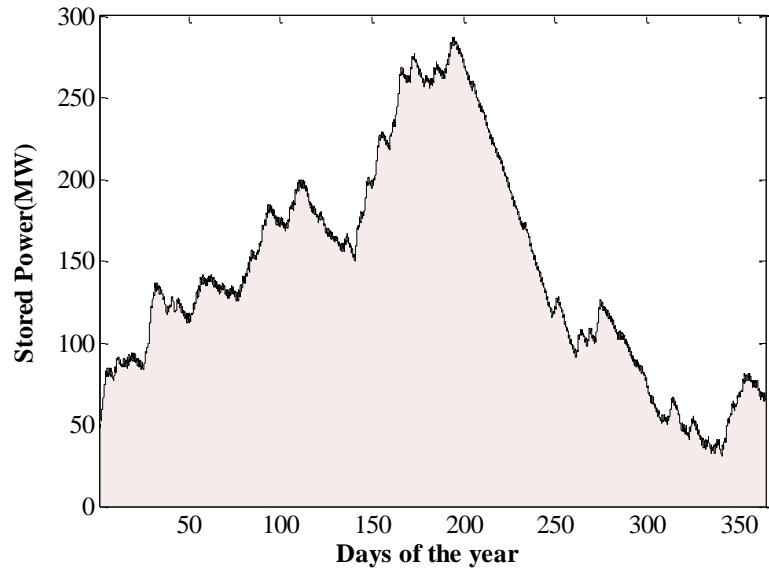
Fig. 4.44. Stored power and consumed power by the energy storage system.

Fig. 4.45 (a) illustrates the excess power that was transferred to the electrolyzer for one year. This excess power can be used to produce the hydrogen in the electrolyzer. Between 5:00 and 15:00 the required energy rate is provided by the PVS and WTS. Fig. 4.45 (b) exhibits all the times that the required energy rate of the unit is provided by the fuel cell.
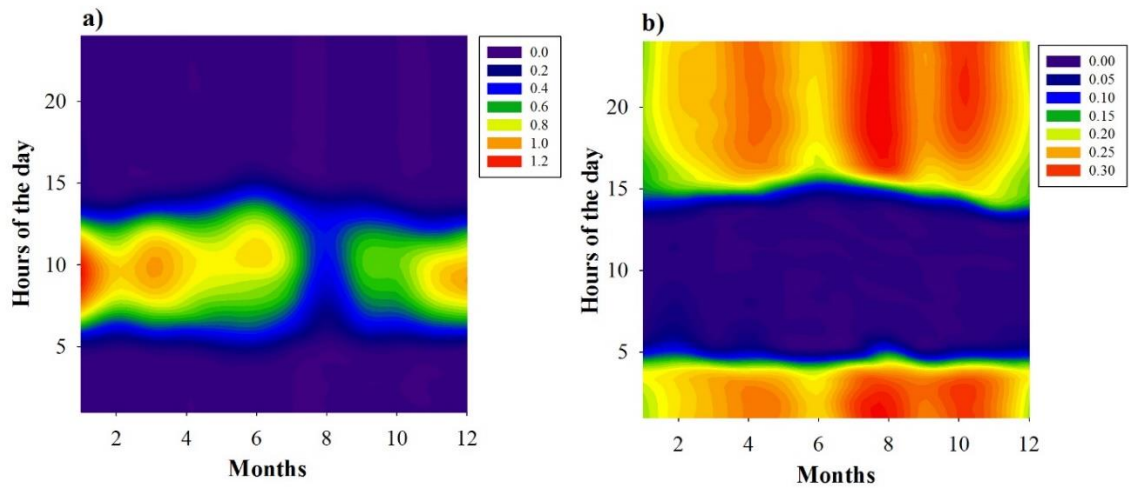
Fig. 4.45. Input power (MW) to the electrolyzer (a) and produced power (MW) by the fuel cell (b).

The produced hydrogen by the electrolyzer is shown in Fig. 4.46. Hydrogen tank that was considered for this system can save around 7500 kg hydrogen by own. This value of hydrogen can generate approximately 300 MWh electrical energy for this system. Fig. 4.47 demonstrates depleted hydrogen by the fuel cell in each hour of January. This hydrogen is consumed to provide the required energy of the system.
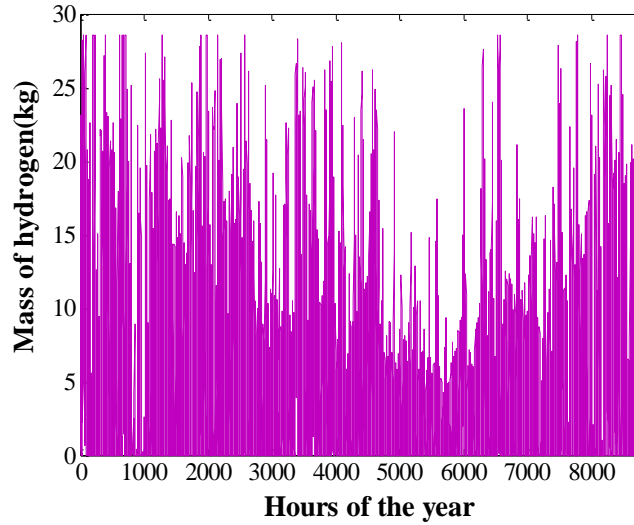
Fig. 4.46. Hydrogen produced (kg) by the electrolyzer.
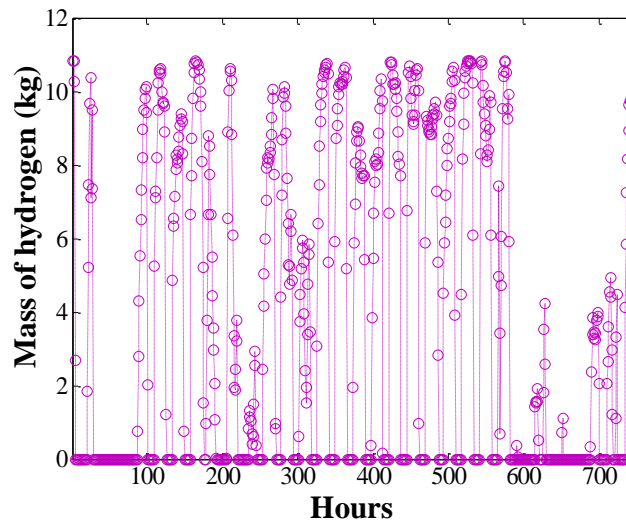
Fig. 4.47. Consumed hydrogen by the fuel cell in January.

Energy, exergy and economic analysis:

Energy and exergy analysis based on the first and second laws of thermodynamics carried out for the PVS, WTS and energy storage system. Energy and exergy analysis of the PVS is shown in Fig. 4.48. As before mentioned, the ambient temperature for the study zone between April and October is above 25°C. This value of the temperature can decrease the efficiency of the PV modules (as can be observed in Fig. 4.48). The average energy and exergy efficiencies in this region are obtained 12% and 16%, respectively.
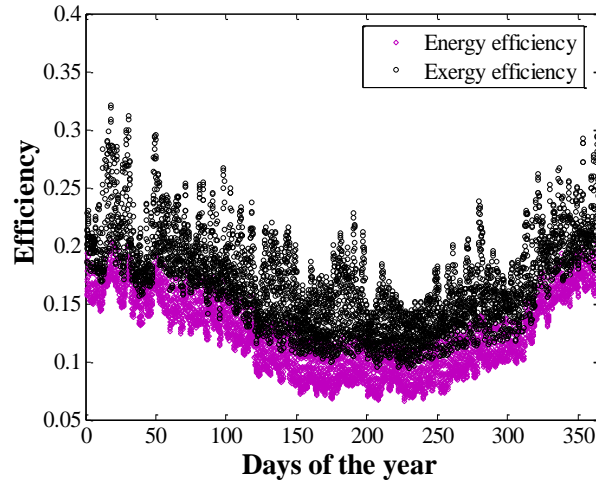
Fig. 4.48. Energy and exergy efficiency of the PVS.

Energy efficiency of the WTS for the study zone in two weeks of January, December and March is shown in Fig. 4.49. The average energy efficiency for the WTS is around 32% for one year. One of the best methods for evaluating the wind energy technology is the exergy analysis. It gives better comprehension of performance than the energy efficiency. Fig. 4.50 presents exergy analysis based on the second law of thermodynamics for the WTS in Bushehr. It is clear that the inlet and outlet exergy of the system are mainly attributed to the wind speed and due to oscillating nature of wind, exergy efficiency has different values for each time. The exergy efficiency is changed between 0 and 37% at different measured wind speed data. Also, the mean exergy efficiency for the WTS is 25.41% for one year.
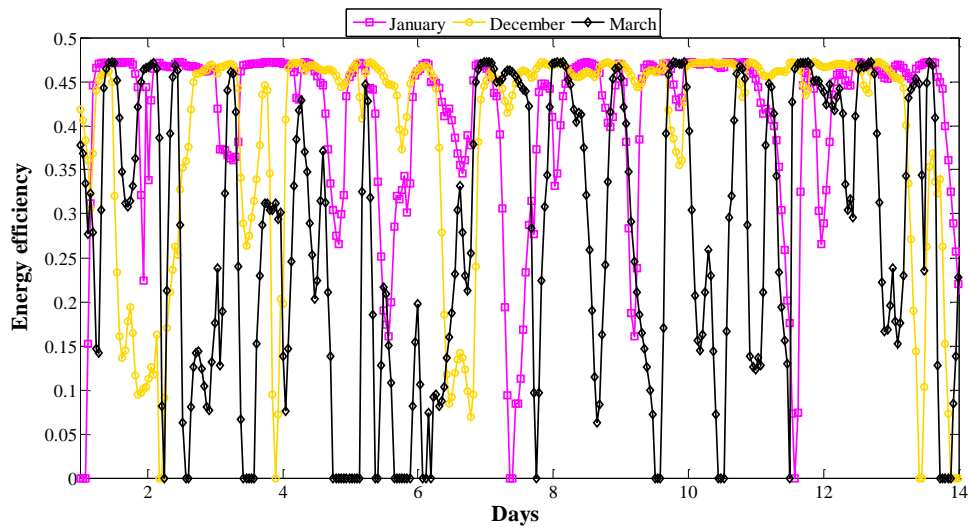
Fig. 4.49. Energy efficiency of the WT.
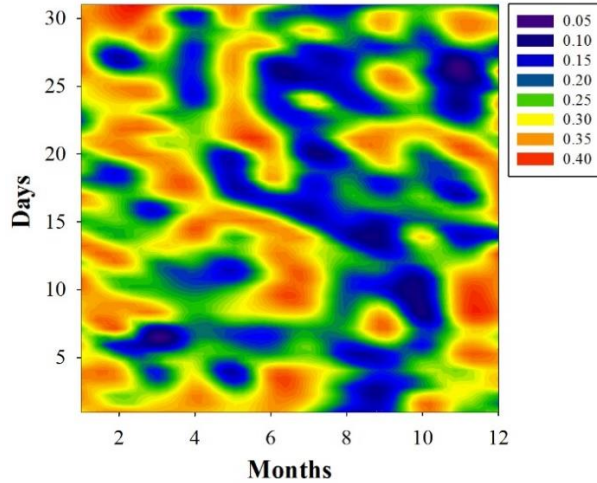
Fig. 4.50. Exergy efficiency of the WT.

Fig. 4.51 shows the input and output exergy of the electrolyzer for one year (2016), one month (January) and one week (first week of February). By considering the physical and chemical exergy of the electrolysis process and based on Eq. (3.213) the rate of exergy has been calculated. Hydrogen will be obtained from water by electrolysis, using excess generated energy rate that is more between 6:00 and 14:00.
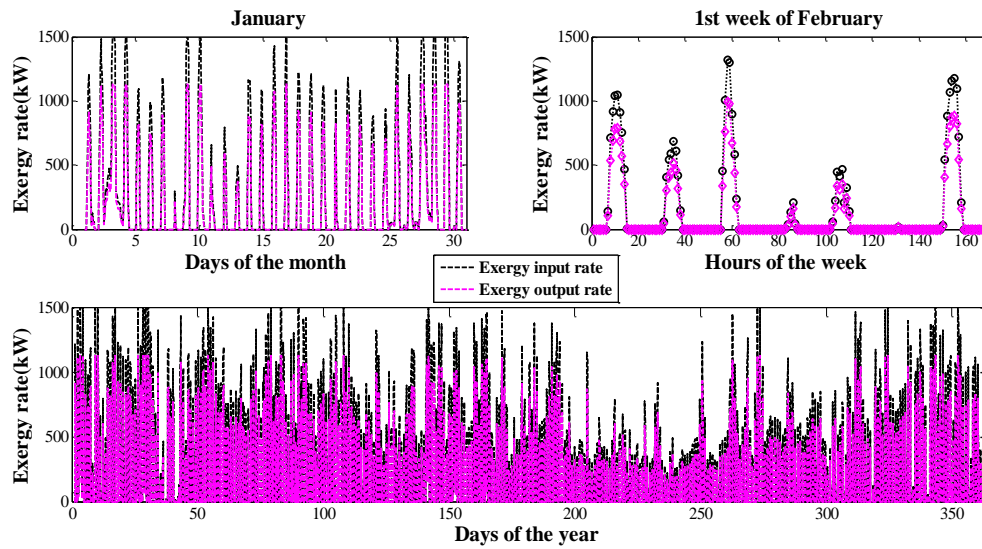
Fig. 4.51. Input and output exergy of the electrolyzer.

The rate of exergy input, output and destruction for three days in February is shown in Fig. 4.52. In Unit 132, fuel cell does not work continuously and completely relates to the required energy of the unit which changes during the day. The rate of exergy destruction changes between 0 and 100 kW.
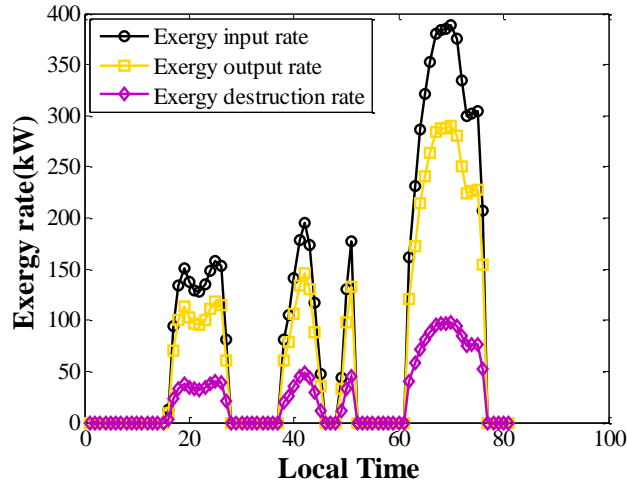
Fig. 4.52. The rate of exergy input, exergy output and exergy destruction of the fuel cell for three days.

Finally, a comprehensive exergy investigation for the proposed system is shown in Fig. 4.53. This exergy graph focuses on exergy destruction for each component of the system. At first glance, it is clear that the main part of input exergy is belonged to PVS with around 80%. Low efficiency of the PV collectors causes the maximum exergy destruction of this system by around 65%. The maximum energy efficiency for each WTS was reported to be 59.3% by Betz [176]. In this study, the average energy and exergy efficiencies for the WT are determined to be 32% and 25%, respectively. The amount of the exergy destruction for the WTS is around 13.52%. Also, the values of the exergy destruction for the electrolyzer, fuel cell and converter are 2.3%, 3.5% and 1.4%, respectively.
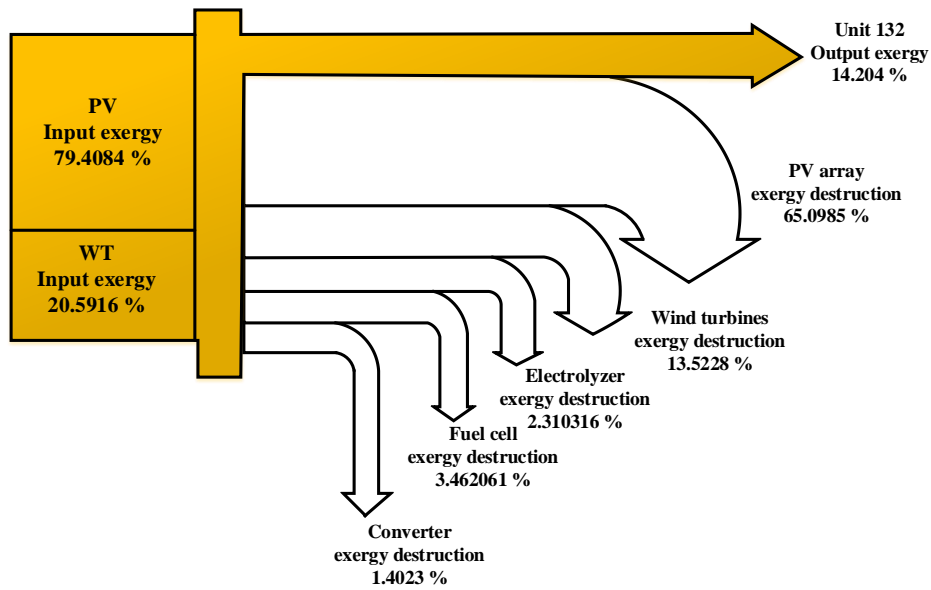
Fig. 4.53. Exergy graph of the proposed system.

Fig. 4.54 indicates the initial cost of the components that have been considered for the proposed system in this study. The WTs made up the maximum value of the cost with 28% of the total. It is clear the energy storage system that contains electrolyzer, fuel cell and hydrogen tank accounts for approximately 50% of the total. Also, PV array and converter have the 20% and 1% of the total investment, respectively.

87
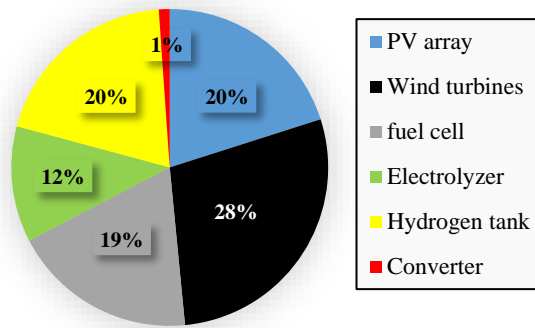
Fig. 4.54. The initial cost of the components.

The costs of the system include the installation cost as well as operation and maintenance costs. The initial investment of the hybrid renewable energy system is extremely high but the operating and maintenance costs are low. All these costs have been decreasing with the constant striving for cost-effectiveness, thereby lowering the cost of energy. Fig. 4.55 (a) demonstrates the cost of the maintenance for the project lifetime (20 years). Also, the total cost of the system contains the initial cost, the cost of maintenance, the cost of the installation and replacement of the components is shown in Fig. 4.56 (b). Total cost in the first year is around 20 million dollars. The trend is obviously upwards and reaches to 2.65 million dollars. The costs of operation and maintenance by considering the rate of inflation and replacement of the components change from 0.4 to 7 million dollars.
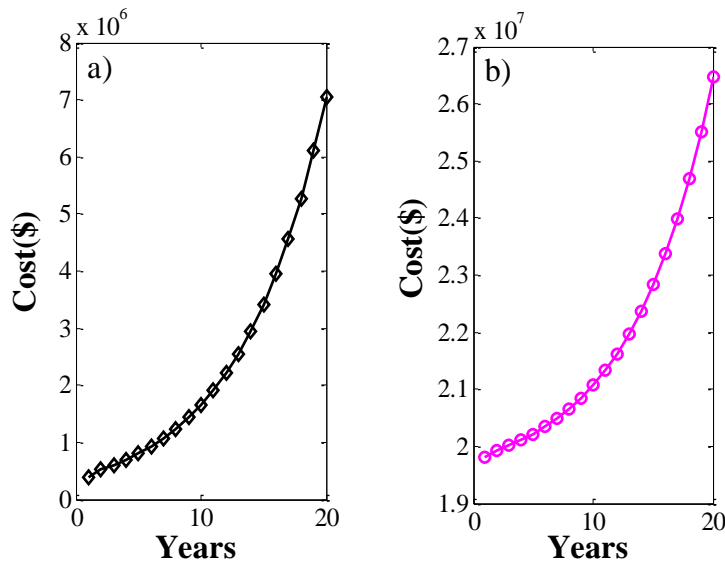
Fig. 4.55. Cost of the maintenance (a) and total cost of the system (b).

The required electrical power for Unit 132 is 320 kW. Since the initial investment was calculated for the first year, the amount of cost per kWh is approximately 7 $/kWh. In the second year, there are only the operation and maintenance costs in which the cost of the system is decreased to 0.0461 $/kWh. Thereafter, for the next years, the cost of produced electrical power will be decreased and the proposed system can compensate the initial system investment.

The payback period of the hybrid hydrogen system that has been proposed for supplying the electrical energy in Unit 132 is shown in Fig. 4.56. The initial cost of the system is approximately 20 million dollars. This initial cost will be increased by the operation and maintenance costs of each year and the rate of the inflation that is considered to be 20% for Iran [139]. The lifetime of the PV panels, wind turbines, electrolyzer and hydrogen tanks was considered to be 20 years, and fuel cells have relatively shorter lifetime which is around 5 years. The price of the electrical energy generated was considered around 0.28 \$/kWh [151] for the first year of the energy production. Also, the rate of inflation is also considered for the generated energy by the system. The payback period for the hybrid hydrogen energy system is around 11 years.
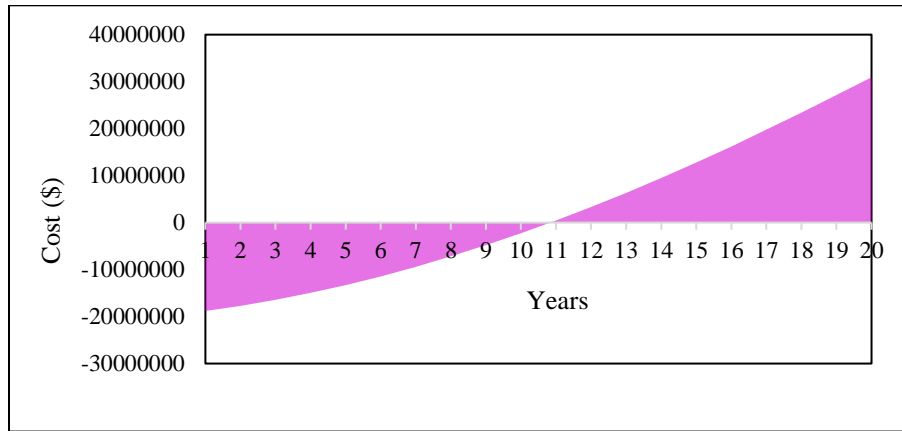
Fig. 4.56. Payback period for the proposed system.

Many investigations have proposed PV/wind system with hydrogen storage system. These studies have been applied to supply the electrical energy in different regions around the world. To the best of the authors' knowledge, most of these investigations are based on energy analysis. Table 4.16 demonstrates the average energy efficiency for each system component. As it was mentioned before, maximum energy efficiency for each wind turbine is 53%. According to Table 4.16, maximum energy efficiency for wind turbine in different case studies was reported around 40%. In this study, it is shown that the energy efficiency for WT, in the case study region, is around 32% for an annual period. This value of energy efficiency makes it a region with high potential for wind energy. An average energy efficiency between 8 and 15% have been reported by the studies for PVS. In this investigation, an average of 12% is obtained for the energy efficiency of PV panels in the case study region. Also, the range of energy efficiency changes for electrolyzer, fuel cell, hydrogen tank and inverter are shown in Table 4.16. Kalinci et al. [118] investigated hybrid hydrogen energy system for Bozcada, Turkey. They have reported the daily average exergy efficiency for the PV array and the percentage of the system exergy rate as 14.26 and 13.54%, respectively. In another study, Caliskan et al. [121] obtained an average of 9.74% exergy efficiency for the solar PV panels. In this study, the exergy efficiency for the PV panels and the percentage of the exergy rate for the system were reported around 16% and 14.204%, respectively.

Table 4.16. The range of the energy efficiency for each component.

	Studies	Energy efficiency (%)	Lifetime, years
PV	Refs. [118], [121], [119], [117], [177], [178], [179]	8-15	20-25
WT	Refs. [118], [121], [119], [180], [181], [182], [183]	25-40	20-25
Electrolyzer	Refs. [118], [121], [119], [184], [182], [178]	53-82	10-20
Fuel cell	Refs. [184], [119], [121], [185], [180], [181]	30-70	5-20
Hydrogen tank	Refs. [184], [119], [182]	95-100	10-20
Inverter	Refs. [184], [119]	90-95	10-20

Chapter 5
Conclusions

5.1. Refrigeration System

In this Ph.D. thesis, a specific type of EERS was proposed as an alternative system in order to supply the cold water for Unit 132 of the second refinery of the South Pars, Iran. This system was compared with the HXRS with three different refrigerants (R134a, R407C, and R410A). Energy, exergy, and thermo-economic analysis were implemented for both of the proposed systems. Finding the size of the components is necessary for thermo-economic analysis, hence required equations for designing the evaporator, condenser, and ejector were given. For thermo-economic analysis, the TRR method was proposed in which all the costs, including return on investment, equipment, and fuel purchase prices and the total revenue requirement were calculated annually. Energy analysis of the system demonstrated that the EERS with R134a as refrigerant has the maximum COP compared to the R134a HXRS. Also, the amount of the COP for the R410A EERS is more than R407C EERS. Exergy analysis of the systems indicated that the value of exergy destruction in the R134a EERS is lower than HXRS with R134a, R407C, and R410A refrigerants. For the R134a EERS, the maximum COP was obtained at $\Delta P = 20\ Kpa$ (pressure drop in suction nozzle) in which PR has the minimum value. Also, the COP of the R134a EERS was decreased with an increase in condensing temperature. Effect of the evaporation and condensing temperatures on diameters of the diffuser, suction nozzle, motive nozzle, and motive section have been evaluated. Increasing in pressure drop in suction nozzle decreased the diameter of the suction nozzle and mixing section. Also, the diameter of the mixing section was decreased with an increase of the condensing and evaporation temperatures. Thermo-economic analysis illustrated that the total cost of the components in the EERS is almost 3% lower than HXRS but the total costs of the fuel and the refrigeration system are 22% and 15.2% lower than HXRS, respectively. In addition, the values of the condensing and evaporation temperatures for designing the evaporator and condenser were proposed to be 58.5°C and 20°C, respectively. The results of this study demonstrated that by considering energy, exergy, and thermo-economic analysis, using the ejector expansion device in refrigeration systems for supplying the cold water is highly recommended.

5.2. Artificial intelligence methods

5.2.1. Solar Energy Prediction

Solar power is a vast, free and renewable resource that can be used to produce electricity. Solar-generated electricity produces no greenhouse gases or emissions of any kind. Solar energy is a commercially-proven, rapidly growing form of electricity generation. Machine learning algorithms were used in order to predict the solar radiation in the study region. In first methodology (N_1), pressure, temperature, relative humidity, wind speed and local time were used to predict solar irradiance. In this network, the amount of the solar radiation that has been recorded during the past few months or years was used to train the network in order to find the solar irradiance with the new inputs. Indeed, it is trained a network to predict the solar irradiance with the before mentioned inputs and without solar irradiance data

collection. The second methodology (N_2) is time-series prediction that developed models used the past values measured solar radiation in order to estimate the future values. Thus the developed models always require solar irradiance database to forecast the future values. This type of forecasting model is valuable for grid operators in order to make decisions of grid operation and also for electric market operators. For the N_1, the MLFFNN, RBFNN, SVR, and FIS models were proposed and compared to each other. For the N_2, the MLFFNN, SVR, FIS, ANFIS-FCM, ANFIS-SC, and ANFIS-GP were developed to forecast solar radiation. This study has led to conclusions in the following, for the N_1:

The MLFFNN was trained with six data training algorithms. The results illustrated that LM and BR have highest correlation coefficient for the test data respectively with 0.9887 and 0.9819. The RBFNN was implemented with six different spread parameter that for this analysis the best performance was obtained in spread to be 6 in which R and RMSE for the test data were 0.88011 and 150.1416, respectively. Also, the SVR model with different user-determined parameters was applied to predict the targets. This model has shown the highest R close to 1 and RMSE=1.053 (Wh/m^2). In addition, the FIS model was applied in order to estimate the solar irradiance. The best performance was achieved by considering the four MFs for each input and target. For this state R and RMSE for the test data are 0.8787 and 171.256 (Wh/m^2), respectively. The comparison of the developed models illustrated that the SVR model and MLFFNN have the maximum efficiency for forecasting the solar radiation.

For the N_2:

Time-series data of hourly solar irradiance was predicted with the MLFFNN. For this purpose, different data training algorithms were used in order to obtain the better performance. The results illustrated that the LM and BR training algorithms have the maximum correlation coefficient for the test data respectively with 0.9526 and 0.9570. The maximum performance was obtained with 70 neurons in the hidden layer. It can be observed, this model has shown a better performance for N_1 compared to N_2. The SVR models reported the maximum performance for time-series prediction with R=0.9999 and RMSE=9.1363 (Wh/m^2). Also, the FIS model demonstrated the better outputs for the N_2 compared to the N_1. This model estimated the targets with approximately 95% accuracy in the test data. In addition, three types of ANFIS model were evaluated in order to forecast the target. ANFIS-FCM with 10 clusters has shown the best performance with R=0.95279 and RMSE=83.1365 (Wh/m^2) for the test data. As a result, for the N_2, although the SVR and ANFIS-FCM have shown the better performance for time-series forecasting, the other developed models also reported the outputs with around 94% accuracy in the test data.

5.2.2. Wind Speed Prediction

Although Iran is among the countries with the huge reserves of fossil fuels and non-renewable sources of energy such as oil and gas, it benefits a remarkable potential of renewable energies such as the wind, solar, biomass and geothermal. The wind turbine system is one of the most competitive sources in the field of renewable energy technologies. Despite several studies which investigated wind energy in different worldwide regions, different patterns of power produced from wind energy have led to the fact that this research is being continued in wind energy systems. This study has led to conclusions in the following:

Three methods of machine learning algorithms were developed to predict the wind speed, wind direction and output power of the WT in Bushehr, located in the south of Iran. Pressure, temperature, local time and relative humidity of the region were considered to be the input variables. The first model was MLFFNN that was trained with nine data training algorithms. The LM and BR algorithms have shown the minimum errors between the actual and predicted data. The second model was SVR with RBF as kernel function. This model was adjusted with three different used-defined parameters that the best performance of the model was obtained by $\varepsilon=0.5$, $\sigma=1$ and $C=1000$. The third method was ANFIS that was optimized with a PSO algorithm. Forecasting models were compared with 5-min, 10-min, 30-min and 1-h intervals of wind speed and its direction. For 5-min and 10-min intervals of wind speed data, the predicted values were found to be in excellent agreement with the actual data for three developed models. For other time intervals, the SVR-RBF model performs better than the MLFFNN and ANFIS-PSO in terms of R, MSE and MSE. For wind direction prediction, the developed models have shown lower performance compared to wind speed prediction.

5.3. Hybrid Renewable Energy System

Utilizing solar and wind energy with hydrogen will have strong environmental effect, to promote the concept of using renewable and clean resources and protect the environment. Hydrogen is the suitable energy carrier to store solar and wind energy and transform them to electrical energy. If there is a need to store a large amount of energy for a long time, hydrogen storage system is today often cheaper and more compact than battery storage. So hydrogen is preferred as media in a long-term storage. The solar/wind energy with hydrogen energy storage system for supplying the constant electrical load in a large scale in the south of Iran was proposed. The results demonstrated that although Iran is rich in fossil fuel resources, analysis of the solar and wind energy stated that this country is a suitable place for applying the solar and wind energy systems. The monthly optimum slope angle for solar collectors was determined with the minimum value in June as -9° and the maximum value in December as 57°. Also, the optimum azimuth angle was found as 30° for the study zone. The solar radiation with the monthly optimum tilt angle was found around 20% more than the horizontal collectors. It is found that the amount of the absorption radiation with the optimum slope angle in such months of the year allows producing more power. The energy and exergy analysis of the PVS have been reported by average of 12% energy efficiency and 16% exergy efficiency. Analysis the ambient temperature of the Bushehr demonstrated that the temperature for June, July, August and September is more than 28℃ and this temperature can be decreased the efficiency of the PVS. Therefore, in these months authors suggest using a cooling system for PV modules. Investigation on power generation of WTs illustrated that between April and August and from 9:00 to 14:00 the power produced by wind farm is above 800 kW. In other months of the year, this power is less than 600 kW. Also, for 00:00 to 5:00 and 16:00 to 24:00 the generated power is around 800 kW in this region. Despite the energy efficiency for the WTS in some days is close to 50%, the average energy efficiency in this region for the WT was reported around 32%. Exergy analysis using the second law of thermodynamics for evaluating the quality of energy was done in this station. Exergy efficiency of the WTS was changed between 0 and 37% and the average value of it was obtained around 26%. Investigation of exergy destruction of the system illustrated that the PVS has the maximum exergy destruction with 65% of the total. The portion of exergy destroyed of the WTs is 13.52%. Also, the less role of exergy destruction belongs to the electrolyzer, fuel cell and converter with 2.3%, 3.5% and 1.4%,

93

respectively. Between January and June excess energy was transferred to the electrolyzer and hydrogen was produced and stored in the hydrogen tanks. In June to December this energy was consumed by the unit. Economic analysis illustrated that the PVS, WTS and energy storage system were included around 20%, 28% and 50% of the total investment, respectively. In addition, the payback period for the hybrid renewable energy was obtained around 11 years.

Future work

It is proposed to work on the following suggestions as the future works:

1. A new intelligent model based on support vector regression optimized with imperialist competitive algorithm for prediction of solar radiation and wind speed data.

2. A new approach based on support vector regression optimized with particle swarm optimization algorithm to prediction of wind speed and solar radiation data.

3. Energy, exergy and economic analyses of ocean thermal energy conversion/photovoltaic/wind turbine system with hydrogen energy storage system.

4. Energy and exergy analyses of geothermal energy system equipped with solar energy with hydrogen storage system

5. Energy and exergy analyses of photovoltaic/wind turbine system with compressed air energy storage (CAES) system

6. Energy and exergy analyses of geothermal/photovoltaic energy system for supplying electrical energy

References

[1] "Science - Ozone Basics." [Online]. Available: http://www.ozonelayer.noaa.gov/science/basics.htm. [Accessed: 17-Apr-2017].

[2] A. Gillespie, *Climate change, ozone depletion and air pollution: legal commentaries within the context of science and policy*. Brill, 2006.

[3] R. N. Faria, R. O. Nunes, R. N. N. Koury, and L. Machado, "Dynamic modeling study for a solar evaporator with expansion valve assembly of a transcritical CO2 heat pump," *Int. J. Refrig.*, vol. 64, pp. 203–213, 2016.

[4] G. K. Singh, "Solar power generation by PV (photovoltaic) technology: A review," *Energy*, vol. 53, pp. 1–13, 2013.

[5] M. Hossain, S. Mekhilef, M. Danesh, L. Olatomiwa, and S. Shamshirband, "Application of extreme learning machine for short term output power forecasting of three grid-connected PV systems," *J. Clean. Prod.*, vol. 167, pp. 395–405, Nov. 2017.

[6] L. Martín, L. F. Zarzalejo, J. Polo, A. Navarro, R. Marchante, and M. Cony, "Prediction of global solar irradiance based on time series analysis: Application to solar thermal power plants energy production planning," *Sol. Energy*, vol. 84, no. 10, pp. 1772–1781, 2010.

[7] A. Alzahrani, J. W. Kimball, and C. Dagli, "Predicting solar irradiance using time series neural networks," *Procedia Comput. Sci.*, vol. 36, no. C, pp. 623–628, 2014.

[8] A. Sharma and A. Kakkar, "Forecasting daily global solar irradiance generation using machine learning," *Renew. Sustain. Energy Rev.*, no. July, pp. 0–1, 2017.

[9] I. A. Ibrahim and T. Khatib, "A novel hybrid model for hourly global solar radiation prediction using random forests technique and firefly algorithm," *Energy Convers. Manag.*, vol. 138, pp. 413–425, 2017.

[10] K. Mohammadi, A. Mostafaeipour, and M. Sabzpooshani, "Assessment of solar and wind energy potentials for three free economic and industrial zones of Iran," *Energy*, vol. 67, pp. 117–128, Apr. 2014.

[11] Y. Jiang and G. Huang, "Short-term wind speed prediction : Hybrid of ensemble empirical mode decomposition , feature selection and error correction," *Energy Convers. Manag.*, vol. 144, pp. 340–350, 2017.

[12] Ü. Ba and T. Filik, "Wind Speed Prediction Using Artificial Neural Networks Based on Multiple Local Measurements in Eskisehir," *Energy Procedia*, vol. 107, no. September 2016, pp. 264–269, 2017.

[13] I. Kirbas and A. Kerem, "Short-Term Wind Speed Prediction Based on Artificial Neural Network Models," *Meas. Control*, vol. 49, no. 6, pp. 183–190, 2016.

[14] M. Bilgili, B. Sahin, and A. Yasar, "Application of artificial neural networks for the wind speed prediction of target station using reference stations data," *Renew. Energy*, vol. 32, no. 14, pp. 2350–2360, 2007.

[15] P. Ramasamy, S. S. Chandel, and A. K. Yadav, "Wind speed prediction in the mountainous region of India using an arti fi cial neural network model," *Renew. Energy*, vol. 80, no. March 2014, pp. 338–347, 2015.

[16] S. K. P and D. Lopez, "Forecasting of Wind Speed Using Feature Selection and Neural Networks," *Int. J. Renew. Energy Res.*, vol. 6, no. 3, 2016.

[17] K. Sreelakshmi and P. Ramakanthkumar, "Neural Networks for Short Term Wind Speed Prediction," *Int. J. Comput. Electr. Autom. Control Inf. Eng.*, vol. 2, no. 6, pp. 2019–2023, 2008.

[18] H. Masur and M. Nimol, "Short Term Wind Speed Forecasting Using Artificial Neural Network : A Case Study," *Int. Conf. Innov. Sci. Eng. Technol.*, pp. 0–4, 2016.

[19] G. Li and J. Shi, "On comparing three artificial neural networks for wind speed forecasting," *Appl. Energy*,

vol. 87, no. 7, pp. 2313–2320, 2010.

[20]   F. Fazelpour, N. Tarashkar, and M. A. Rosen, "Short-term wind speed forecasting using artificial neural networks for Tehran , Iran," *Int. J. Energy Environ. Eng.*, 2016.

[21]   B. Doucoure, K. Agbossou, and A. Cardenas, "Time series prediction using arti fi cial wavelet neural network and multi-resolution analysis : Application to wind speed data," *Renew. Energy*, vol. 92, pp. 202–211, 2016.

[22]   H. S. Nogay, "Application of artificial neural networks for short term wind speed forecasting in Mardin , Turkey," *J. Energy South. Africa*, vol. 23, no. 4, pp. 2–7, 2012.

[23]   G. Najafi, B. Ghobadian, R. Mamat, T. Yusaf, and W. H. Azmi, "Solar energy in Iran: Current state and outlook," *Renew. Sustain. Energy Rev.*, vol. 49, pp. 931–942, 2015.

[24]   D. Fadai, "The feasibility of manufacturing wind turbines in Iran," *Renew. Sustain. Energy Rev.*, vol. 11, no. 3, pp. 536–542, 2007.

[25]   "NASA-SSE   -   www.soda-pro.com."   [Online].   Available: http://www.soda-pro.com/web-services/radiation/nasa-sse. [Accessed: 01-Sep-2017].

[26]   R. N. N. Koury, L. Machado, and K. A. R. Ismail, "Numerical simulation of a variable speed refrigeration system," *Int. J. Refrig.*, vol. 24, no. 2, pp. 192–200, Mar. 2001.

[27]   M.-H. Yang, R.-H. Yeh, and T.-C. Hung, "Thermo-economic analysis of the transcritical organic Rankine cycle using R1234yf/R32 mixtures as the working fluids for lower-grade waste heat recovery," *Energy*, Sep. 2017.

[28]   A. A. Kornhauser, "The use of an ejector as a refrigerant expander," 1990.

[29]   K. Sumeru, H. Nasution, and F. N. Ani, "A review on two-phase ejector as an expansion device in vapor compression refrigeration cycle," *Renew. Sustain. Energy Rev.*, vol. 16, no. 7, pp. 4927–4937, 2012.

[30]   S. Fangtian and M. Yitai, "Thermodynamic analysis of transcritical CO 2 refrigeration cycle with an ejector," *Appl. Therm. Eng.*, vol. 31, no. 6, pp. 1184–1189, 2011.

[31]   M. Zhou, X. Wang, and J. Yu, "Theoretical study on a novel dual-nozzle ejector enhanced refrigeration cycle for household refrigerator-freezers," *Energy Convers. Manag.*, vol. 73, no. September 2013, pp. 278–284, 2013.

[32]   S. Aphornratana and I. W. Eames, "A small capacity steam-ejector refrigerator: experimental investigation of a system using ejector with movable primary nozzle," *Int. J. Refrig.*, vol. 20, no. 5, pp. 352–358, 1997.

[33]   M. Hassanain, E. Elgendy, and M. Fatouh, "Ejector expansion refrigeration system: Ejector design and performance evaluation," *Int. J. Refrig.*, vol. 58, pp. 1–13, 2015.

[34]   S. Wongwises and S. Disawas, "Performance of the two-phase ejector expansion refrigeration cycle," *Int. J. Heat Mass Transf.*, vol. 48, no. 19–20, pp. 4282–4286, 2005.

[35]   L. Zheng, J. Deng, Y. He, and P. Jiang, "Dynamic model of a transcritical CO2 ejector expansion refrigeration system," *Int. J. Refrig.*, vol. 60, pp. 247–260, Dec. 2015.

[36]   H. Li, F. Cao, X. Bu, L. Wang, and X. Wang, "Performance characteristics of R1234yf ejector-expansion refrigeration cycle," *Appl. Energy*, vol. 121, pp. 96–103, 2014.

[37]   T. Thongtip and S. Aphornratana, "An alternative analysis applied to investigate the ejector performance used in R141b jet-pump refrigeration system," *Int. J. Refrig.*, vol. 53, pp. 20–33, 2015.

[38]   A. Farsi, S. M. H. Mohammadi, and M. Ameri, "Thermo-economic comparison of three configurations of combined supercritical CO 2 refrigeration and multi-effect desalination systems," *Appl. Therm. Eng.*, vol. 112, pp. 855–870, 2017.

[39]   M. Sadeghi, S. M. S. Mahmoudi, and R. Khoshbakhti Saray, "Exergoeconomic analysis and multi-objective

97

optimization of an ejector refrigeration cycle powered by an internal combustion (HCCI) engine," *Energy Convers. Manag.*, vol. 96, pp. 403–417, 2015.

[40] F. Fazelpour and T. Morosuk, "Exergoeconomic analysis of carbon dioxide transcritical refrigeration machines," *Int. J. Refrig.*, vol. 38, no. 1, pp. 128–139, 2014.

[41] O. Rezayan and A. Behbahaninia, "Thermoeconomic optimization and exergy analysis of CO2/NH3 cascade refrigeration systems," *Energy*, vol. 36, no. 2, pp. 888–895, 2011.

[42] K. Thulukkanam, *Heat Exchanger Design Handbook, Second Edition*. 2013.

[43] H. S. Lee, *Thermal Design: Heat Sinks, Thermoelectrics, Heat Pipes, Compact Heat Exchangers, and Solar Cells*. 2010.

[44] F. Liu and E. A. Groll, "Study of ejector efficiencies in refrigeration cycles," *Appl. Therm. Eng.*, vol. 52, no. 2, pp. 360–370, 2013.

[45] W. Chen, C. Shi, S. Zhang, H. Chen, D. Chong, and J. Yan, "Theoretical analysis of ejector refrigeration system performance under overall modes," *Appl. Energy*, pp. 1–11, 2015.

[46] J. Deng, P. Jiang, T. Lu, and W. Lu, "Particular characteristics of transcritical CO 2 refrigeration cycle with an ejector," *Appl. Therm. Eng.*, vol. 27, no. 2, pp. 381–388, 2007.

[47] Y. Huai, X. Guo, and Y. Shi, "Experimental Study on Performance of Double-throttling Device Transcritical CO2 Ejector Refrigeration System," *Energy Procedia*, vol. 105, pp. 5106–5113, May 2017.

[48] L. Zheng and J. Deng, "Experimental investigation on a transcritical CO 2 ejector expansion refrigeration system with two-stage evaporation," *Appl. Therm. Eng.*, Jul. 2017.

[49] K. D. Choudhary, M. S. Dasgupta, and S. sunder, "Energetic and Exergetic Investigation of a N 2 O Ejector Expansion Transcritical Refrigeration Cycle," *Energy Procedia*, vol. 109, pp. 122–129, Mar. 2017.

[50] H. K. Ersoy and N. Bilir, "Performance characteristics of ejector expander transcritical CO2 refrigeration cycle," *Proc. Inst. Mech. Eng. Part A J. Power Energy*, vol. 226, no. 5, pp. 623–635, 2012.

[51] M. Elakdhar, E. Nehdi, and L. Kairouani, "Analysis of a compression/ejection cycle for domestic refrigeration," *Ind. Eng. Chem. Res.*, vol. 46, no. 13, pp. 4639–4644, 2007.

[52] F. Liu and E. A. Groll, "Study of ejector efficiencies in refrigeration cycles," *Appl. Therm. Eng.*, vol. 52, no. 2, pp. 360–370, 2013.

[53] N. Bilir Sag, H. K. Ersoy, A. Hepbasli, and H. S. Halkaci, "Energetic and exergetic comparison of basic and ejector expander refrigeration systems operating under the same external conditions and cooling capacities," *Energy Convers. Manag.*, vol. 90, no. June, pp. 184–194, 2015.

[54] M. Rasti, M. S. Hatamipour, S. F. Aghamiri, and M. Tavakoli, "Enhancement of domestic refrigerator's energy efficiency index using a hydrocarbon mixture refrigerant," *Measurement*, vol. 45, no. 7, pp. 1807–1813, 2012.

[55] G. Pottker, B. Guo, and P. S. Hrnjak, "Experimental investigation of an R410A vapor compression system working with an ejector," 2010.

[56] K. Megdouli, B. M. Tashtoush, Y. Ezzaalouni, E. Nahdi, A. Mhimid, and L. Kairouani, "Performance analysis of a new ejector expansion refrigeration cycle (NEERC) for power and cold: Exergy and energy points of view," *Appl. Therm. Eng.*, vol. 122, pp. 39–48, Jul. 2017.

[57] Ş. Ünal, M. T. Erdinç, and Ç. Kutlu, "Optimal thermodynamic parameters of two-phase ejector refrigeration system for buses," *Appl. Therm. Eng.*, vol. 124, pp. 1354–1367, Sep. 2017.

[58] M. H. Eldakamawy, M. V. Sorin, and M. Brouillette, "Energy and exergy investigation of ejector refrigeration systems using retrograde refrigerants," *Int. J. Refrig.*, vol. 78, pp. 176–192, Jun. 2017.

[59]   J. Dong, M. Yu, W. Wang, H. Song, C. Li, and X. Pan, "Experimental investigation on low-temperature thermal energy driven steam ejector refrigeration system for cooling application," *Appl. Therm. Eng.*, vol. 123, pp. 167–176, Aug. 2017.

[60]   J. Hu, J. Shi, Y. Liang, Z. Yang, and J. Chen, "Numerical and experimental investigation on nozzle parameters for R410A ejector air conditioning system," *Int. J. Refrig.*, vol. 40, pp. 338–346, 2014.

[61]   X. Wang, J. Yu, M. Zhou, and X. Lv, "Comparative studies of ejector-expansion vapor compression refrigeration cycles for applications in domestic refrigerator-freezers," *Energy*, vol. 70, no. January, pp. 635–642, 2014.

[62]   J. Song, J. Wang, and H. Lu, "A novel combined model based on advanced optimization algorithm for short-term wind speed forecasting," *Appl. Energy*, vol. 215, pp. 643–658, Apr. 2018.

[63]   C. D. Zuluaga, M. A. Álvarez, and E. Giraldo, "Short-term wind speed prediction based on robust Kalman filtering: An experimental comparison," *Appl. Energy*, vol. 156, pp. 321–330, Oct. 2015.

[64]   D. A. Fadare, "The application of artificial neural networks to mapping of wind speed profile for energy application in Nigeria," *Appl. Energy*, vol. 87, no. 3, pp. 934–942, 2010.

[65]   F. Douak, F. Melgani, and N. Benoudjit, "Kernel ridge regression with active learning for wind speed prediction," *Appl. Energy*, vol. 103, pp. 328–340, Mar. 2013.

[66]   K. Chen and J. Yu, "Short-term wind speed prediction using an unscented Kalman filter based state-space support vector regression approach," *Appl. Energy*, vol. 113, pp. 690–705, Jan. 2014.

[67]   Ü. B. Filik and T. Filik, "Wind Speed Prediction Using Artificial Neural Networks Based on Multiple Local Measurements in Eskisehir," *Energy Procedia*, vol. 107, no. September 2016, pp. 264–269, 2017.

[68]   H. Akçay and T. Filik, "Short-term wind speed forecasting by spectral analysis from long-term observations with missing values," *Appl. Energy*, vol. 191, pp. 653–662, 2017.

[69]   J. A. Carta, P. Cabrera, J. M. Matías, and F. Castellano, "Comparison of feature selection methods using ANNs in MCP-wind speed methods. A case study," *Appl. Energy*, vol. 158, pp. 490–507, 2015.

[70]   A. N. Celik and M. Kolhe, "Generalized feed-forward based method for wind energy prediction," *Appl. Energy*, vol. 101, pp. 582–588, 2013.

[71]   H. Liu, H.-Q. Tian, X.-F. Liang, and Y.-F. Li, "Wind speed forecasting approach using secondary decomposition algorithm and Elman neural networks," *Appl. Energy*, vol. 157, pp. 183–194, 2015.

[72]   W. Zhao, Y. M. Wei, and Z. Su, "One day ahead wind speed forecasting: A resampling-based approach," *Appl. Energy*, vol. 178, pp. 886–901, 2016.

[73]   J. Wang, T. Niu, H. Lu, Z. Guo, W. Yang, and P. Du, "An analysis-forecast system for uncertainty modeling of wind speed: A case study of large-scale wind farms," *Appl. Energy*, vol. 211, pp. 492–512, Feb. 2018.

[74]   V. Vapnik, *The nature of statistical learning theory*. Springer science & business media, 2013.

[75]   H. Y. Cheng, C. C. Yu, and S. J. Lin, "Bi-model short-term solar irradiance prediction using support vector regressors," *Energy*, vol. 70, pp. 121–127, 2014.

[76]   Y. Yaslan and B. Bican, "Empirical mode decomposition based denoising method with support vector regression for time series prediction: A case study for electricity load forecasting," *Measurement*, vol. 103, pp. 52–61, 2017.

[77]   J. Antonanzas, R. Urraca, F. J. Martinez-De-Pison, and F. Antonanzas-Torres, "Solar irradiation mapping with exogenous data from support vector regression machines estimations," *Energy Convers. Manag.*, vol. 100, pp. 380–390, 2015.

[78]   K. Mohammadi, S. Shamshirband, M. H. Anisi, K. Amjad Alam, and D. Petković, "Support vector regression based prediction of global solar radiation on a horizontal surface," *Energy Convers. Manag.*, vol. 91, pp. 433–

441, 2015.

[79]   J. Wang, Z. J. Zhai, Y. Jing, and C. Zhang, "Particle swarm optimization for redundant building cooling heating and power system," *Appl. Energy*, vol. 87, no. 12, pp. 3668–3679, 2010.

[80]   G. W. Chang, H. J. Lu, Y. R. Chang, and Y. D. Lee, "An improved neural network-based approach for short-term wind speed and power forecast," *Renew. Energy*, vol. 105, p. 301e311 Contents, 2017.

[81]   H. Liu, J. Shi, and E. Erdem, "Prediction of wind speed time series using modified Taylor Kriging method," *Energy*, vol. 35, no. 12, pp. 4870–4879, 2010.

[82]   Y. Noorollahi, M. A. Jokar, and A. Kalhor, "Using artificial neural networks for temporal and spatial wind speed forecasting in Iran," *Energy Convers. Manag.*, vol. 115, pp. 17–25, 2016.

[83]   I. Schicker, P. Papazek, A. Kann, and Y. Wang, "Short-range wind speed predictions for complex terrain using an interval-artificial neural network," *Energy Procedia*, vol. 125, no. September, pp. 199–206, 2017.

[84]   G. Kumar and H. Malik, "Generalized Regression Neural Network Based Wind Speed Prediction Model For Western Region Of India," *Procedia Comput. Sci.*, vol. 93, pp. 26–32, 2016.

[85]   K. G. Sheela, S. N. Deepa, and R. W. Newcomb, "Neural network based hybrid computing model for wind speed prediction," *Neurocomputing*, vol. 122, pp. 425–429, 2013.

[86]   D. Petkovic, "Adaptive neuro-fuzzy approach for estimation of wind speed distribution," *Int. J. Electr. Power Energy Syst.*, vol. 73, pp. 389–392, 2015.

[87]   G. Santamaría-Bonfil, A. Reyes-Ballesteros, and C. Gershenson, "Wind speed forecasting for wind farms: A method based on support vector regression," *Renew. Energy*, vol. 85, pp. 790–809, 2016.

[88]   X. Mi, H. Liu, and Y. Li, "Wind speed forecasting method using wavelet, extreme learning machine and outlier correction algorithm," *Energy Convers. Manag.*, vol. 151, no. April, pp. 709–722, 2017.

[89]   G. Li and J. Shi, "On comparing three artificial neural networks for wind speed forecasting," *Appl. Energy*, vol. 87, no. 7, pp. 2313–2320, Jul. 2010.

[90]   J. Koo, G. D. Han, H. J. Choi, and J. H. Shim, "Wind-speed prediction and analysis based on geological and distance variables using an artificial neural network: A case study in South Korea," *Energy*, vol. 93, pp. 1296–1302, Dec. 2015.

[91]   A. Lodge and X.-H. Yu, "Short term wind speed prediction using artificial neural networks," in *2014 4th IEEE International Conference on Information Science and Technology*, 2014, pp. 539–542.

[92]   M. A. Mohandes, T. O. Halawani, S. Rehman, and A. A. Hussain, "Support vector machines for wind speed prediction," *Renew. Energy*, vol. 29, no. 6, pp. 939–947, May 2004.

[93]   M. Bilgili, B. Sahin, and A. Yasar, "Application of artificial neural networks for the wind speed prediction of target station using reference stations data," *Renew. Energy*, vol. 32, no. 14, pp. 2350–2360, Nov. 2007.

[94]   S. Salcedo-Sanz, E. G. Ortiz-Garcı́a, Á. M. Pérez-Bellido, A. Portilla-Figueras, and L. Prieto, "Short term wind speed prediction based on evolutionary support vector regression algorithms," *Expert Syst. Appl.*, vol. 38, no. 4, pp. 4052–4057, Apr. 2011.

[95]   D. Liu, D. Niu, H. Wang, and L. Fan, "Short-term wind speed forecasting using wavelet transform and support vector machines optimized by genetic algorithm," *Renew. Energy*, vol. 62, pp. 592–597, 2014.

[96]   A. Qazi, H. Fayaz, A. Wadi, R. G. Raj, N. A. Rahim, and W. A. Khan, "The artificial neural network for solar radiation prediction and designing solar systems: a systematic literature review," *J. Clean. Prod.*, vol. 104, pp. 1–12, Oct. 2015.

[97]   C. Renno, F. Petito, and A. Gatto, "ANN model for predicting the direct normal irradiance and the global radiation for a solar application to a residential building," *J. Clean. Prod.*, vol. 135, pp. 1298–1316, 2016.

100

[98]   V. H. Quej, J. Almorox, M. Ibrakhimov, and L. Saito, "Estimating daily global solar radiation by day of the year in six cities located in the Yucatán Peninsula, Mexico," *J. Clean. Prod.*, vol. 141, pp. 75–82, Jan. 2017.

[99]   K.-P. Lin and P.-F. Pai, "Solar power output forecasting using evolutionary seasonal decomposition least-square support vector regression," *J. Clean. Prod.*, vol. 134, pp. 456–462, Oct. 2016.

[100]   S. Mehdizadeh, J. Behmanesh, and K. Khalili, "Application of gene expression programming to predict daily dew point temperature," *Appl. Therm. Eng.*, vol. 112, pp. 1097–1107, 2017.

[101]   S. Mehdizadeh, J. Behmanesh, and K. Khalili, "Using MARS, SVM, GEP and empirical equations for estimation of monthly mean reference evapotranspiration," *Comput. Electron. Agric.*, vol. 139, pp. 103–114, 2017.

[102]   I. Loghmari, Y. Timoumi, and A. Messadi, "Performance comparison of two global solar radiation models for spatial interpolation purposes," *Renew. Sustain. Energy Rev.*, vol. 82, no. November 2016, pp. 837–844, 2018.

[103]   Y. Kashyap, A. Bansal, and A. K. Sao, "Solar radiation forecasting with multiple parameters neural networks," *Renew. Sustain. Energy Rev.*, vol. 49, pp. 825–835, 2015.

[104]   J. Wu, C. K. Chan, Y. Zhang, B. Y. Xiong, and Q. H. Zhang, "Prediction of solar radiation with genetic approach combing multi-model framework," *Renew. Energy*, vol. 66, pp. 132–139, 2014.

[105]   R. Meenal and A. I. Selvakumar, "Assessment of SVM, Empirical and ANN based solar radiation prediction models with most influencing input parameters," *Renew. Energy*, 2017.

[106]   L. Olatomiwa, S. Mekhilef, S. Shamshirband, and D. Petkovic, "Adaptive neuro-fuzzy approach for solar radiation prediction in Nigeria," *Renew. Sustain. Energy Rev.*, vol. 51, pp. 1784–1791, 2015.

[107]   E. F. Alsina, M. Bortolini, M. Gamberi, and A. Regattieri, "Artificial neural network optimisation for monthly average daily global solar radiation prediction," *Energy Convers. Manag.*, vol. 120, pp. 320–329, 2016.

[108]   L. Wang, O. Kisi, M. Zounemat-Kermani, G. A. Salazar, Z. Zhu, and W. Gong, "Solar radiation prediction using different techniques: model evaluation and comparison," *Renew. Sustain. Energy Rev.*, vol. 61, pp. 384–397, Aug. 2016.

[109]   S. Belaid and A. Mellit, "Prediction of daily and mean monthly global solar radiation using support vector machine in an arid climate," *Energy Convers. Manag.*, vol. 118, pp. 105–118, Jun. 2016.

[110]   S. Mehdizadeh, J. Behmanesh, and K. Khalili, "Comparison of artificial intelligence methods and empirical equations to estimate daily solar radiation," *J. Atmos. Solar-Terrestrial Phys.*, vol. 146, pp. 215–227, 2016.

[111]   N. K. C. Nair and N. Garimella, "Battery energy storage systems: Assessment for small-scale renewable energy integration," *Energy Build.*, vol. 42, no. 11, pp. 2124–2130, 2010.

[112]   T. Zoubir Roumila, Djamila Rekioua, "Energy management based fuzzy logic controller of hybrid system wind/photovoltaic/diesel with storage battery," *Int. J. Hydrogen Energy*, vol. 42, no. 30, pp. 19525–19535, Jul. 2017.

[113]   M. Cilogulları, M. Erden, M. Karakilcik, and I. Dincer, "Investigation of hydrogen production performance of a Photovoltaic and Thermal System," *Int. J. Hydrogen Energy*, vol. 42, no. 4, pp. 2547–2552, Jan. 2017.

[114]   H. Ozcan and I. Dincer, "Energy and exergy analyses of a solar based hydrogen production and compression system," *Int. J. Hydrogen Energy*, pp. 1–15, 2016.

[115]   J. Kotowicz, Ł. Bartela, D. Węcel, and K. Dubiel, "Hydrogen generator characteristics for storage of renewably-generated energy," *Energy*, vol. 118, pp. 156–171, 2017.

[116]   T. S. Uyar and D. Besikci, "Integration of hydrogen energy systems into renewable energy systems for better design of 100% renewable energy communities," *Int. J. Hydrogen Energy*, vol. 42, no. 4, pp. 2453–2456, 2017.

[117]   M. Calderón, A. J. Calderón, A. Ramiro, J. F. González, and I. González, "Evaluation of a hybrid photovoltaic-

wind system with hydrogen storage performance using exergy analysis," *Int. J. Hydrogen Energy*, vol. 36, no. 10, pp. 5751–5762, 2011.

[118]   Y. Kalinci, I. Dincer, and A. Hepbasli, "Energy and exergy analyses of a hybrid hydrogen energy system: A case study for Bozcaada," *Int. J. Hydrogen Energy*, vol. 42, no. 4, pp. 2492–2503, 2017.

[119]   O. V. Marchenko and S. V. Solomin, "Modeling of hydrogen and electrical energy storages in wind/PV energy system on the Lake Baikal coast," *Int. J. Hydrogen Energy*, vol. 42, no. 15, pp. 9361–9370, 2017.

[120]   F. Khalid, I. Dincer, and M. A. Rosen, "Analysis and assessment of an integrated hydrogen energy system," *Int. J. Hydrogen Energy*, vol. 41, no. 19, pp. 7960–7967, 2016.

[121]   H. Caliskan, I. Dincer, and A. Hepbasli, "Energy, exergy and sustainability analyses of hybrid renewable energy based hydrogen and electricity production and storage systems: Modeling and case study," *Appl. Therm. Eng.*, vol. 61, no. 2, pp. 784–798, 2013.

[122]   E. López González *et al.*, "Energy evaluation of a solar hydrogen storage facility: Comparison with other electrical energy storage technologies," *Int. J. Hydrogen Energy*, vol. 40, no. 15, pp. 5518–5525, 2015.

[123]   J. Andrews and B. Shabani, "Dimensionless analysis of the global techno-economic feasibility of solar-hydrogen systems for constant year-round power supply," *Int. J. Hydrogen Energy*, vol. 37, no. 1, pp. 6–18, 2012.

[124]   M. Smaoui, A. Abdelkafi, and L. Krichen, "Sizing of a stand-alone hybrid system supplying a desalination unit," *STA 2014 - 15th Int. Conf. Sci. Tech. Autom. Control Comput. Eng.*, vol. 120, pp. 820–824, 2014.

[125]   A. Maleki, F. Pourfayaz, and M. H. Ahmadi, "Design of a cost-effective wind/photovoltaic/hydrogen energy system for supplying a desalination unit by a heuristic approach," *Sol. Energy*, vol. 139, pp. 666–675, 2016.

[126]   A. Singh, P. Baredar, and B. Gupta, "Techno-economic feasibility analysis of hydrogen fuel cell and solar photovoltaic hybrid renewable energy system for academic research building," *Energy Convers. Manag.*, vol. 145, pp. 398–414, 2017.

[127]   T. H. T. Nguyen, T. Nakayama, and M. Ishida, "Optimal capacity design of battery and hydrogen system for the DC grid with photovoltaic power generation based on the rapid estimation of grid dependency," *Int. J. Electr. Power Energy Syst.*, vol. 89, pp. 27–39, 2017.

[128]   B. D. Shakya, L. Aye, and P. Musgrave, "Technical feasibility and financial analysis of hybrid wind-photovoltaic system with hydrogen storage for Cooma," *Int. J. Hydrogen Energy*, vol. 30, no. 1, pp. 9–20, 2005.

[129]   O. Brunin, M. Feidt, and B. Hivet, "Comparison of the working domains of some compression heat pumps and a compression-absorption heat pump," *Int. J. Refrig.*, vol. 20, no. 5, pp. 308–318, 1997.

[130]   J. Yu, X. Song, and M. Ma, "Theoretical study on a novel R32 refrigeration cycle with a two-stage suction ejector," *Int. J. Refrig.*, vol. 36, no. 1, pp. 166–172, 2013.

[131]   Ramesh K. Shah, Dusˇan P. Sekulic´, *Fundamentals of Heat Transfer*. 2010.

[132]   J. Sarkar, "Ejector enhanced vapor compression refrigeration and heat pump systems—A review," *Renew. Sustain. Energy Rev.*, vol. 16, no. 9, pp. 6647–6659, 2012.

[133]   A. Valero, M. A. Lozano, and M. Muñoz, "A general theory of exergy saving. I. On the exergetic cost," *Comput. Eng. energy Syst. Second law Anal. Model.*, vol. 3, pp. 1–8, 1986.

[134]   R. Selbaş, Ö. Kizilkan, and A. Şencan, "Thermoeconomic optimization of subcooled and superheated vapor compression refrigeration cycle," *Energy*, vol. 31, no. 12, pp. 1772–1792, 2006.

[135]   Y. M. El-Sayed, "Designing desalination systems for higher productivity," *Desalination*, vol. 134, no. 1–3, pp. 129–158, 2001.

[136]   E. Indicators, "Marshall&Swift Equipment Cost Index," *Chem. Eng.*, p. 72, 2011.

[137]   "EPRI Product." [Online]. Available: https://www.epri.com/#/pages/product/000000003002001434/. [Accessed: 31-May-2017].

[138]   A. Bejan and G. Tsatsaronis, *Thermal design and optimization*. John Wiley & Sons, 1996.

[139]   "Statistics and data of central bank." [Online]. Available: http://www.cbi.ir/Inflation/Inflation_FA.aspx. [Accessed: 31-May-2017].

[140]   "Statistics and information network| Home." [Online]. Available: http://isn.moe.gov.ir/. [Accessed: 16-Apr-2017].

[141]   S. Sanaye and A. Shirazi, "Thermo-economic optimization of an ice thermal energy storage system for air-conditioning applications," *Energy Build.*, vol. 60, pp. 100–109, 2013.

[142]   "Machine Learning in MATLAB - MATLAB & Simulink." [Online]. Available: https://www.mathworks.com/help/stats/machine-learning-in-matlab.html. [Accessed: 28-Sep-2017].

[143]   A. K. Yadav, V. Sharma, H. Malik, and S. S. Chandel, "Daily array yield prediction of grid-interactive photovoltaic plant using relief attribute evaluator based Radial Basis Function Neural Network," *Renew. Sustain. Energy Rev.*, Jun. 2017.

[144]   Z. Katambara and J. Ndiritu, "A fuzzy inference system for modelling streamflow: Case of Letaba River, South Africa," *Phys. Chem. Earth*, vol. 34, no. 10–12, pp. 688–700, 2009.

[145]   B. Haznedar and A. Kalinli, "Training ANFIS Using Genetic Algorithm for Dynamic Systems Identification," *Int. J. Intell. Syst. Appl. Eng.*, vol. 4, no. Special Issue, pp. 44–47, 2016.

[146]   M. V. Oliveira and R. Schirru, "Applying particle swarm optimization algorithm for tuning a neuro-fuzzy inference system for sensor monitoring," *Prog. Nucl. Energy*, vol. 51, no. 1, pp. 177–183, 2009.

[147]   A. Khosravi, R. N. N. Koury, L. Machado, and J. J. G. Pabon, "Prediction of wind speed and wind direction using artificial neural network, support vector regression and adaptive neuro-fuzzy inference system," *Sustain. Energy Technol. Assessments*, vol. 25, pp. 146–160, Feb. 2018.

[148]   S. Mehdizadeh, "Estimation of daily reference evapotranspiration (ET o) using artificial intelligence methods: Offering a new approach for lagged ET o data-based modeling," *J. Hydrol.*, 2018.

[149]   S. Mehdizadeh, J. Behmanesh, and K. Khalili, "New Approaches for Estimation of Monthly Rainfall Based on GEP-ARCH and ANN-ARCH Hybrid Models," *Water Resour. Manag.*, vol. 32, no. 2, pp. 527–545, 2018.

[150]   "IR : Iran Announces New Renewable Energy Facilities - General news news." [Online]. Available: http://www.instalbiz.com/news/1-full-news-ir-iran-announces-new-renewable-energy-facilities_201.html. [Accessed: 04-Jul-2017].

[151]   "Renewable Energy and Energy Efficiency Organization." [Online]. Available: http://www.satba.gov.ir/en/home. [Accessed: 05-Jul-2017].

[152]   S. A. Klein and J. C. Theilacker, "An algorithm for calculating monthly-average radiation on inclined surfaces," *J. Sol. Energy Eng.*, vol. 103, no. 1, pp. 29–33, 1981.

[153]   J. A. Duffie and W. A. Beckman, *Solar engineering of thermal processes*. John Wiley & Sons, 2013.

[154]   J. H. Watmuff, W. W. S. Charters, and D. Proctor, "Solar and wind induced external coefficients-solar collectors," *Coop. Mediterr. pour l'Energie Sol.*, vol. 1, p. 56, 1977.

[155]   A. S. Joshi, I. Dincer, and B. V. Reddy, "Thermodynamic assessment of photovoltaic systems," *Sol. Energy*, vol. 83, no. 8, pp. 1139–1149, 2009.

[156]   O. Baskut, O. Ozgener, and L. Ozgener, "Second law analysis of wind turbine power plants: Cesme, Izmir example," *Energy*, vol. 36, no. 5, pp. 2535–2542, 2011.

[157]   A. D. Şahin, I. Dincer, and M. A. Rosen, "Thermodynamic analysis of wind energy," *Int. J. Energy Res.*, vol.

30, no. 8, pp. 553–566, 2006.

[158] J. Sarkar, "Performance characteristics of natural-refrigerants-based ejector expansion refrigeration cycles," *Proc. Inst. Mech. Eng. Part A J. Power Energy*, vol. 223, no. 5, pp. 543–550, 2009.

[159] P. Chaiwongsa and S. Wongwises, "Effect of throat diameters of the ejector on the performance of the refrigeration cycle using a two-phase ejector as an expansion device," *Int. J. Refrig.*, vol. 30, no. 4, pp. 601–608, 2007.

[160] P. Chaiwongsa and S. Wongwises, "Experimental study on R-134a refrigeration system using a two-phase ejector as an expansion device," *Appl. Therm. Eng.*, vol. 28, no. 5–6, pp. 467–477, 2008.

[161] S. Disawas and S. Wongwises, "Experimental investigation on the performance of the refrigeration cycle using a two-phase ejector as an expansion device," *Int. J. Refrig.*, vol. 27, no. 6, pp. 587–594, 2004.

[162] N. Bilir Sag, H. K. Ersoy, A. Hepbasli, and H. S. Halkaci, "Energetic and exergetic comparison of basic and ejector expander refrigeration systems operating under the same external conditions and cooling capacities," *Energy Convers. Manag.*, vol. 90, pp. 184–194, 2015.

[163] D. Aghazadeh Dokandari, A. Setayesh Hagh, and S. M. S. Mahmoudi, "Thermodynamic investigation and optimization of novel ejector-expansion CO2/NH3 cascade refrigeration cycles (novel CO2/NH3 cycle)," *Int. J. Refrig.*, vol. 46, no. 94, pp. 26–36, 2014.

[164] J. Deng, P. Jiang, T. Lu, and W. Lu, "Particular characteristics of transcritical CO2 refrigeration cycle with an ejector," *Appl. Therm. Eng.*, vol. 27, no. 2–3, pp. 381–388, Feb. 2007.

[165] E. Nehdi, L. Kairouani, and M. Bouzaina, "Performance analysis of the vapour compression cycle using ejector as an expander," *Int. J. Energy Res.*, vol. 31, no. 4, pp. 364–375, 2007.

[166] M. Aminyavari, B. Najafi, A. Shirazi, and F. Rinaldi, "Exergetic, economic and environmental (3E) analyses, and multi-objective optimization of a CO2/NH3 cascade refrigeration system," *Appl. Therm. Eng.*, vol. 65, no. 1–2, pp. 42–50, 2014.

[167] T. R. Ayodele, A. S. O. Ogunjuyigbe, and C. G. Monyei, "On the global solar radiation prediction methods," *J. Renew. Sustain. Energy*, vol. 8, no. 2, p. 23702, 2016.

[168] S. X. Chen, H. B. Gooi, and M. Q. Wang, "Solar radiation forecast based on fuzzy logic and neural networks," *Renew. Energy*, vol. 60, pp. 195–201, 2013.

[169] S. Gupta, R., Singhal, "Prediction of Global Solar Radiation in UAE Using Artificial Neural Networks," *J. Sustain. Dev. energy, water Environ. Syst.*, vol. 4, no. 2, pp. 94–106, 2016.

[170] Z. Ramedani, M. Omid, A. Keyhani, S. Shamshirband, and B. Khoshnevisan, "Potential of radial basis function based support vector regression for global solar radiation prediction," *Renew. Sustain. Energy Rev.*, vol. 39, pp. 1005–1011, Nov. 2014.

[171] V. H. Quej, J. Almorox, J. A. Arnaldo, and L. Saito, "ANFIS, SVM and ANN soft-computing techniques to estimate daily global solar radiation in a warm sub-humid environment," *J. Atmos. Solar-Terrestrial Phys.*, vol. 155, no. February, pp. 62–70, 2017.

[172] L. Olatomiwa, S. Mekhilef, S. Shamshirband, K. Mohammadi, D. Petković, and C. Sudheer, "A support vector machine-firefly algorithm-based model for global solar radiation prediction," *Sol. Energy*, vol. 115, pp. 632–644, 2015.

[173] M. Bou-Rabee, S. A. Sulaiman, M. S. Saleh, and S. Marafi, "Using artificial neural networks to estimate solar radiation in Kuwait," *Renew. Sustain. Energy Rev.*, vol. 72, no. November 2016, pp. 434–438, 2017.

[174] K. Bakirci, "Prediction of global solar radiation and comparison with satellite data," *J. Atmos. Solar-Terrestrial Phys.*, vol. 152–153, no. December 2016, pp. 41–49, 2017.

[175] B. Liu and R. Jordan, "Daily insolation on surfaces tilted towards equator," *ASHRAE J.;(United States)*, vol.

10, 1961.

[176] A. Betz, "Introduction to the Theory of Flow Machines," *Pergamon Press*, pp. 167–174, 1966.

[177] O. Marchenko and S. Solomin, "Economic Efficiency of Renewable Energy Sources in Autonomous Energy Systems in Russia," *Int. J. Renew. ENERGY Res. Oleg Marchenko al*, vol. 4, no. 3, 2014.

[178] S. Diaf, G. Notton, M. Belhamel, M. Haddadi, and A. Louche, "Design and techno-economical optimization for hybrid PV/wind system under various meteorological conditions," *Appl. Energy*, vol. 85, pp. 968–987, 2008.

[179] F. Khalid, M. Aydin, I. Dincer, and M. A. Rosen, "Comparative assessment of two integrated hydrogen energy systems using electrolyzers and fuel cells," *Int. J. Hydrogen Energy*, vol. 41, no. 44, pp. 19836–19846, 2016.

[180] E. Akyuz, Z. Oktay, and I. Dincer, "Energy Analysis of Hydrogen Production from a Hybrid Wind Turbine-Electrolyzer System," in *Progress in Exergy, Energy, and the Environment*, Cham: Springer International Publishing, 2014, pp. 377–384.

[181] M. Beccali, S. Brunone, P. Finocchiaro, and J. M. Galletto, "Method for size optimisation of large wind–hydrogen systems with high penetration on power grids," *Appl. Energy*, vol. 102, pp. 534–544, Feb. 2013.

[182] Z. Yumurtacı and K. Toprak, "An Economic Analysis of Hydrogen Production Using Wind Power," *Int. J. Renew. Energy Res.*, vol. 1, no. 1, pp. 11–17, 2011.

[183] O. Marchenko and S. Solomin, "Efficiency of small autonomous wind/diesel/hydrogen systems in Russia," *Int. J. Renew. Energy Res.*, vol. 3, no. 2, 2013.

[184] O. V. Marchenko and S. V. Solomin, "The future energy: Hydrogen versus electricity," *Int. J. Hydrogen Energy*, vol. 40, no. 10, pp. 3801–3805, Mar. 2015.

[185] R. Carapellucci and L. Giordano, "Modeling and optimization of an energy generation island based on renewable technologies and hydrogen storage systems," *Int. J. Hydrogen Energy*, vol. 37, no. 3, pp. 2081–2093, Feb. 2012.